Optimal Design of Wind Turbine Blades for Bend Twist Coupling Effects

Department of Wind Energy Master Report

Niek Hesby Roeleven

DTU Wind Energy-M-0223

August 2018

DTU Wind Energy
Department of Wind Energy

Authors: Niek Hesby Roeleven

Title: Optimal Design of Wind Turbine Blades for Bend Twist Coupling Effects

DTU Wind Energy-M-0223
August 2018

Project Period:
October 2017 – August 2018

ECTS: 45

Education: Master of Science

Supervisors:
Mathias Stolpe
Alexander Verbart
DTU Wind Energy

Matthijs Langelaar
Jessica Holierhoek
TU Delft

Remarks:
This report is submitted as partial fulfillment of the requirements for graduation in the above education at the Technical University of Denmark.

DTU Wind Energy is a department of the Technical University of Denmark with a unique integration of research, education, innovation and public/private sector consulting in the field of wind energy. Our activities develop new opportunities and technology for the global and Danish exploitation of wind energy. Research focuses on key technical-scientific fields, which are central for the development, innovation and use of wind energy and provides the basis for advanced education at the education.

We have more than 240 staff members of which approximately 60 are PhD students. Research is conducted within nine research programmes organized into three main topics: Wind energy systems, Wind turbine technology and Basics for wind energy.

Technical University of Denmark
Department of Wind Energy
Frederiksborgvej 399
2800 Kgs. Lyngby
Denmark

www.vindenergi.dtu.dk

Optimal Design of Wind Turbine Blades for Bend Twist Coupling Effects

An European Wind Energy Master (EWEM) thesis

by

Niek Hesby Roeleven

to obtain the degree of Master of Science Aerospace Engineering
at the Delft University of Technology
and the degree of Master of Science European Wind Energy
at the Technical University of Denmark,
to be defended publicly on Thursday September 13, 2018 at 10:30 AM.

Student number:	4487508(TU Delft), s113696 (DTU)	
Project duration:	October 1, 2017 – August 30, 2018	
Thesis committee:	Prof. M. Stolpe	DTU, supervisor
	Dr. Ir. M. Langelaar,	TUDelft
	Dr. Ir. J. G. Holierhoek	TU Delft, supervisor
	Dr. Ir. R. C. Alderliesten	TU Delft, chairman
	Prof. E. Lund	AAU

Technical University of Denmark

DTU

TU Delft Delft University of Technology

Abstract

This thesis concerns the optimal design of wind turbine blades for bend twist coupling effects. Bend-twist coupling effects can prove to be an effective way of reducing fatigue damage and root bending moments for a wind turbine blade. However, how can bend-twist coupling be incorporated into a wind turbine blade considering the many structural requirements? This thesis investigates the optimal design for bend-twist coupling in wind turbine blades. Gradient based numerical optimization algorithms are applied to obtain composite material layups favorable for bend twist coupling. The thesis work builds a framework that allows for the selection of fiber angles at several sections along the blade, while considering structural constraints. This involves the use of a cross section analysis software and a finite element beam formulation for the evaluation of responses, while an aeroelastic software is used for load mitigation validation. The structural constraints include tip twists and deflection, eigenfrequencies and material failure criteria of which the analytic sensitivities are calculated, implemented in the framework and validated against central finite difference gradient values. A simple cantilever sandwich beam is considered first as a trial for the framework and four problem formulations are defined to test both the framework and the considered optimization algorithms. A full scale wind turbine blade for a 10MW wind turbine is then subject for the optimization. A converged design for the full scale blade is obtained and subject to aeroelastic simulations in a steady state and turbulent inflow. From this, the load mitigation effects are observed and discussed. With the work done in this thesis project, a step closer to an effective framework for aeroelastic tailoring is achieved.

Preface

With this thesis, I have challenged myself on all the knowledge I have obtained throughout my master program. The multidisciplinary optimization problem, posed in this study, combines my passion of wind turbine blades, composite materials and structural optimization. Had I known how big a task I've put before me, I would certainly have reduced my ambitions, since I had not accounted for the impact when things did not go as planned.

Coming here, to the final stage has been a stressful, demanding, and a wonderful journey, one that I would not have been without. I give my thanks to my loving family for supporting me fully all the way. After long hours you have always lifted my spirit and provided me with renewed energy. It would not have been possible without you.

A special thanks goes to my supervisor, Mathias Stolpe, who has quickly and thoroughly answered any question I posed. Your eye for detail and ability to ask the right questions has guided me in my work.

To Matthijs Langelaar: You have always been ready to help and stayed through my elaborate e-mails. Thank you for the discussions on sensitivities of strains and stresses, your input was highly valuable.

To Jessica Holierhoek: Although your way to this project was unusual, I value your sharp mind and outstanding knowledge of wind turbine blades.

Thanks to Koert Lindenburg from WMC who, through an email correspondence, led me to an usable analytic theory and experimental results of thin walled composite beams.
Last, a thanks to Alexander Verbart, who had to leave before the end. You are kind, patient, and gave engaging discussions and insights regarding stress constraints and aggregation methods.

Contents

List of Figures

List of Tables

List of Symbols

Vectors are written in bold small Latin and Greek letters, $\mathbf{u} \wedge \boldsymbol{\theta}$
Matrices are written in bold large Latin and Greek letters, $\mathbf{K} \wedge \boldsymbol{\Lambda}$

Missing units: mixed units

α	Bend-twist coupling factor	[-]
ϵ	Error	[-]
$\boldsymbol{\varepsilon}$	Strains	[-]
$\bar{\boldsymbol{\varepsilon}}$	Material limit strains	[-]
ν_{ij}	Poisson's ratio	[-]
ρ	Density	[kgm^{-3}]
$\boldsymbol{\sigma}$	Stresses	[Pa]
$\bar{\boldsymbol{\sigma}}$	Material strength	[Pa]
θ	Fiber angle	[°]
$\boldsymbol{\theta}$	Internal force and moments	
$\boldsymbol{\psi}$	Strain and curvatures	[-]
$\boldsymbol{\chi}$	Translation of reference point	[-]
$\boldsymbol{\varphi}$	Rotation of reference point	[rad]
$\boldsymbol{\omega}$	Eigenvalues	[rads^{-2}]
$\boldsymbol{\lambda}$	Eigenfrequencies	[Hz]
$\boldsymbol{\Lambda}$	Lagrange constraint multiplier	[-]
bc	boundary condition number	[-]
$\mathbf{e}_k$	Null vector with unity at k	
f	Objective function	
f_j	j^{th}-eigenfrequency	[s^{-1}]
$\mathbf{g}$	In-equality constraint functions	
$\mathbf{g}_w$	Warping displacements of point	
$\mathbf{h}$	Equality constraint functions	
lc	Load case number	[-]
$\mathbf{m}$	Moment and torsion	
n_λ	Number of eigenfrequencies	[-]
n_b	Number of beam elements	[-]
n_d	Number of d.o.f.	[-]
n_e	Number of 2D cross section elements	[-]
n_m	Number of materials pr. cross section	[-]
n_n	Number of 2D cross section nodes	[-]
n_{nb}	Number of global beam FE nodes	[-]
n_p	Number of patches in cross section	[-]
$nlse$	Number of layers input shellexpander.py	[-]
$nnpe$	Element connectivity with node number	[-]
$\mathbf{p}$	Global FE nodal loads and moments	
$\mathbf{p}_s$	Traction forces	[Pa]
$\mathbf{s}$	Reference point displacement	
$\mathbf{t}$	Shear force vector	[N]
u_φ^{tip}	Beam tip twist around z-axis	[rad]
u_y^{tip}	Beam tip deflection in y-direction	[m]
$\mathbf{u}$	Global FE nodal displacement field	
$\mathbf{v}$	Rigid body translation of point	
$\mathbf{w}$	Cross section equil. central solution	
$\mathbf{x}$	Column vector containing design variables	[°]
$\mathbf{x}_{dv}$	Design variables for particular cross section	[°]
$\mathbf{A}$	Material property matrix	
$\mathbf{A}_l$	Extensional stiffness matrix	[N]
$\mathbf{B}$	2D strain-displacement matrix	
$\mathbf{B}_l$	Bending-extension coupling matrix	[Nm]
$\mathbf{B}_b$	Beam strain-displacement matrix	[-]
$\mathbf{C}$	Cross section material property matrix	
$\mathbf{D}_l$	Bending stiffness matrix	[Nm^2]
$\mathbf{D}$	Warping constraint matrix	
E_{ii}	Material Youngs Modulus in ii direction	[Pa]
$\mathbf{E}$	Cross section material property matrix	
$\mathbf{F}_s$	Cross section compliance matrix	
$\mathbf{FI}_p$	Failure index for element patch p	[-]
G_{ij}	Material shear modulus in ij direction	[Pa]
$\mathbf{G}$	Cross section material property matrices	
$\mathbf{K}$	Cross section equilibrium stiffness matrix	
$\mathbf{K}_b$	Beam element stiffness matrix	
$\mathbf{K}_g$	Global FE beam stiffness matrix	
$\mathbf{K}_s$	Cross section stiffness matrix	
$\mathbf{L}$	Cross section material property matrix	
$\mathbf{M}$	Cross section material property matrix	
$\mathbf{M}_b$	Beam element mass matrix	
$\mathbf{M}_g$	Global mass matrix	
$\mathbf{M}_s$	Cross section mass matrix	
N	Number of cross sections	[-]
$\mathbf{N}$	FE interpolation functions	[-]
$\mathbf{N}_b$	Beam FE interpolation function	[-]
$\mathbf{Q}$	Lamina stiffness matrix	[Pa]
$\mathbf{Q}_m$	Material constitutive matrix	[Pa]
$\mathbf{R}$	Material property matrix	
$\mathbf{S}$	One dimensional strain-displacement matrix	[-]
T	Internal shear force	[N]
$\mathbf{T}$	Rotation matrix	[-]
$\mathbf{T}_r$	Sixth order auxiliary matrix for strains	[-]
$\mathbf{V}$	Array with eigenfrequencies vectors	[-]
$\mathbf{W}$	Central solution considering unit load	
W_{ext}	External work per unit length	[J]
W_{int}	Internal work or elastic energy per unit length	[J]
$\mathbf{X}$	Solutions to cross section equil. eq.	
$\mathbf{Y}$	Solutions to cross section equil. eq.	
$\mathbf{Z}$	Auxiliary matrix for cross section forces	[-]

List of abbreviations

- DTU - Technical University of Denmark
- WTB - Wind turbine blade
- BTC - Bend-twist coupling
- CFRP - Carbon fiber reinforced plastic
- GFRP - Glass fiber reinforced plastic
- UD - Unidirectional
- FE - Finite Element
- CoE - Cost of Energy
- CLT - Classical laminate theory
- CFRP - Carbon fiber reinforced plastic
- GFRP - Glass fiber reinforced plastic
- BECAS - BEam Cross sectional Analysis Software
- FRANS - FRame Analysis Software
- DLC - Design Load Case
- ETM - Extreme Turbulence Model
- FI - Failure Index
- SQP - Sequential Quadratic Programming

CHAPTER 1

Introduction

This thesis work investigates the optimal structural design of wind turbine blades for bend twist coupling effects. To this measure, a framework for structural optimizing of wind turbine blades (WTB) has been established. The philosophy is to obtain *the* design that fulfills the constraints in the best possible way considering minimization of a parameter belonging to the WTB. The study deals with the DTU 10MW reference WTB and the aim is to design it for bend-twist coupling (BTC) effects while maintaining its structural integrity. The following sections in this chapter presents the introduction, research aims, motivation and why the outcome of this thesis is interesting for the wind energy sector, introduction to the phenomenon BTC, and an overview of the report.

1.1 Wind turbine rotor blades

Wind turbines have seen a significant increase in size from commercial models in the 2000s of 2MW[11] to present 8MW (SWT-8.0-154 - Siemens[58]) and even 9.5MW (V164-9.5 MW Vestas[46]) full scale certified turbines. The innovation in the wind energy industry have pushed wind turbine blade sizes and lengths to a current world record of 88.4m. It was build by LM Wind Power for the company Adwen and intended a 8MW turbine. Considering that the blade mass increases with an almost cubed law as function of blade length[48] (see figure 1.1), further scaling highly increases the structural requirements of the blade and other components such as bearings, pitch actuators and tower. Another issue with increasing blade lengths is the flexibility of the blade, which can result in catastrophic failure if the blade becomes too flexible and hits the tower. The solution is new and innovative materials that offer higher stiffness at low cost of mass and improved design tools to better utilize these new materials and investigate new compositions and aeroelastic tailoring. With an ever increasing portfolio of candidate materials to use in WTB's a fast, accurate, and robust structural optimization scheme is needed in order to utilize and obtain the optimal design accounting for structural and stability constraints. Furthermore, with the optimization scheme, new designs utilizing the response of the WTB when subjected to aerodynamic loads in a beneficial way can quickly be obtained and researched.

Large WTBs are composed of several parts bonded together with adhesives, see figure 1.2. The main parts are shells, spar caps and webs which together secures the desired aerodynamic profile and structural properties while minimizing the weight. Each part consists of composite materials which provides high stiffness at low mass. The materials used are usually glass or carbon fibers, core materials such as foam or balsa wood and finally resin that binds it all together. This sort of composite, with a mixture of fibers and epoxy, is usually denoted fiber reinforced plastic (FRP). The composition of these materials, and by controlling the fiber angles, allow designs with anisotropic properties, beneficial for the blade while considering the structural requirements. Practice in industry requires the blade design to be validated in both FE- and aeroelastic software for numerous load cases which limits the number of design iterations due to the high computational costs. Traditionally, pure scaling[17] of WTB's offer a quick way to dimension longer blades for larger turbines, however, evaluating the best design

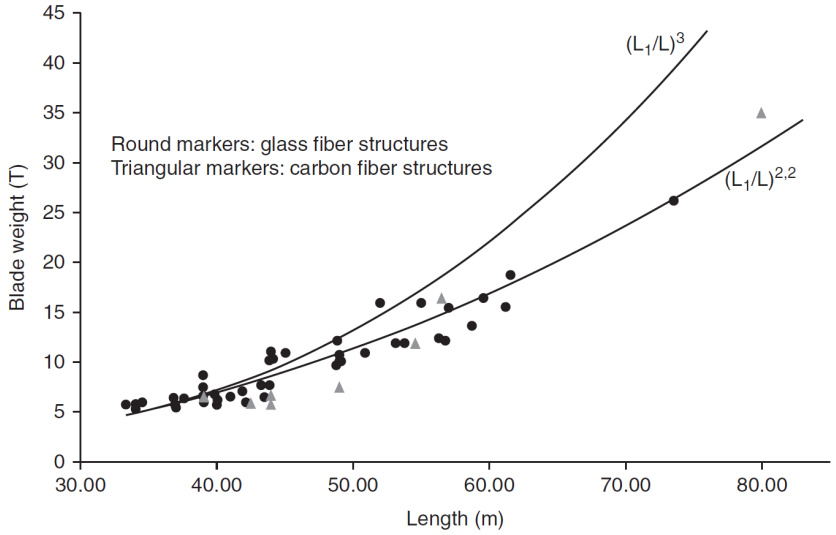

Figure 1.1: *Development of wind turbine blade lengths versus weight, taken from [11].*

from a database of materials is too time consuming and even with an automated process the computational costs is significant. Furthermore, leaps in technology frequently occurs such as prebended and swept blades, where the geometrical similarity assumption of pure scaling is invalid.

Loads, experienced by the WTB, consists of aerodynamic loads from the wind and self weight loads due to gravity. The blade response to these steady, cyclic and transient loads is illustrated in figure 1.2 and are flapwise deflection, edgewise deflection and torsional twist while the excitation from the same loads can cause vibrations that lead to resonance and instabilities. All of these contribute to the fatigue damage history of the blade and thus must be taken into account if the blade is to withstand 20+ years of operation.

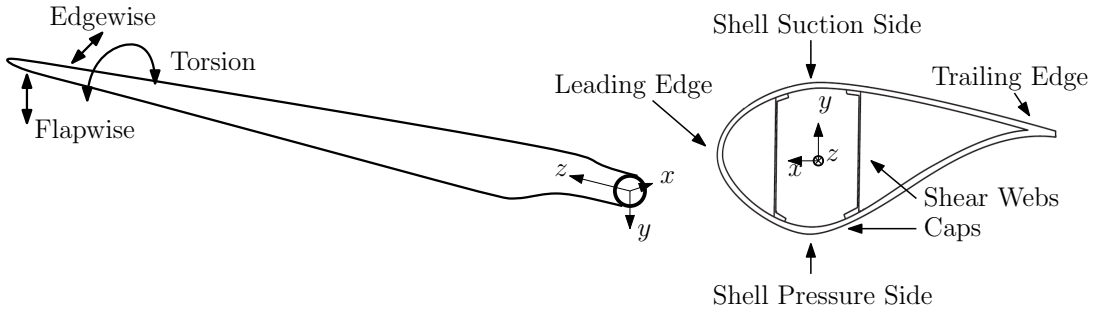

Figure 1.2: *(Left) Sketch of WTB with bending deflection, torsion twist Right WTB cross section (airfoil) and blade constituent parts.*

The torsional twist is of special interest, since this can be coupled with the flapwise deflection by either sweeping the blade (geometrical coupling) or having the fiber orientations off diagonal to the blade neutral axis (material coupling). Depending on the coupling, the blade will either twist towards stall or towards feather and doing so change the angle of attack which is the angle between the relative wind speed observed by the blade and the airfoil chord line. Figure 1.3 illustrates the torsional deflections. Increasing angle of attack results in greater lifting force of the blade until a point of flow separation known as stall. Decreasing the angle of attack will lower the generated lift as the chord line aligns with the relative wind direction and having

the chord line coinciding with the wind direction is called feathered position. For a sketch of a WTB airfoil and its relative angles and force vectors see figure A.1 in the appendix page 75. It should be noted here that besides the torsional twist, which is an elastic response to loads, the entire blade is twisted actively by the turbine control system and may contain a pre-twist (usual for stall regulated turbines). The active pitch action is denoted as *pitching* the blade and the pitch angle is the angle between chord line and plane of rotation.

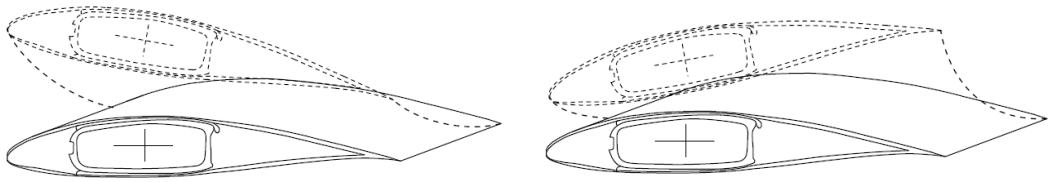

(a) *Twist towards stall* **(b)** *Twist towards feather*

Figure 1.3: *BTC wind turbine blade response to a bending load, from [27]*

1.2 Research aim

This thesis work attempts to design the 10MW DTU reference WTB (without prebend) such that bend-twist coupling is incorporated in the blade response to a flapwise loading. This is also known as aeroelastic tailoring where the response to loads on the blade is beneficial in one or more measures. The optimum WTB design must meet structural constraints such as eigenfrequencies, maximum flapwise tip deflections and stress constraints. To obtain the design, numerical gradient based algorithms, SQP (using *fmincon*) and IPOPT, are used together with a material optimization framework with continuous design variables. The aerodynamic profile and outer and inner dimensions of the blade are fixed, and it is up to the algorithm to orient the composite material such that the objective is minimized. With the geometry fixed, only fiber angles are considered in this study. It is believed that the framework can serve as a tool in aeroelastic tailoring which can prove advantageous in WTB design. It is desired that the framework does not pose significant computational costs, which influences the choice of software and modeling in this study. The following hypothesis is stated:

- *Material bend-twist coupling effects can effectively work as a passive load alleviation method for wind turbine blades without degrading the structural integrity specific to flapwise bending stiffness, eigenfrequencies and material stress limits.*

The following research objective can thus be defined as:

- *to design a framework that maximizes the rotational response in wind turbine blades undergoing flapwise bending by analyzing and designing the optimal structural properties or layup for bend twist coupling considering structural constraints using state of the art optimization algorithm(s).*

This allows for the optimum design of a wind turbine blade for bend-twist coupling effects considering careful chosen constraints. To obtain such a design, knowledge of bend-twist couplings in composite beams and wind turbine blades are sought through literature and parametric studies prior to a full blade optimization formulation. To defend the hypothesis, aeroelastic simulations

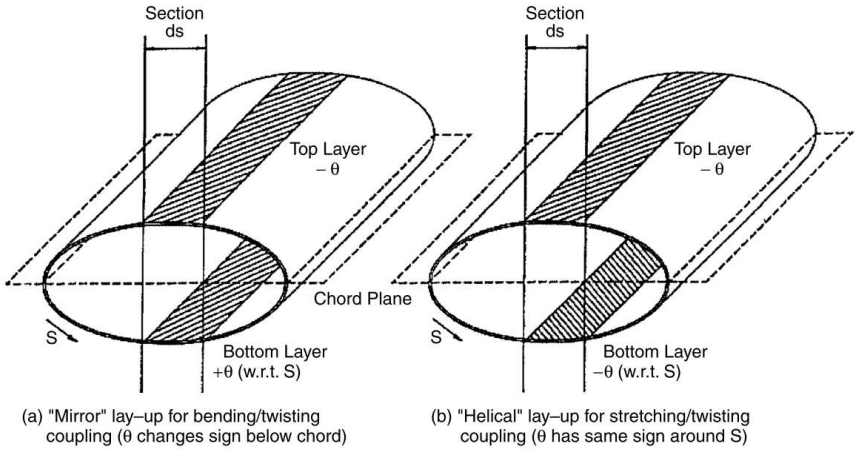

Figure 1.4: *Ways to incorporate BTC and stretch/twist coupling effects in WTB as suggested by Karaolis et al.[35]. Illustration taken from[42].*

using the software HAWC2 is proposed to validate the load mitigation effects. Validation of the deflective and rotational response with Abaqus was also considered at the beginning of the thesis work, however, had to be abandoned due to shortness of project time.

1.3 Motivation

The motivation for longer blades, and thus a larger swept area, is simply to be able to extract more energy from the wind with one turbine. Doing so, the cost of energy (CoE) is reduced making wind energy more competitive with other sources of energy [71]. With larger blade lengths comes increased aerodynamic loads and self weight which threatens the structural integrity of the blade and the wind turbine itself. Furthermore, long slender blades pose less bending stiffness such that when exposed to high loads the tip deflection is more significant. Incorporating BTC can reduce the total deflection of the blade since the blade will pitch to feather when deflecting flapwise. Furthermore, blades with BTC towards feather have shown to reduce the fatigue damage thus prolonging the life of the blade[10].

1.3.1 Bend-twist coupling

Generally two types of couplings have been considered for WTBs: extensional-bending and twist-bending couplings. Extensional-bending coupling is usually seen as a method for stall regulated turbines as an emergency brake mechanism such that if the rotational speed is too high the blade will twist due to the centrifugal forces[47]. There is therefore no load alleviation by using this coupling and it is not considered for this study. BTC produce a twist when the blade undergoes flapwise bending. If the twist occurs such that the blade turns up into the wind, the loads from the wind reduces and therefore this BTC is chosen for this study.
To incorporate BTC effects in a WTB, Karaolis et al.[35] suggested using biased layups in the shells. The fiber angles in the pressure and suction side shells are mirrored as illustrated in figure 1.4. A practical example of incorporating BTC effects on a WTB can e.g. be found in [5]. Research regarding the benefits and possibilities of coupled WTBs are numerous, however, a small recap of the most important findings is presented here.

Early researchs' initial motivation for BTC in WTB's was increased energy capture, aeroelastic

stability and load mitigation[42]. The increased energy capture is realized by having BTC effects towards stall, meaning when the blade undergoes flapwise bending, the blade also twists to higher angle of attacks thus increasing lift force. Research by Lobitz et al.[41] revealed BTCs towards stall could lead to divergence where the change in angle is self-enforcing leading to even higher twist angles until the structural limits of the blade are surpassed and catastrophic failure occurs. This phenomenon is known as divergence. Furthermore, the findings in the paper also showed increased risk of stall flutter, which is an excited torsional mode due to the de- and reattachment of the flow leading to increased amplitude in the oscillations. These findings has latest been fortified by Stäblein and Hansen [60] who investigated the aeroelastic properties of a simplified BTC blade section with an unsteady aerodynamic model in a linearised state-space formulation.
The desired coupling twists the blade towards feather as it undergoes flapwise bending and doing so reduces the angles of attack and the loads. The load mitigation by BTC is denoted as a passive load alleviation, meaning no actuators are needed to change the angle of attack. Today modern turbines are of the category variable-speed and -pitch, meaning the blade both operates at various rotational speeds and pitch angles, controlled by the wind turbine control system. The variable pitch allows for the blade to operate continuously at near maximum efficiency for lower wind speeds. As the wind speeds increase, the blades will be pitched out towards feather by the pitch mechanism. Just prior to reaching rated wind speed, which is the minimum wind speed where the wind turbine can produce its maximum power output, the wind turbine will experience its largest loads since the turbine control have not yet pitched the blades. The pitching of the blades are both to reduce the loads at higher wind speeds than rated wind speed and to maintain the rotational speed of generator below a set maximum.

So why consider BTC for load alleviation if the pitch system already does it? The pitch system reacts only when the generator rotational speed becomes larger than a certain threshold provided by the control strategy or emergency shut downs. It is too slow to react to sudden gusts and measuring the load on the blade or deflection in real-time is, to the authors knowledge, not feasible. The passive load alleviation is, however, instantaneous since the twisting occurs simultaneously with the flapwise deflection thus reducing loads and tip deflection. The effects of the load mitigation can be observed in the fatigue damage of the blades. Lobitz et al.[42] simulated wind turbines in turbulent and transient environments and compared the fatigue damage between rotors with BTC and without. The results showed significant reduction in fatigue damage up to 80% for stall controlled rotors, however, only for blades with very high couplings, which might not be feasible in production perspective considering fiber angles are discrete and material strains and stresses change when introducing BTC. The mitigation effects was reported less for pitch controlled turbines with 10% reductions which is still significant considering WTB's are designed for two decades of operation.
The BTC comes with a cost. When the blade twists towards feather, the lift force, which provides the torque for the generator, is reduced. Thus, a loss of power production is present. It has been suggested by Zahle et al. [71] to increase the rotor diameter to cope with the loss of power, allthough their passive load mitigation was obtained by optimizaing the internal structure of WTB. The effects can also be mitigated by pre-twist of the blade[42][1]. Another aspect is the lower bending stiffness which follows naturally when rotating fiber angles off axis. In this thesis study, structural constraints to ensure structural integrity and sufficient bending stiffness to prevent WTB collision with the wind turbine tower is ensured.

1.4 Layout of thesis

This section presents the layout of the remaining pages of this thesis and a small introduction to each point of what to expect from the different sections.

- Chapter 2: Methodology and theory
  Literature findings on composite beams are presented and an analytic theory is utilized to gain insight in BTC effects. The cross section analysis tool used in this project is introduced as well as the theory behind it. The loads considered for this study and cross section meshes are discussed in the end of this chapter.
- Chapter 3: Formulation of optimization problem:
  A general discussion on optimization and the solvers considered for this thesis work is presented as well as the analytic sensitivities.
- Chapter 4: Validation of framework
  The framework is validated with a simple study considering a cantilever sandwich beam of which the aim also is to obtain proper problem formulations and gain insight in the optimization algorithm performance.
- Chapter 5: Full blade optimization
  The DTU10MW reference WTB is subject to the optimization scheme and a converged result is obtained.
- Chapter 6: HAWC2 results
  The optimized blade design for BTC effects is subject to aeroelastic simulations to validate the load mitigation effects.
- Chapter 7: Future work
  The work not completed in this thesis and suggestions to future work is presented.
- Chapter 8: Conclusion

CHAPTER 2

Methodology and Theory

This chapter serves as an introduction to early analytic and experimental research regarding BTC in composite beams. Relevant literature findings and analytic methods are presented and used in a discussion of BTC effects. An introduction to the cross section analysis tool BECAS, used in this study, is later presented as well as the theory behind it. A discussion on the methodology used regarding 2D-meshing and the static load case is then provided in the end of this chapter.

2.1 Composite beam theories

There is no easy analytic method to estimate a WTB's blade response to loads. The varying cross section geometry and composite material properties oriented in different directions, all along the blade span, cannot be simplified to suitable hand calculations without losing too much information such that the results will be far from the WTB's real response. Nevertheless, in order to understand the BTC phenomenon better, analytic solutions to composite beams, capable of estimating the beam twist response due to BTC effects, has been sought and found in great numbers. Citing Volovoi et al.[68]:

"*There is no lack of composite beam theories. Quite the contrary, there might be too many of them.*"

Common for the beam theories are the basis in Euler-Bernoulli beam formulation that allows for simple static analysis of long, slender, beam-like structures. Extension to include shear deformation, by dropping the assumption that a cross section plane remains perpendicular to the beam bending axis after deformation, is then performed, and a Timoshenko beam formulation is obtianed[65]. A further extension can be made by including the St. Venant's torsion which assumes out-of-plane warping is unrestrained and therefore does not cause axial stress in the section. Stäblein reviews the importance of warping for closed section composite beams in the book MARE-WINT [45] and finds that general warping and shear deformation is influential whereas restrained warping is of less importance.
Numerical results from Chorténez and Piovan [19], using their own derived beam formulation, suggests that shear deformations are important for composite beam frequencies. The experimental investigation into thin walled composite beams with BTC effects by Chandra et al. [15] supports that both transverse shear and warping effects indeed are important. In a subsequent study, Chandra and Chopra[14] further investigated the importance of shear deformation and warping effects for open and closed beam sections with up to a remarkable 630% increase in torsional stiffness for a composite I-beam when warping was constrained.

The limited findings above are far from extensive, however, they give an insight into the vast area of research concerning thin-walled composite beams which is the basis of WTB's and one specific from Chandra et al.[15] will be used to compare numerical results in section 2.4.

2.2 The BTC parameter

This section serves as an introduction to the theoretical analysis developed by Lobitz and Veers[43] to investigate the BTC effects, and more interestingly, its limits. With the basis in beam stress-strain relationship developed by Karaolis et al. [35], a 2-by-2 sub-matrix system, coupling the bending and twisting response with off-diagonal terms in the cross-sectional stiffness matrix, is derived by Lobitz and Veers.

Using classical laminate theory (CLT), Karaolis et al. presented a method that describes the amount of coupling present in a structure. The theory has later been treated, corrected and validated by Kooijman[37] and Ong and Tsai [50]. Based on the theory, Lobitz and Veers [41] proposed a coupling parameter, α, as a measure of BTC. The theory leading to this parameter is shortly presented here.

The anisotropic constitutive relation in CLT for a laminate is given as a 6-by-6 matrix that relates the global strains and stresses, see eq. (2.1) (taken Jones's book on mechanics of materials[34]).

$$\begin{bmatrix} N_x \\ N_y \\ N_{xy} \\ M_x \\ M_y \\ M_{xy} \end{bmatrix} = \begin{bmatrix} A_{11} & A_{12} & A_{16} & B_{11} & B_{12} & B_{16} \\ A_{21} & A_{22} & A_{26} & B_{21} & B_{22} & B_{26} \\ A_{61} & A_{62} & A_{66} & B_{61} & B_{62} & B_{66} \\ B_{11} & B_{12} & B_{16} & D_{11} & D_{12} & D_{16} \\ B_{21} & B_{22} & B_{26} & D_{21} & D_{22} & D_{26} \\ B_{61} & B_{62} & B_{66} & D_{61} & D_{62} & D_{66} \end{bmatrix} \begin{bmatrix} \epsilon_x \\ \epsilon_y \\ \gamma_{xy} \\ \kappa_x \\ \kappa_y \\ \kappa_{xy} \end{bmatrix} \tag{2.1}$$

In short it is written as $[\mathbf{N};\mathbf{M}] = [\mathbf{A_l B_l};\mathbf{B_l D_l}][\boldsymbol{\epsilon}]$. The submatrices are named as: $\mathbf{A}_l$ is the extensional stiffness matrix, $\mathbf{B}_l$ is the bending-extension coupling stiffness matrix and $\mathbf{D}_l$ is the bending stiffness matrix and the inverse of the constitutive matrix in eq. (2.1) is $[\mathbf{ab};\mathbf{bd}]$. The elements in $\mathbf{A}_l$, $\mathbf{B}_l$ and $\mathbf{D}_l$ are calculated by:

$$A_{ij} = \sum_{k=1}^{n} \left(\bar{Q}_{ij}\right)_k (z_k - z_{k-1}), \quad B_{ij} = \sum_{k=1}^{n} \frac{1}{2} \left(\bar{Q}_{ij}\right)_k (z_k^2 - z_{k-1}^2), \quad D_{ij} = \sum_{k=1}^{n} \frac{1}{3} \left(\bar{Q}_{ij}\right)_k (z_k^3 - z_{k-1}^3) \tag{2.2}$$

where $(\bar{Q}_{ij})_k$ is the rotated local lamina stiffness matrix for the k^{th} layer in the laminate and z_k is the thickness coordinate. The entries in $(Q_{ij})_k$ are shown in eq. (2.3) for assumed plane stress.

$$\mathbf{Q}_k = \frac{1}{1 - \nu_{12}\nu_{21}} \begin{bmatrix} E_{11} & \nu_{21}E_{22} & 0 \\ \nu_{21}E_2 & E_{22} & 0 \\ 0 & 0 & G_{12}\left(1 - \nu_{12}\nu_{21}\right) \end{bmatrix} \tag{2.3}$$

When rotated with standard rotation matrix $\mathbf{T}$, the matrix is fully populated: $\bar{\mathbf{Q}}_k = \mathbf{T}\mathbf{Q}_k\mathbf{T}^T$. It is possible to estimate the local material stresses for the k^{th}- lamina by Hook's Law $\boldsymbol{\sigma}_l = \mathbf{Q}_k\boldsymbol{\epsilon}_l$ where the subscript l denotes rotated strains and stresses. In order to derive a simplified theory from this, Karaolis et al. made the following assumptions:

- The structure analyzed is a thin-walled beam with wall thickness much smaller than width ($t << c$). As a result the in-plane skin bending and coupling are negligible compared to the entire beam performance[37].
- Only linear elastic deformation is considered.

- Stress concentrations due to warping incompatibility or shear lag are ignored.

The following derivation follows that given by Ong and Tsai [50] but builds on the work of Lobitz et al. [41]. The full matrix, $\bar{\mathbf{Q}}_k$ is reduced to a 2-by-2 matrix by assuming the in-plane normal stress, σ_{22} is zero. This gives:.

$$\begin{bmatrix}\sigma_{11}\\ \sigma_{22}\\ \tau_{12}\end{bmatrix} = \begin{bmatrix}Q_{11} & Q_{12} & Q_{16}\\ Q_{21} & Q_{22} & Q_{26}\\ Q_{61} & Q_{62} & Q_{66}\end{bmatrix}\begin{bmatrix}\epsilon_{11}\\ \epsilon_{22}\\ \gamma_{12}\end{bmatrix} \rightarrow \begin{bmatrix}\sigma_{11}\\ \tau_{12}\end{bmatrix} = \begin{bmatrix}\bar{Q}_{11} & \bar{Q}_{16}\\ \bar{Q}_{61} & \bar{Q}_{66}\end{bmatrix}\begin{bmatrix}\epsilon_{11}\\ \gamma_{12}\end{bmatrix} \tag{2.4}$$

with

$$\bar{Q}_{11} = Q_{11} - \frac{Q_{12}Q_{21}}{Q_{22}}, \quad \bar{Q}_{16} = Q_{16} - \frac{Q_{12}Q_{26}}{Q_{22}}, \quad \bar{Q}_{61} = Q_{61} - \frac{Q_{62}Q_{21}}{Q_{22}}, \quad \bar{Q}_{66} = Q_{66} - \frac{Q_{62}Q_{26}}{Q_{22}} \tag{2.5}$$

This reduces eq. (2.1) and by assuming a symmetric layup, $\mathbf{B} = \mathbf{0}$, a relation between bending- and torsion moment and the respective curvature and twist is obtained:

$$\begin{bmatrix}N_x\\ N_{xy}\\ M_x\\ M_{xy}\end{bmatrix} = \begin{bmatrix}\bar{A}_{11} & \bar{A}_{16} & \bar{B}_{11} & \bar{B}_{16}\\ \bar{A}_{61} & \bar{A}_{66} & \bar{B}_{61} & \bar{B}_{66}\\ \bar{B}_{11} & \bar{B}_{16} & \bar{D}_{11} & \bar{D}_{16}\\ \bar{B}_{61} & \bar{B}_{66} & \bar{D}_{61} & \bar{D}_{66}\end{bmatrix}\begin{bmatrix}\epsilon_x\\ \gamma_{12}\\ \kappa_x\\ \kappa_{xy}\end{bmatrix} \overset{\mathbf{B}=\mathbf{0}}{\rightarrow} \begin{bmatrix}M_y\\ M_{xy}\end{bmatrix} = \begin{bmatrix}\bar{D}_{11} & \bar{D}_{16}\\ \bar{D}_{61} & \bar{D}_{66}\end{bmatrix}\begin{bmatrix}\kappa_x\\ \kappa_{xy}\end{bmatrix} \tag{2.6}$$

Here κ_x is the bending curvature and κ_{xy} is the twist curvature. Ong and Tsai [50] relates $\bar{D}_{ij}$ to Lobitz and Veers' [41] stiffness terms by:

$$\frac{\partial\theta}{\partial x} = \kappa_x, \quad \frac{\partial\varphi}{\partial x} = \kappa_{xy}, \quad \bar{D}_{11} = \frac{EI}{b}, \qquad \bar{D}_{66} = \frac{GJ}{b}, \quad \bar{D}_{16} = \bar{D}_{61} = -\frac{g}{b} \tag{2.7}$$

where b is the width of the laminate and g is the BTC term. Rewriting eq. (2.6) and leaving out $1/b$ for abbreviation:

$$\begin{bmatrix}M_x\\ M_{xy}\end{bmatrix} = \begin{bmatrix}EI & -g\\ -g & GJ\end{bmatrix}\begin{bmatrix}\kappa_x\\ \kappa_{xy}\end{bmatrix} \tag{2.8}$$

If the structural coupling term, g is zero, there exists no coupling. In order for the 2-by-2 matrix to be positive definitive the following must hold: $|g| = \sqrt{EI \cdot GJ}$. To investigate intermediate values of the coupling term the following relation is defined [41]:

$$\alpha = \frac{g}{\sqrt{EI \cdot GJ}}, \quad -1 \leq \alpha \leq 1 \tag{2.9}$$

The above limits are theoretical and it has been shown by Ong and Tsai [50] that in practice the limits are ± 0.6. To illustrate how the parameter changes with angles, figure 2.1 has been produced using standard material properties presented in table 2.1. The subject is a sandwich beam with the top and bottom face having the same fiber orientation using either glass fiber reinforced plastics (GFRP) or carbon fiber reinforced plastics (CFRP). CLT is then used to determine the stiffness terms needed to calculate the coupling parameter in eq. (2.9).

2.2.1 Discussion on coupling contributors

Controlling the fiber angles has a direct effect on the stiffness terms values which control the amount of coupling. As observed in figure 2.1, choice of material also affects the amount of coupling possible where CFRP outperforms GFRP. This is also supported by findings in literature

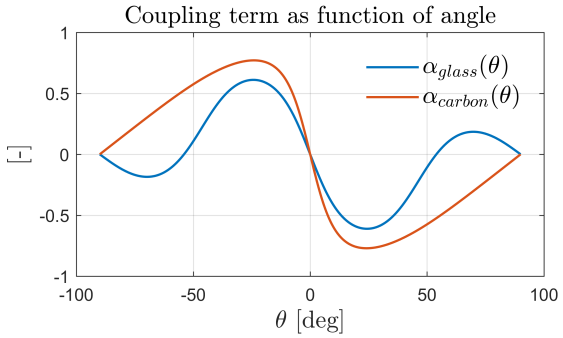

Figure 2.1: *Coupling parameter as function of angles in a sandwich beam with symmetric layup.*

	GFRP	CFRP	Core
E_{11}[GPa]	35.7	160	0.075
E_{22}[GPa]	10.6	6.9	0.075
G_{12}[GPa]	2.81	6.21	0.020
ν_{12}[-]	0.324	0.28	0.1

Table 2.1: *FRP properties from [40] and core materials from [22] as Divinycell H60*

e.g. [40], [50]. Further observing the results in figure 2.1, the optimum angle for highest/lowest coupling parameter, α, for this sandwich beam is approximately 25-30°, depending on material. This also stems well with literature findings: Chandra et al.[15] concluded that symmetric layups indeed results in BTC and that the coupling is greater with larger angles. Ong and Tsai[50] performed experiments on composite D-spars and concluded that the three main contributors for BTC effects are the material, ply orientation and proportional volume of anisotropy layers in the laminate. Fedorov and Berggreen[26] performed experiments on composite beams and small sections of WTB's. They concluded that a loss of 30-35% in bending stiffness is present when unidirectional (UD) glass fibers in the spar cap are oriented 20-25° off axis. Furthermore, using the simple Euler Bernoulli beam formulation developed by Lobitz and Veers[41], they could express the BTC parameter for these WTB sections. Their findings indicate a maximum of 0.2 BTC parameter for glass UD fibers and 0.4 for carbon fibers. These are important findings and could aid when considering constraints for the optimization scheme.
The above findings lay out a reasonable picture of what to aim for for the full blade optimization in this study. More examples of research concerning BTC effects in WTB's could easily be found, however, to limit the extend of this study the above chosen are the most important. Furthermore, geometrical parameters, such as the placement of shear webs and load application point can also affect the blade response when deflecting in a bend-twist coupled way, but will not be treated in this study, since the geometry is fixed.

2.3 Structural model

Given the high complexity BTC's introduce (in the form of warping and coupled response to loads), a robust and accurate framework is needed for the optimization. The accuracy can be obtained using FE discretization which is well suited for complex structures and responses and commercial software such as Ansys, Abaqus, or COMSOL exist, which are capable of handling composites. The aim is to perform structural optimization on the DTU10MW reference WTB which is no small problem and requires a lot of iterative evaluations of the structure response to small changes in material orientations. Although providing great detail, the mentioned software requires a detailed mesh i.e. a high number of elements and, to the authors knowledge, they do not provide sufficient model simplifications to reduce the computational costs significantly. A WTB is a long, slender, structure that can be represented by a FE beam model and doing so, avoid the need of a shell-element mesh representation of the entire blade surface and internal structure. The difficulty lies in obtaining the cross section stiffness matrices for each section/beam element of the blade. To this matter, BECAS will be used.

2.3.1 Introduction to BECAS

The BEam Cross sectional Analysis Software (BECAS v3.3) was developed by José Blasques[6] and builds on the theory of Giavotto et al.[29]. The input to the software is a 2D mesh of any arbitrary geometry with any anisostropic and oriented material properties. BECAS then assembles a 6-by-6 stiffness matrix while accounting for all geometrical and material induced couplings. In the introduction to this chapter, a small number of highlighted literature findings showed that warping effects and shear deformation should be accounted for. This is the case for the BECAS software and therefore a suitable choice for this study. The cross section stiffness matrix can be used with 3D beam FE's to present any beam like structure such as a WTB. BECAS is very conveniently free for academic purposes and is written in MATLAB. It is currently maintained at the Department of Wind Energy DTU.

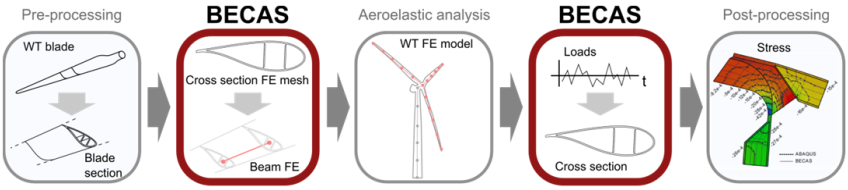

Figure 2.2: *Typical workflow of WTB design using BECAS from[24]*

As observed in figure 2.2, not all tasks are handled by BECAS. Pre- and post processing as well as load application and response calculations must be performed by different software. For example, the cross section mesh must be provided along with the material properties of each element in the mesh. As a minimum, BECAS requires 5 input files for the computational work intended in this thesis work:

- N2D.in: (n_n-by-3) array with nodal positions where each row is [node label, x-coordinate, y-coordinate].
- E2D.in: (n_e-by-$nnpe$) array with element connectivity where each row is [element label, node 1, ..., node $nnpe$) where $nnpe$ depends on element type.
- EMAT.in: (n_e-by-4) array with element material properties where each row is [element label, material number, fiber angle, fiber plane angle].
- MATPROPS.in: (n_{mat}-by-10) array with the material properties where each row is in the form [E_{11}, E_{22}, E_{33}, G_{12}, G_{13}, G_{23}, ν_{12}, ν_{13}, ν_{13}, ρ]. Each row correspond to a unique material referred to by second column from EMAT.in.
- FAILMAT.in: (n_{mat}-by-19) array with the failure criterion selection flag (1-4) in the first column and the material characteristics in the remaining 18 columns. Note that in this study fatigue damage is not estimated, so the last three columns in FAILMAT.in are left empty. To see the order and nomenclature of the material strength parameters, see e.g. table 4.3.

With BECAS the cross section stiffness matrices can be evaluated, however, response to loads must be evaluated by alternative software. This is done with the software FRANS which accompanies BECAS, see below.

2.3.2 Introduction to FRANS

The aerodynamic loads from the wind and the gravitational loads due to the self-weight cannot be evaluated by BECAS. However, with known loads (e.g. a load case from the DTU10MW report[3]) on the WTB, BECAS can via the FRame ANalysis Software (FRANSv0.2) evaluate

the response i.e. displacement, eigenfrequencies, strains, and stresses in each cross section finite element. FRANS creates a 3D beam finite element representation of the WTB using the cross section stiffness matrices from BECAS. The process is visualized in figure 2.3. In this study, only composite beams or WTB's are considered which share similar boundary conditions, that is, clamped at one end (root) and free at the other (tip). The method to construct and build the beam FE representation of the WTB can be read in detail in e.g. [6], but is for convenience presented here.

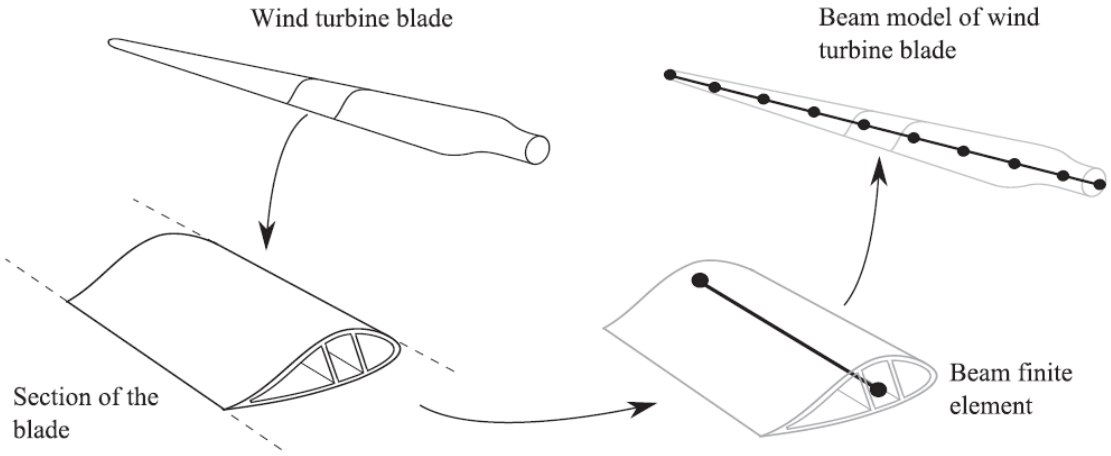

Figure 2.3: *Schematic of the creation of the FE beam discretized model of a WTB as done by FRANS, taken from [6]*

The global beam stiffness matrix $\mathbf{K}_g$ is defined as:

$$\mathbf{K}_g = \sum_{b=1}^{n_b} \mathbf{K}_b = \sum_{b=1}^{n_b} \int_0^{L_b} \mathbf{B}_b^T \mathbf{K}_s \mathbf{B}_b \mathrm{dz} \tag{2.10}$$

where n_b is the number of beam elements and L_b is the length of element b. The summation refers to typical FE assembly and $\mathbf{B}_b$ is the strain-displacement matrix and $\mathbf{K}_s$ is the cross section stiffness matrix for the cross section associated with the beam element b, provided by BECAS. A global FE mass matrix for the FE beam representation can be obtained in a similar fashion by:

$$\mathbf{M}_g = \sum_{b=1}^{n_b} \mathbf{M}_b = \sum_{b=1}^{n_b} \int_0^{L_b} \mathbf{N}_b^T \mathbf{M}_s \mathbf{N}_b \mathrm{dz} \tag{2.11}$$

where $\mathbf{N}_b$ is a shape function matrix and $\mathbf{M}_s$ is the cross section mass matrix also provided by BECAS. The size of $\mathbf{K}_g$ depends on the number of beam elements and element type. A 2-node FE beam model with n_b number of beam elements will have a stiffness matrix, $\mathbf{K}_g$, of $(n_b + 1)$-by-$(n_b + 1)$ whereas a 4-node FE beam model with n_b number of beam elements will result in a $(3n_b + 1)$-by-$(3n_b + 1)$ stiffness matrix. Using elements with higher number nodes generally increase the accuracy of the FE method, especially for nonlinear problems. The software FRANS uses 4-node beam FE as standard and for each node, 6 dof's are present (3 displacement and 3 rotations in the order $[u_x,\ u_y,\ u_z,\ \varphi_x,\ \varphi_y,\ \varphi_z]$, see figure 2.4 for coordinate system). A choice must be made regarding at which node to evaluate displacement, rotation and stresses. Choosing nodes closest to the clamped end will provide the highest

stresses whereas choosing nodes farthest away from clamped end provides highest accumulated displacement and rotations. The stiffness is assumed constant along the length of a beam element which contravene with actual stiffness distribution. The effects of this can be mitigated by increasing number of elements and a method was discovered in one of the templates files accompanied BECAS to do this in an efficient way. A total of n_b sections are made along a beam structure and BECAS is used to calculate the cross section stiffness matrix for each section. Linear interpolation of the stiffness is then performed between adjacent sections to obtain even more unique stiffness matrices destined for more beam elements. This way, the resolution is increased at a low computational cost. The increased discretized beam is used to evaluate the nodal displacement field and eigenvalues. The nodal displacement and rotations, $\mathbf{u}$, can be approximated by solving the following equilibrium eq.:

$$\mathbf{K}_g\mathbf{u} = \mathbf{p} \tag{2.12}$$

where $\mathbf{p}$ is the static forces and moments applied to the nodes and $\mathbf{K}_g$ is defined in eq. (2.10). Throughout this study when performing structural optimization, it is assumed the loads are independent of the design variables (fiber orientation) i.e. they remain the same even though the actual aerodynamic loads, of which they have their basis, are dependent on the blade response. It is a two way interaction. The wind exert a force on the blade so the blade deflects. The deflection changes the inflow angles to the blade which changes the loads from the wind and so forth. Including this "aero"-"elastic" phenomenon in the structural optimization would definitely give a more realistic response, however, also severely complicate the optimization framework. A feedback loop to an aeroelastic tool would be necessary.

FRANS needs four input files defined for it to build the global beam element stiffness matrix, mass matrix and load vector.

- N1D.in: (n_{bn}-by-2) array with nodal positions in a 1D space where each row is [node label, coordinate].
- E1D.in: (n_b-by-5) array with beam element connectivity where each row is [element label, node 1 ...., node 4].
- F1D.in: (lc x n_b-by-5) array with load case number, load type, beam node for application, on which d.o.f. the load acts, and load magnitude. Each row is [load case, load type(1-3), beam element node, d.o.f., magnitude].
- B1D.in: (bc-by-3) array with boundary condition where each row is [boundary condition number, d.o.f., boundary condition magnitude].

2.3.3 The theory behind BECAS

This section makes an effort to briefly present the theory behind BECAS. Although numerous papers can be referenced for an outline of the theory, it was deemed necessary to present it in this study, due to its significance by allowing to define a simple 6-by-6 cross sectional stiffness matrix from any cross section geometry and any number of anisotropic materials in that cross section. Furthermore, references to some of the equations in this section is made in the sensitivity analysis in section 3.3.
The method developed by Giavotto et al. [29] takes in a 2D discretized cross section geometry and sets up equilibrium equations using the virtual work principle. The solution to the equilibrium equations is a set of second order linear differential equations with two solutions as *the extremity solution* and *the central solution*, using the nomenclatour from Giavotto et al. The following introduces the theory.

Considering an arbitrary slice of an arbitrary beam cross section, as shown in figure 2.4, with the defined cartesian coordinate system xyz. The internal forces and moments, acting at a reference point, O, in the cross section are shear forces in the x- and y-directions (T_x and T_y respectively), an axial tension force in the z-direction (T_z), bending moments around x- and y-axis (M_x and M_y respectively) and a torsional moment around the z-axis (M_z). All internal forces and moments are described with the 6-by-1 vector $\boldsymbol{\theta}$ where the elements are the forces and moments in the order presented above. Likewise, a strain-curvature vector is defined as $\boldsymbol{\psi}$ containing the elements of the shear strains (τ_x, τ_y), the tension strain (τ_z), the bending curvatures (κ_x, κ_y), and the twist rate (κ_z).

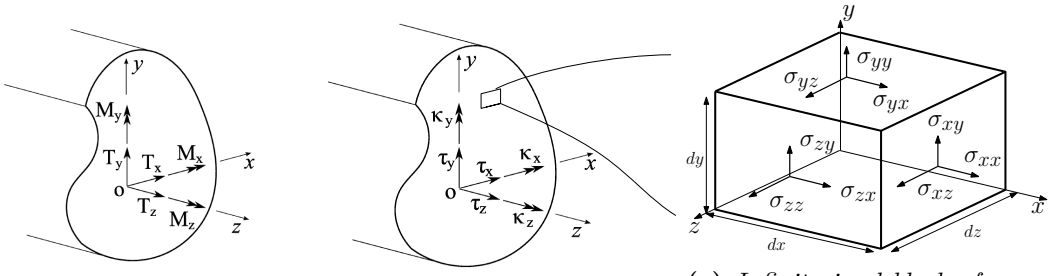

(a) *Forces and moments* **(b)** *Strains and curvatures* **(c)** *Infinitesimal block of cross section*

Figure 2.4: *Beam cross section coordinate system. (a) forces and moments (b) strains and curvatures, taken from [6]. (c) sign convention of dx-dy-dz infinitesimal block.*

When the beam is loaded, the stresses and strains at any point in the cross section can be described with the vectors:

$$\boldsymbol{\sigma} = [\sigma_{xx} \;\; \sigma_{yy} \;\; \sigma_{xy} \;\; \sigma_{xz} \;\; \sigma_{yz} \;\; \sigma_{zz}]^T \tag{2.13}$$

$$\boldsymbol{\varepsilon} = [\varepsilon_{xx} \;\; \varepsilon_{yy} \;\; 2\varepsilon_{xy} \;\; 2\varepsilon_{xz} \;\; 2\varepsilon_{yz} \;\; \varepsilon_{zz}]^T \tag{2.14}$$

Following normal convention, the first subscript in eq. (2.13) and (2.14) denotes the plane and the second the direction of which it is acting. The stresses and strains are related with the constitutive matrix, $\mathbf{Q}$, through Hook's Law; $\boldsymbol{\sigma} = \mathbf{Q}\boldsymbol{\varepsilon}$. Observing figure 2.5a, the internal forces and moments are related to the stresses by:

$$\mathbf{t} = \int_A \mathbf{p}_s \mathrm{dA}, \qquad \mathbf{m} = \int_A \mathbf{Z}^T \mathbf{p}_s \mathrm{dA} \tag{2.15}$$

where $\mathbf{p_s} = [\sigma_{xz} \;\; \sigma_{yz} \;\; \sigma_{zz}]^T$, $\mathbf{t} = [T_x \;\; T_y \;\; T_z]^T$, $\mathbf{m} = [M_x \;\; M_y \;\; M_z]^T$ and:

$$\mathbf{Z}_{xyz} = \begin{bmatrix} 0 & -z & y \\ z & 0 & -x \\ -y & x & 0 \end{bmatrix} \tag{2.16}$$

combining this gives the vector of section forces:

$$\boldsymbol{\theta} = [\mathbf{t} \;\; \mathbf{m}]^T = \int_A \mathbf{Z}_{xyz}^T \mathbf{p_s} \mathrm{dA} \tag{2.17}$$

where the matrix $\mathbf{Z} = [\mathbf{I}_3 \;\; \mathbf{Z}_{xyz}^T]$. The strains and curvatures in $\boldsymbol{\varphi}$ are related to the section internal forces and moments through the constitutive relation $\boldsymbol{\varphi} = \mathbf{F}_s\boldsymbol{\theta}$ where $\mathbf{F}_s$ is the 6-by-6 cross section compliance matrix. The stiffness matrix is $\mathbf{K}_s = \mathbf{F}_s^{-1}$ such that $\boldsymbol{\theta} = \mathbf{K}_s\boldsymbol{\varphi}$.

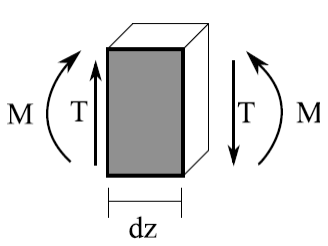

(a) *Cross section resultant forces.*

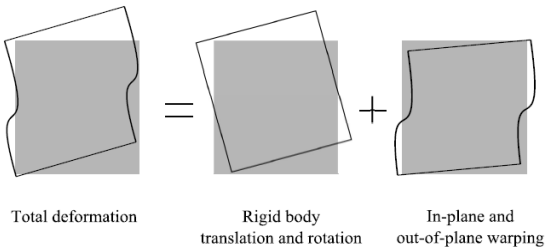

(b) *Rigid body translation and rotation and in-plane and out-of-plane contributions.*

Figure 2.5: *(a) the cross section resultant forces for a slice dz of the beam (b) contributions to total deformation of the beam cross section, both taken from [8]*

Kinematics

At an arbitrary point in the cross section, the displacement is defined as $\mathbf{s} = \mathbf{v} + \mathbf{g}$ where $\mathbf{v} = [v_x \;\; v_y \;\; v_z]^T$ is the vector of displacements associated with rigid body translation and rotation and $\mathbf{g}_w = [g_x \;\; g_y \;\; g_z]^T$ is the vector of warping displacements, see figure 2.5b. The rigid body displacements can be represented by the translations and rotations of the cross section reference point such that $\mathbf{v} = \mathbf{Z}\mathbf{r}$, where $\mathbf{r} = \left[\boldsymbol{\chi}^T(z) \;\; \boldsymbol{\varphi}^T(z)\right]^T = [\chi_x \;\; \chi_y \;\; \chi_z \;\; \varphi_x \;\; \varphi_y \;\; \varphi_z]^T$. The warping displacements can be interpolated as $\mathbf{g}(x, y, z) = \mathbf{N}_i(x, y)\mathbf{u}(x_i, y_i, z)$ where $\mathbf{N}$ is the typical finite element shape functions and $\mathbf{u}$ is the nodal warping displacements. The total displacement of a point on the cross section is thus:

$$\mathbf{s} = \mathbf{Z}\mathbf{r} + \mathbf{N}\mathbf{u} \tag{2.18}$$

Strain-displacement relation

Assuming small displacements, the strain-displacement relation with tensor notation is:

$$\boldsymbol{\varepsilon}_{ij} = \frac{1}{2}\left(u_{i,j} + u_{j,i}\right), \qquad (i, j = x, y, z) \tag{2.19}$$

Inserting eq. (2.18) results in the expression

$$\boldsymbol{\varepsilon} = \mathbf{S}\mathbf{Z}\boldsymbol{\psi} + \mathbf{B}\mathbf{N}\mathbf{u} + \mathbf{S}\mathbf{N}\frac{\partial \mathbf{u}}{\partial z} \tag{2.20}$$

The strain-displacement matrices $\mathbf{B}$ and $\mathbf{S}$ are defined as:

$$\mathbf{B} = \begin{bmatrix} \partial/\partial x & 0 & 0 \\ 0\partial/\partial y & 0 & \\ \partial/\partial y & \partial/\partial x & 0 \\ 0 & 0 & \partial/\partial x \\ 0 & 0 & \partial/\partial y \\ 0 & 0 & 0 \end{bmatrix}, \qquad \mathbf{S} = \begin{bmatrix} 0 & 0 & 0 \\ 0 & 0 & 0 \\ 0 & 0 & 0 \\ 1 & 0 & 0 \\ 0 & 1 & 0 \\ 0 & 0 & 1 \end{bmatrix} \tag{2.21}$$

where the derivatives $\partial/\partial z$ have been left out and unsolved. The vector of strains and curvatures is a function of the rigid body motions:

$$\boldsymbol{\psi} = \mathbf{T}_r\mathbf{r} + \frac{\partial \mathbf{r}}{\partial z}, \qquad \mathbf{T}_r = \begin{bmatrix} & 0 & -1 & 0 \\ \mathbf{0}_3 & 1 & 0 & 0 \\ & 0 & 0 & 0 \\ \mathbf{0}_3 & & \mathbf{0}_3 & \end{bmatrix} \tag{2.22}$$

Equilibrium equations

The principle of virtual displacements states that at equilibrium the total external virtual work per unit length has to be equal to the total internal virtual work per unit length[6]. The work done by the section stresses, $\mathbf{p}_s$, through the virtual displacement $\delta\mathbf{s}$ is the only contribution to the total external virtual work per unit length (see eq. (2.15)):

$$\delta\frac{\partial W_{ext}}{\partial z} = \int_A \frac{\partial \delta\mathbf{s}^T\mathbf{p}}{\partial z}\mathrm{dA} \tag{2.23}$$

with δ as the virtual operator. The total internal virtual work per unit length corresponds to the elastic strain energy of the cross section and consists of the stresses, $\boldsymbol{\sigma}$ along the virtual strains $\delta\boldsymbol{\varepsilon}$:

$$\delta\frac{\partial W_{int}}{\partial z} = \int_A \delta\boldsymbol{\varepsilon}^T\boldsymbol{\sigma}\mathrm{dA} \tag{2.24}$$

The set of second order linear differential equations is obtained when equalizing $\delta\partial W_{ext}/\partial z = \delta\partial W_{int}/\partial z$ and inserting the expressions for the displacement, stresses and strains in eq. (2.23) and (2.24):

$$\mathbf{M}\frac{\partial^2\mathbf{u}}{\partial z^2} + \left(\mathbf{C} - \mathbf{C}^T\right)\frac{\partial \mathbf{u}}{\partial z} + \mathbf{L}\frac{\partial \psi}{\partial z} - \mathbf{E}\mathbf{u} - \mathbf{R}\boldsymbol{\psi} = 0 \tag{2.25a}$$

$$\mathbf{L}^T\frac{\partial \mathbf{u}}{\partial z} + \mathbf{R}^T\mathbf{u} + \mathbf{A}\boldsymbol{\psi} = \boldsymbol{\theta} \tag{2.25b}$$

$$\frac{\partial \boldsymbol{\theta}}{\partial z} = \mathbf{T}_r^T\boldsymbol{\theta} \tag{2.25c}$$

Each of the cross section material property matrices in eq. (2.25a) and (2.25b) are a product of the element connectivity in the 2D mesh and the material properties associated to each finite element. The sizes of the matrices are likewise controlled by the number of 2D FE's in the grid. The matrices are defined as (here presented along their derivatives w.r.t. element material constitutive matrix which will be used for the sensitivity analysis, section 3.3):

$$\underset{(6\times6)}{\mathbf{A}} = \sum_{e=1}^{n_e}\int_A \mathbf{Z}_e^T\mathbf{S}_e^T\mathbf{Q}_e\mathbf{S}_e\mathbf{Z}_e\mathrm{d}A, \qquad \frac{\partial \mathbf{A}}{\partial x_i} = \sum_{e=1}^{n_e}\int_A \mathbf{Z}_e^T\mathbf{S}_e^T\frac{\partial \mathbf{Q}_e}{\partial x_i}\mathbf{S}_e\mathbf{Z}_e\mathrm{d}A \tag{2.26a}$$

$$\underset{(n_d\times n_d)}{\mathbf{C}} = \sum_{e=1}^{n_e}\int_A \mathbf{N}_e^T\mathbf{B}_e^T\mathbf{Q}_e\mathbf{S}_e\mathbf{N}_e\mathrm{d}A, \qquad \frac{\partial \mathbf{C}}{\partial x_i} = \sum_{e=1}^{n_e}\int_A \mathbf{N}_e^T\mathbf{B}_e^T\frac{\partial \mathbf{Q}_e}{\partial x_i}\mathbf{S}_e\mathbf{N}_e\mathrm{d}A \tag{2.26b}$$

$$\underset{(n_d\times 6)}{\mathbf{R}} = \sum_{e=1}^{n_e}\int_A \mathbf{N}_e^T\mathbf{B}_e^T\mathbf{Q}_e\mathbf{S}_e\mathbf{Z}_e\mathrm{d}A, \qquad \frac{\partial \mathbf{R}}{\partial x_i} = \sum_{e=1}^{n_e}\int_A \mathbf{N}_e^T\mathbf{B}_e^T\frac{\partial \mathbf{Q}_e}{\partial x_i}\mathbf{S}_e\mathbf{Z}_e\mathrm{d}A \tag{2.26c}$$

$$\underset{(n_d\times n_d)}{\mathbf{M}} = \sum_{e=1}^{n_e}\int_A \mathbf{N}_e^T\mathbf{S}_e^T\mathbf{Q}_e\mathbf{S}_e\mathbf{N}_e\mathrm{d}A, \qquad \frac{\partial \mathbf{M}}{\partial x_i} = \sum_{e=1}^{n_e}\int_A \mathbf{N}_e^T\mathbf{S}_e^T\frac{\partial \mathbf{Q}_e}{\partial x_i}\mathbf{S}_e\mathbf{N}_e\mathrm{d}A \tag{2.26d}$$

$$\underset{(6\times n_d)}{\mathbf{L}} = \sum_{e=1}^{n_e} \int_A \mathbf{Z}_e^T \mathbf{S}_e^T \mathbf{Q}_e \mathbf{S}_e \mathbf{N}_e \mathrm{d}A, \qquad \frac{\partial \mathbf{L}}{\partial x_i} = \sum_{e=1}^{n_e} \int_A \mathbf{Z}_e^T \mathbf{S}_e^T \frac{\partial \mathbf{Q}_e}{\partial x_i} \mathbf{S}_e \mathbf{N}_e \mathrm{d}A \tag{2.26e}$$

$$\underset{(n_d\times n_d)}{\mathbf{E}} = \sum_{e=1}^{n_e} \int_A \mathbf{N}_e^T \mathbf{B}_e^T \mathbf{Q}_e \mathbf{B}_e \mathbf{N}_e \mathrm{d}A, \qquad \frac{\partial \mathbf{E}}{\partial x_i} = \sum_{e=1}^{n_e} \int_A \mathbf{N}_e^T \mathbf{B}_e^T \frac{\partial \mathbf{Q}_e}{\partial x_i} \mathbf{B}_e \mathbf{N}_e \mathrm{d}A \tag{2.26f}$$

Here, n_e is the total number of FE in the cross section, the summation refers to typical assembly procedure used in FEA, subscript e denotes a specific element and n_d is the total number of degrees of freedom (d.o.f.) in the system calculated as $n_d = 3 \times n_n$ where the number of nodes n_n is multiplied with three nodal displacements ($u_x,\ u_y,\ u_z$).
The displacements, $\mathbf{u}$, are able to replicate the six rigid body motions and eq. (2.18) is therefore 6 times redundant. To ensure that the warping displacements do not contribute to the rigid-body displacements of the cross section the following constraints are included

$$\begin{bmatrix} \mathbf{D}^T & \mathbf{0} \\ \mathbf{0} & \mathbf{D}^T \end{bmatrix} \begin{bmatrix} \mathbf{u} \\ \frac{\partial \mathbf{u}}{\partial z} \end{bmatrix} = \begin{bmatrix} \mathbf{0} \\ \mathbf{0} \end{bmatrix}, \qquad \mathbf{D} = \begin{bmatrix} \mathbf{I}_3 & ... & \mathbf{I}_3 \\ \mathbf{Z}_{xyz_1} & ... & \mathbf{Z}_{xyz_{n_n}} \end{bmatrix}^T \tag{2.27}$$

where $\mathbf{Z}_{xyz_1}, ..., \mathbf{Z}_{xyz_{n_n}}$ are obtianed by inserting the coordinates of the node into eq. (2.16).
The second order linear differential equations (2.25a) to (2.25c) present two types of solutions named *extremity-* and *central*-solutions by Giavotto et al.[29]. For discussions on the solutions the reader is referred to [6], [29] and [8]. The *central*-solution is stated in [8] as:

$$\begin{cases} \mathbf{E}\dfrac{\partial \mathbf{u}}{\partial z} + \mathbf{R}\dfrac{\partial \boldsymbol{\varphi}}{\partial z} = \mathbf{0} \\ \mathbf{R}^T\dfrac{\partial \mathbf{u}}{\partial z} + \mathbf{A}\dfrac{\partial \boldsymbol{\varphi}}{\partial z} = \dfrac{\partial \boldsymbol{\theta}}{\partial z} \end{cases} \tag{2.28a}$$

$$\begin{cases} \mathbf{E}\mathbf{u} + \mathbf{R}\boldsymbol{\psi} = \left(\mathbf{C} - \mathbf{C}^T\right)\dfrac{\partial \boldsymbol{\theta}}{\partial z} + \mathbf{L}\dfrac{\partial \boldsymbol{\psi}}{\partial z} \\ \mathbf{R}^T\mathbf{u} + \mathbf{A}\boldsymbol{\psi} = -\mathbf{L}^T\dfrac{\partial \mathbf{u}}{\partial z} + \boldsymbol{\theta} \end{cases} \tag{2.28b}$$

The stiffness matrix is obtained by putting $\boldsymbol{\theta} = \mathbf{I}_6$ and solving the system of equations. The system presented, with some manipulation and in matrix form, becomes:

$$\begin{bmatrix} \mathbf{E} & \mathbf{R} & \mathbf{D} \\ \mathbf{R}^T & \mathbf{A} & \mathbf{0} \\ \mathbf{D}^T & \mathbf{0} & \mathbf{0} \end{bmatrix} \begin{bmatrix} \mathbf{X} \\ \mathbf{Y} \\ \boldsymbol{\Lambda}_2 \end{bmatrix} = \begin{bmatrix} \left(\mathbf{C} - \mathbf{C}^T\right) & \mathbf{L} \\ -\mathbf{L}^T & \mathbf{0} \\ \mathbf{0} & \mathbf{0} \end{bmatrix} \begin{bmatrix} \frac{\partial \mathbf{X}}{\partial z} \\ \frac{\partial \mathbf{Y}}{\partial z} \end{bmatrix} + \begin{bmatrix} \mathbf{0} \\ \mathbf{I}_6 \\ \mathbf{0} \end{bmatrix} \tag{2.29a}$$

$$\begin{bmatrix} \mathbf{E} & \mathbf{R} & \mathbf{D} \\ \mathbf{R}^T & \mathbf{A} & \mathbf{0} \\ \mathbf{D}^T & \mathbf{0} & \mathbf{0} \end{bmatrix} \begin{bmatrix} \frac{\partial \mathbf{X}}{\partial z} \\ \frac{\partial \mathbf{Y}}{\partial z} \\ \boldsymbol{\Lambda}_1 \end{bmatrix} = \begin{bmatrix} \mathbf{0} \\ \mathbf{T}_r^T \\ \mathbf{0} \end{bmatrix} \tag{2.29b}$$

with Lagrange multipliers $\boldsymbol{\Lambda}_{1-2}$ corresponding to constraints. In short it can be written as:

$$\mathbf{K}\mathbf{W} = \mathbf{F} \Leftrightarrow \begin{bmatrix} \mathbf{K}_{11} & \mathbf{K}_{12} \\ \mathbf{0} & \mathbf{K}_{11} \end{bmatrix} \begin{bmatrix} \mathbf{W}_1 \\ \mathbf{W}_2 \end{bmatrix} = \begin{bmatrix} \mathbf{F}_1 \\ \mathbf{F}_2 \end{bmatrix} \tag{2.30}$$

where

$$\mathbf{K}_{11} = \begin{bmatrix} \mathbf{E} & \mathbf{R} & \mathbf{D} \\ \mathbf{R}^T & \mathbf{A} & \mathbf{0} \\ \mathbf{D}^T & \mathbf{0} & \mathbf{0} \end{bmatrix}, \quad \mathbf{K}_{12} = \begin{bmatrix} \left(\mathbf{C} - \mathbf{C}^T\right) & -\mathbf{L} & \mathbf{0} \\ \mathbf{L}^T & \mathbf{0} & \mathbf{0} \\ \mathbf{0} & \mathbf{0} & \mathbf{0} \end{bmatrix} \tag{2.31}$$

$$\mathbf{W}_1 = \begin{bmatrix} \mathbf{X} \\ \mathbf{Y} \\ \boldsymbol{\Lambda_1} \end{bmatrix}, \quad \mathbf{W}_2 = \begin{bmatrix} \frac{\partial \mathbf{X}}{\partial z} \\ \frac{\partial \mathbf{Y}}{\partial z} \\ \boldsymbol{\Lambda}_2 \end{bmatrix}, \quad \mathbf{F}_1 = \begin{bmatrix} \mathbf{0} \\ \mathbf{I}_6 \\ \mathbf{0} \end{bmatrix}, \quad \mathbf{F}_2 = \begin{bmatrix} \mathbf{0} \\ \mathbf{T}_r \\ \mathbf{0} \end{bmatrix} \tag{2.32}$$

The central solutions are linear and homogeneous such that

$$\mathbf{u} = \mathbf{X}\boldsymbol{\theta}, \qquad \frac{\partial \mathbf{u}}{\partial z} = \frac{\partial \mathbf{X}}{\partial z}\boldsymbol{\theta} \qquad \boldsymbol{\varphi} = \mathbf{Y}\boldsymbol{\theta}, \qquad \frac{\partial \boldsymbol{\varphi}}{\partial z} = \frac{\partial \mathbf{Y}}{\partial z}\boldsymbol{\theta} \tag{2.33}$$

Inserting (2.33) into the central solution (2.28a) and (2.28b) and restating it in matrix form gives eq. (2.34) and (2.35):

$$\mathbf{K}\mathbf{w} = \mathbf{f} \Leftrightarrow \begin{bmatrix} \mathbf{K}_{11} & \mathbf{K}_{12} \\ \mathbf{0} & \mathbf{K}_{11} \end{bmatrix} \begin{bmatrix} \mathbf{w}_1 \\ \mathbf{w}_2 \end{bmatrix} = \begin{bmatrix} \mathbf{f}_1 \\ \mathbf{f}_2 \end{bmatrix} \tag{2.34}$$

where:

$$\mathbf{w}_1 = \begin{bmatrix} \mathbf{u} \\ \boldsymbol{\psi} \\ \boldsymbol{\lambda}_1 \end{bmatrix}, \quad \mathbf{w}_2 = \begin{bmatrix} \frac{\partial \mathbf{u}}{\partial z} \\ \frac{\partial \boldsymbol{\psi}}{\partial z} \\ \boldsymbol{\lambda}_2 \end{bmatrix}, \quad \mathbf{f}_1 = \begin{bmatrix} \mathbf{0} \\ \boldsymbol{\theta} \\ \mathbf{0} \end{bmatrix}, \quad \mathbf{f}_2 = \begin{bmatrix} \mathbf{0} \\ \left(\mathbf{T}_r^T \boldsymbol{\theta}\right) \\ \mathbf{0} \end{bmatrix} \tag{2.35}$$

The matrices $\mathbf{X}$, $\mathbf{Y}$, $\partial\mathbf{X}/\partial z$, and $\partial\mathbf{Y}/\partial z$ have six columns each from each load vector. The relation between these two sets of equations are:

$$\mathbf{w}_1 = \mathbf{W}_1\boldsymbol{\theta}, \quad \mathbf{w}_2 = \mathbf{W}_2\boldsymbol{\theta} \tag{2.36}$$

The external and internal equilibrium from eq. (2.24) and (2.23) is restated with the external work in its complementary form:

$$\delta\boldsymbol{\theta}^T \mathbf{F}_s \boldsymbol{\theta} = \int_A \delta\boldsymbol{\varepsilon}^T \boldsymbol{\sigma} \mathrm{dA} \tag{2.37}$$

The cross section compliance matrix can be defined as:

$$\delta\boldsymbol{\theta}^T \mathbf{F}_s \therefore= \delta\boldsymbol{\theta}^T \begin{bmatrix} \mathbf{W}_1 \\ \mathbf{W}_2 \end{bmatrix}^T \begin{bmatrix} \mathbf{G}_{11} & \mathbf{G}_{12} \\ \mathbf{G}_{12}^T & \mathbf{G}_{22} \end{bmatrix} \boldsymbol{\theta} = \delta\boldsymbol{\theta}^T \mathbf{W}^T \mathbf{G} \mathbf{W} \boldsymbol{\theta} \tag{2.38}$$

where

$$\mathbf{G}_{11} = \begin{bmatrix} \mathbf{E} & \mathbf{R} & \mathbf{0} \\ \mathbf{R}^T & \mathbf{A} & \mathbf{0} \\ \mathbf{0} & \mathbf{0} & \mathbf{0} \end{bmatrix}, \quad \mathbf{G}_{12} = \begin{bmatrix} \mathbf{C} & \mathbf{0} & \mathbf{0} \\ \mathbf{L} & \mathbf{0} & \mathbf{0} \\ \mathbf{0} & \mathbf{0} & \mathbf{0} \end{bmatrix}, \quad \mathbf{G}_{22} = \begin{bmatrix} \mathbf{M} & \mathbf{0} & \mathbf{0} \\ \mathbf{0} & \mathbf{0} & \mathbf{0} \\ \mathbf{0} & \mathbf{0} & \mathbf{0} \end{bmatrix} \tag{2.39}$$

The final expression for the compliance matrix is:

$$\mathbf{F}_s = \mathbf{W}^T \mathbf{G} \mathbf{W} \tag{2.40}$$

and the cross section stiffness matrix is:

$$\mathbf{K}_s = \mathbf{F}_s^{-1} \tag{2.41}$$

2.4 Comparison to experimental results

To gain experience with BECAS and validate that the desired BTC effects can be captured by FRANS, a comparison is made with findings in literature which is presented below.

A very common cited article for validating composite beam formulations is the one of Chandra et al. [15]. In this study, the authors experimentally showed BTC effects in thin walled composite beams and compared them to their own analytic predictions and a newly formulated FEM by Stemple and Lee [62]. The beams investigated had a symmetric layup $[\theta]_6$ in the flanges and symmetric cross-ply layup $[\theta/-\theta]_3$ in the webs. The annotation $[\theta]$ is common practice and simply specifies the laminae angles such that a laminate with 3 plies with 0, 15, and 30 degrees for their fiber orientation respectively will have the annotation [0/15/30]. The subscript in the annotation is how many times the layup is repeated. In the study, each ply had a thickness of 0.127mm i.e. faces and webs thickness' are 0.76mm. The outer cross section dimensions are 24.2mm for the width and 13.6mm for the height. The length of the beam is 762mm and the material is AS4/3501-6 Unidirectional Graphite/Epoxy with properties $E_{11} = 142$GPa, $E_{22} = E_{33} = 9.81$GPa, $G_{12} = G_{13} = 6$GPa, $G_{23} = 3.77$GPa, $\nu_{12} = \nu_{13} = 0.3$, and $\nu_{23} = 0.42$ taken from Stäblein et al.[59] since the material properties in Chandra et al.[14] are insufficient. Unfortunately, the stiffness matrix presented by Stäblein et al. cannot be reproduced exactly as stated in the article, although the same program is used to obtain it (BECAS). It is suspected that material properties, number of FE, and conversion between the coordinate system used in the paper and by BECAS plays a role. Discrepancies of the material properties have been found in the PhD thesis of Couturier[20] where shear modulus and Poisson's ratio differ from the ones presented by Stäblein et al. The present obtained cross section stiffness matrix and the one presented in Stäblein et al.'s article are compared in the appendix page 76.

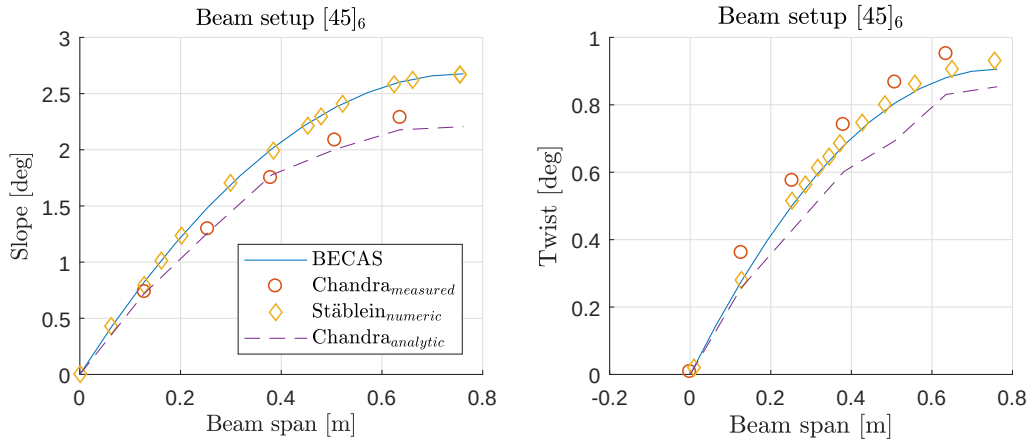

Figure 2.6: *Comparing numeric and analytic results with reported measurements from Chandra et al. [14] and numeric values from Stäblein et al.[59].*

Using GMSH[28] (shortly introduced in section 2.5.1), the thin walled composite beam cross section is discretized into 8737 Q4 elements (linear rectangular four node plane element) and a self-defined routine, imports the 2D grid into BECAS. Applying a tip load of 4.448N, the bending slope and twist rate is determined and compared with digitized results reported in [59] and digitized measurements and an analytic method from [14] in figure 2.6 for a beam layup of $[45°]_6$ in the flanges and $[\pm 45°]_3$ in the webs.
In the comparison, in figure 2.6, a good correlation is observed. The analytic data was made using the method presented by Chandra et al. [15] and Hong and Chopra [32] and the theory

is reproduced in the appendix, page 75. The numeric results are coherent with the results and conclusion made by Chandra et al.[15]: that is, the analytic methods underpredict the actual composite beam twist response, whereas numerical methods show better agreement with measurements. This being the importance of including transverse shear which is not captured by the analytic solution. The numeric results of the bending slope is up to 15% off, which contribute to production errors since in practice ensuring correct fibers angles is quite difficult. The bending slope results coincide with those of Stäblein et al.'s and is accepted as is.

2.5 2D meshing

Any 2D-structure can be discretized into small 2D elements that together are called a grid or a mesh due to the visual appearance, see e.g. 2.7b. The FE-method is an approximation of the physical state of a material and can converge to the true state as FE's decrease in size and thus increase in numbers. A high number of elements in the cross section mesh will improve accuracy but will increase the computational costs since the system of equations representing the equilibrium (eq. (2.12)) will increase. This dispute can only be solved with a compromise, usually determined by a convergence study which is the most important and usually also the most omitted step associated with any FE-analysis. A successful convergence study will result in a 2D discretisation that contains the best ratio of accuracy and computational cost. It is obtained by gradually increasing the number of elements in the mesh until the response (deflection, stresses, frequencies, etc.) reach a steady value e.g. below 1% change. The following two sections presents the 2D discretisations of a simple cantilever sandwich beam, used in the parametric study, and the 10MW DTU reference WTB, used for the full blade optimization.

2.5.1 Simple beam

BECAS allows for 2D quadratic elements with 4 or 8 nodes (Q4 and Q8 respectively) and for triangular elements with 6 nodes (T6). The higher number of nodes allows for higher order shape functions. The parametric study is designed to test the framework of the optimization and computational costs are valued higher than accuracy in this case for faster function evaluations i.e. Q4 elements are selected. Furthermore, the composite beam exhibits a fairly simple cross section and no extraordinary deformations are expected which require higher order elements.
A sandwich cantilever beam presents a uniform cross section all along its span, thus only a single mesh is needed that can be extrapolated to the remaining length. The beam dimensions is presented in chapter 4 as well as the load case. The mesh is made with the software GMSH[28] (pronounced g-mesh), which is an open-source 3D FE grid generator, however, in this case only used to create 2D meshes. The mesh is defined in an input file, and GMSH draws and mesh the geometry based on the points, lines, and connections specified in the file. The input file for a cross section 2D mesh used for the parametric study of a cantilever sandwich beam is attached in the appendix, page 78.

To exclude mesh dependency, a convergence study is performed, that considers the tip end beam deflection as response. By gradually increasing the number of elements used to discretize the cross section, the converged result should show a horizontal line with a max of 0.5% difference between response values. The result of the convergence study is plotted in figure 2.7a and presents a converged result with 728 elements. The number of beam elements used for the convergence study was 10 and no BTC was introduced in the beam.

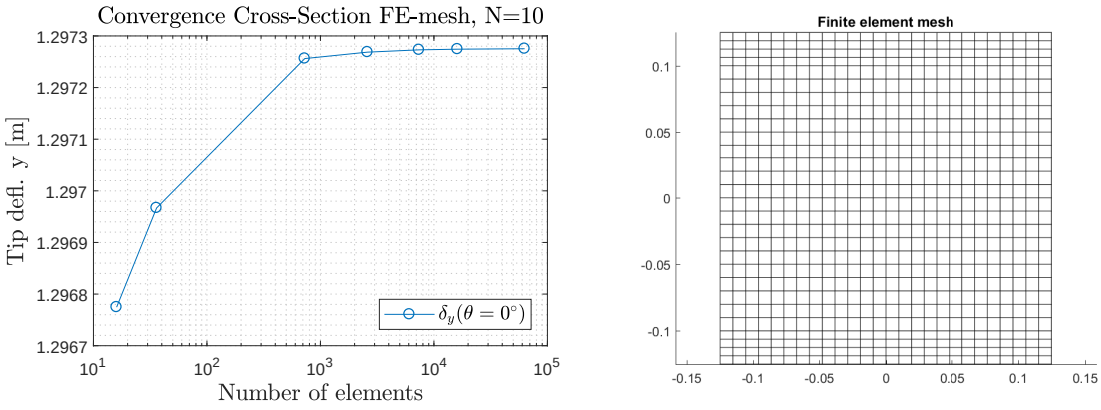

(a) *Convergence history* **(b)** *Cross section FE=728*

Figure 2.7: *Mesh convergence of beam end node displacement with 10 beam elements and fiber angles in the faces set to null. The beam dimensions and load case are presented in chapter 4*

A beam element convergence study was also performed, which showed no change in response value (using 728 cross section Q4 elements) going from 3 to 20 beam elements. The plot has been omitted of this report since it is trivial to show a horizontal line.
Lastly, a note on the choice of mesh type. Typically, a choice is made between unstructured and structured meshes, where the latter is presented in figure 2.7b. Besides being visibly more appealing, the structured mesh poses no benefits over an unstructured one for this type of cross section, whereas an unstructured mesh is more appropriate when discretizing circular shapes and sharp corners.

2.5.2 Wind turbine blade

The cross section geometry of an airfoil is significant more complex than that of a simple sandwich cantilever beam. The thin laminates pose a risk of FE's with high aspect ratios as they are pushed flat and a known problem with these kind of elements is shear locking. The DTU10MW reference WTB is used in this thesis study, and very conveniently, 27 cross section meshes can be created using the Abaqus model[21] and a python program called shellexpander.py, which is distributed along with BECAS. A limitation of using shellexpander is the loss of control of the mesh, since only the discretization through thickness, i.e. number of layers, is adjustable for the user. Shellexpander reads the input files for Abaqus of the DTU10MW reference WTB, and expands a FE layered shell model by building layers from outer FE shell boundary (as for airfoil geometry) or from mid-thickness line (as for webs). The program will create a 2D mesh of any specified number of cross sections and provide it in correct format for BECAS along material numbers and orientation.

A few of the meshes are presented in figure 2.8. The presented cross section meshes has approximately 500 Q8 elements each for a chosen through thickness number of layers of $nlse = 8$. Shellexpander.py has a lower limit of $nlse$ which is the minimum number of different layers in a part of the blade e.g. caps. If the cap is build by three different layers/composite materials, the lowest vaue of $nlse = 3$ to be able to discritize the elements. No upper limit exit, however, one has to take into account the increased computational burden.

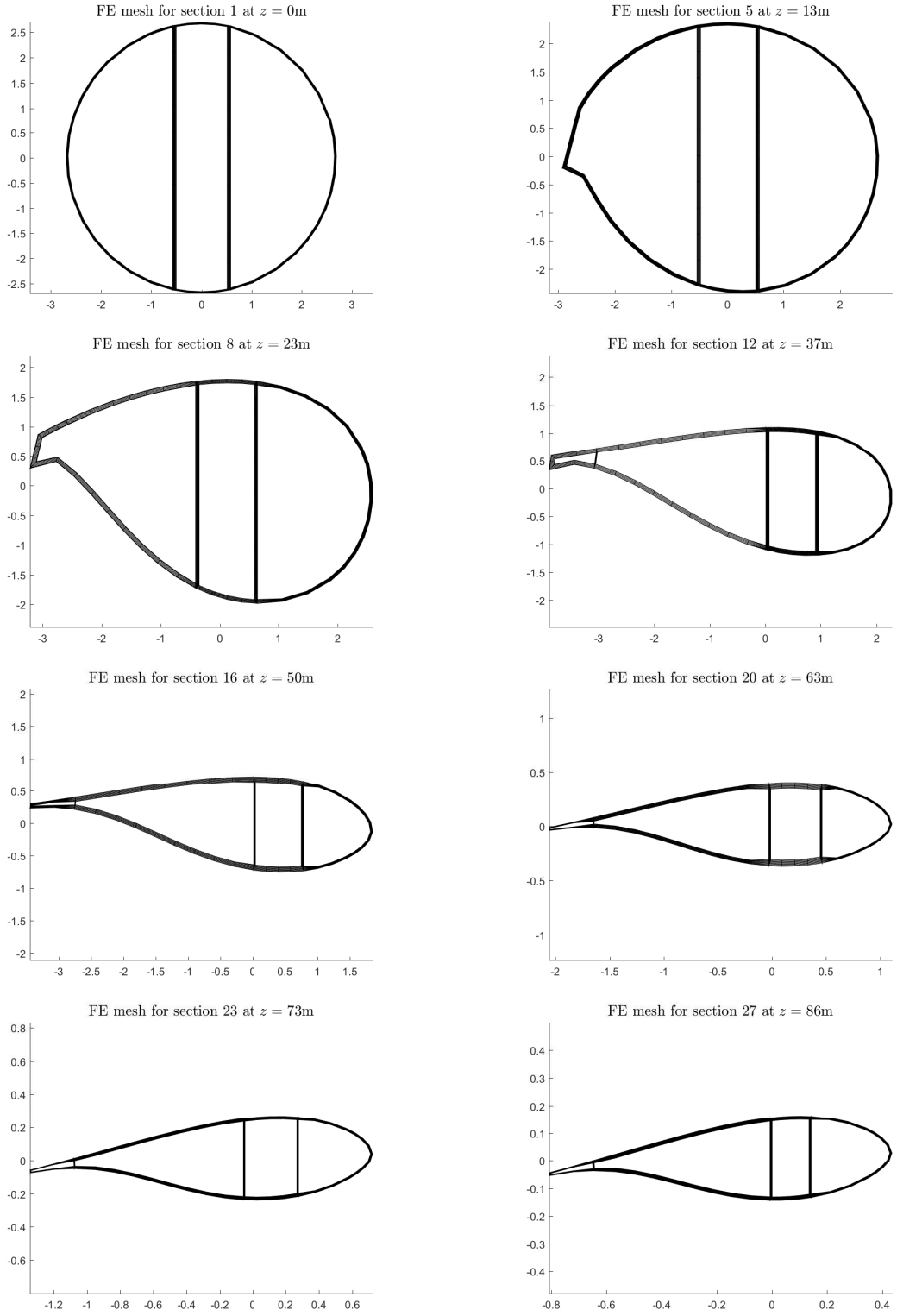

Figure 2.8: *Selected cross section FE mesh of the DTU10MW reference WTB.*

2.5.3 Element patches

Element patches are a grouping of FE in the cross section grid that exhibit the same material and fiber angle and is affected by the same design variable. This is an effective way of reducing the computational cost and can also give a more realistic image of how the laminate layup is in a WTB. Practically, the patches can either be for a single ply in the laminate, multiple plies in the laminate or entire sub-parts of the WTB cross section e.g. the pressure side cap or the leading edge web, thus both a material and geometric dependence. It can also be expanded to embrace spanwise distributions. In this study, to keep the computational costs down, the elements in the WTB cross section are patched together based on the location such that caps, webs, shells, etc. are well defined in the cross section grid. This results in remarkably fewer design variables and allows for analysis where only fiber angles in e.g. the cap is allowed to change, and the modified subpart resulting in highest BTC effects can be identified.

2.6 Loads

The loads applied to the DTU10MW reference WTB are taken from the DTU10MW reference wind turbine report [3] and consist of 14 load cases, computed with the aeroelastic code HAWC2[38] in accordance with the IEC-61400 standard. Each load case presents the extreme of a internal force or moment related to the elastic center at 27 sections along the blade span, collected from simulations in time domain under various conditions. The load case selected for this study contains the maximum absolute flapwise bending moments including a respective partial safety factor of 1.35, which were present for the Design Load Basis (DLC) 1.3 that denotes an Extreme Turbulence Model (ETM). The ETM express a more turbulent wind field with larger variance in direction and magnitude of the wind. Large gusts are therefore more frequent, and give rise to large blade deflections. Since the pitch controller system is unable to react fast enough to alleviate deflection and loads caused by gusts, the BTC mitigation effects should be clear during this extreme environment. The choice of this load case is motivated by the optimization problem definition: to obtain maximum coupling in the blade while considering a maximum tip deflection constraint and structural integrity in the form of eigenfrequency- and material failure criteria constraints. Choosing the highest loads may hinder the amount of coupling possible in the blade due to the different constraints, however, the optimal design will be conservative. Figures 2.9 and 2.10 presents the internal forces and moments of the load case with maximum absolute flapwise moments. Of the six internal forces presented for load case 9, only the moments M_x and M_y will be used to calculate distributed external forces and provided to FRANS. The main loads on a WTB is the flapwise bending moment, from the wind, and the edgewise bending moment, from the gravitational pull and lift force (see airfoil sketch in the appendix page 75). Shear forces, axial force and torsion is relevant, however, significantly lower than the flapwise bending moment, see M_x at figure 2.10. Furthermore, including torsion loads will influence the BTC coupling effects, and to keep it simple it is excluded. Using edgewise bending moments may introduce edgewise BTC effects, however, it is believed that this can be handled by appropriate selection of element patches. Another argument for including edgewise bending moments, is that the WTB should present the BTC effects even with edgewise loading, otherwise, the desired response might be reduced or be dependent on the azimuth position of the blade.

Unfortunately, FRANS does not support applied internal forces but can only handle external forces, thus, the loads must be approximated using beam equations. The method used here is taken from [13] and the equations can be found in e.g. [63]. The following beam equations are used:

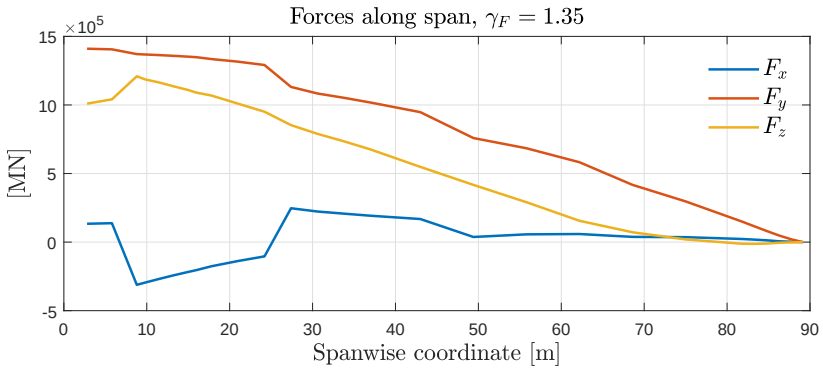

Figure 2.9: *Internal forces along blade span for load case 9 from [3]*

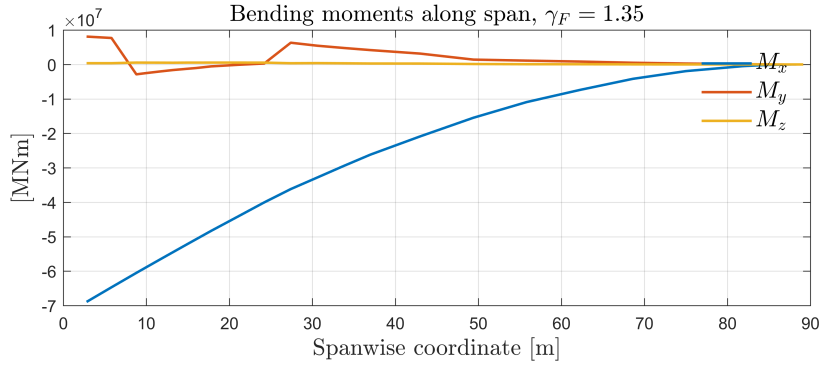

Figure 2.10: *Internal moments along blade span for load case 9 from [3].*

$$T_x = -\frac{\mathrm{d}M_y}{\mathrm{d}z}, \qquad T_y = \frac{\mathrm{d}M_x}{\mathrm{d}z}, \qquad q_x = -\frac{\mathrm{d}T_x}{\mathrm{d}z}, \qquad q_y = -\frac{\mathrm{d}T_y}{\mathrm{d}z} \tag{2.42}$$

The moments M_x and M_y in eq. (2.42) are table values from the DTU10MW reference wind turbine report [3], see table 2.2. The table shows the extreme internal forces at a section z=24.2 m, collected from various time domain simulations. The values used are thus the highest absolute values from a range of simulations although highly unlikely that the turbine blade will experience all the extreme bending moments simultaneously. This makes for a conservative load case and thus a conservative optimal design.
Using the values for the extreme bending moments around $x-$ and $y-$axis for load case , the shear forces, T_x and T_y in the WTB are approximated with eq. (2.42) by taking the derivative of the a 3^{rd} order polynomial fit to bending moments. The distributed load, that can be applied to the FE beam model by FRANS, is then obtained by taking the derivative of the shear forces. Figure 2.11 shows the work flow for load case 9.
One could question whether a polynomial fit to the shear forces listed in the DTU10MW reference wind turbine report could have been sufficient such that the first step is skipped and a better fit is obtained. Nevertheless, this method is suitable and shows good consistency with deflection values e.g. the maximum tip deflection is reported by [3] to be 12.4m for the DLC 1.3 case, and using the extreme values for flapwise bending moment in load case 9 and the method outlined above, the tip displacement is calculated to be 13.51m with no modifications to the original blade design and thus comparable to the original reported maximum. The difference can be rooted in the not so perfect fit seen in figure 2.11 and the difference in between software used to obtain the tip displacement. The reported maximum tip displacement in the

Table 2.2: *Extreme internal loads collected from various simulations in time domain according to IEC-61400 standard at section number 11 $z = 24.2$ m, takes from [3]. The extreme resultant force and moments have been left out, thus the missing case number 7.*

Load case		DLC	γ_F [-]	F_x [MN]	F_y [MN]	F_z [MN]	M_x [MNm]	M_y [MNm]	M_z [MNm]
1	F_x max	dlc1.3	1.35	0.6201	0.5670	1.3796	-6.3263	11.7007	0.2098
2	min	dlc1.3	1.35	-0.5978	-0.0194	1.3335	2.0900	-14.4587	-0.6439
3	F_y max	dlc1.3	1.35	0.4443	1.4147	1.0644	-33.2051	7.3193	0.2831
4	min	dlc6.2	1.1	0.1081	-1.0553	0.0802	25.7233	3.3898	0.6537
5	F_z max	dlc2.1	1.35	-0.2329	0.4912	2.1765	-15.2363	-6.0230	-0.1670
6	min	dlc6.2	1.1	-0.0725	-0.7945	-0.5227	18.5518	-0.1156	0.3236
8	M_x max	dlc1.3	1.35	0.0195	-0.7359	1.7650	26.5539	1.6363	-0.0493
9	min	dlc1.3	1.35	0.1795	1.3249	0.9077	-40.5149	4.9810	0.4500
10	M_y max	dlc2.1	1.35	0.5768	-0.1117	1.3012	11.3194	16.3736	0.5579
11	min	dlc1.3	1.35	-0.5956	-0.0447	1.3338	2.9221	-14.5158	-0.6619
12	M_z max	dlc6.2	1.1	0.1860	-0.9590	-0.3510	26.1955	6.1252	0.9005
13	min	dlc1.3	1.35	-0.4174	-0.0746	1.5220	6.9106	-13.2988	-0.9337

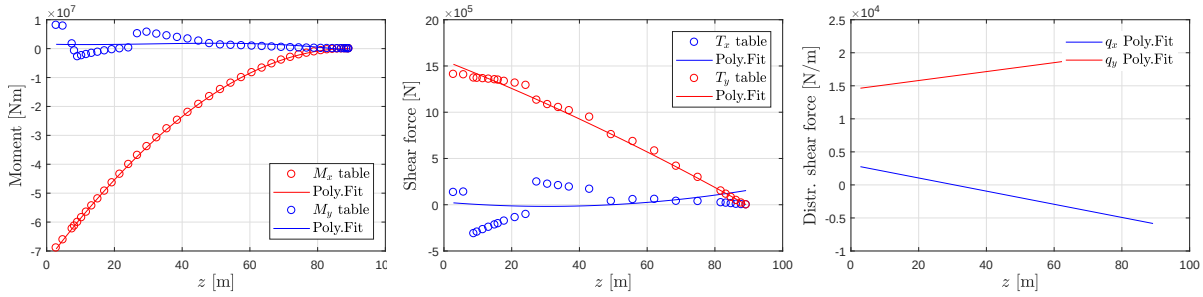

(a) *Moment table values* **(b)** *Shear force* **(c)** *External load*

Figure 2.11: *Extreme internal moment loads from table values fitted with polynomials and converted to external distributed loads.*

DTU10MW reference wind turbine report[3] was obtained with HAWC2 while the presently presented was obtained with BECAS via FRANS.
The extreme internal loads can be used directly with BECAS to evaluate the cross section element strains, stresses and failure indexes based on appropriate failure criteria which will be treated in section 3.2.2. However, FRANS contains a module to extract the internal forces and moments based on the FE beam deflection and rotations, see eq. (2.43). The vector, $\boldsymbol{\theta}$, contains the internal forces and moments w.r.t. beam element b as the subscript denotes. Furthermore, the forces and moments can be transformed to another point e.g. shear center, and rotated to fit the elastic axis, also provided in FRANS routines. A comparison is made, using the internal forces and moments from above with the ones recovered using the FRANS module which is presented in figure 2.12. In the figure, it is observed that the internal forces retrieved with FRANS does not correspond and in fact presents errors up to approximately 100% for the flapwise moments which for this study is the most important one. Transforming them w.r.t. shear center and rotating to elastic axis provides little to no change. In this study, the forces and moments recovered from FRANS will be used when evaluating the strains and stresses

$$\boldsymbol{\theta} = \mathbf{K}_b \mathbf{u}_b \tag{2.43}$$

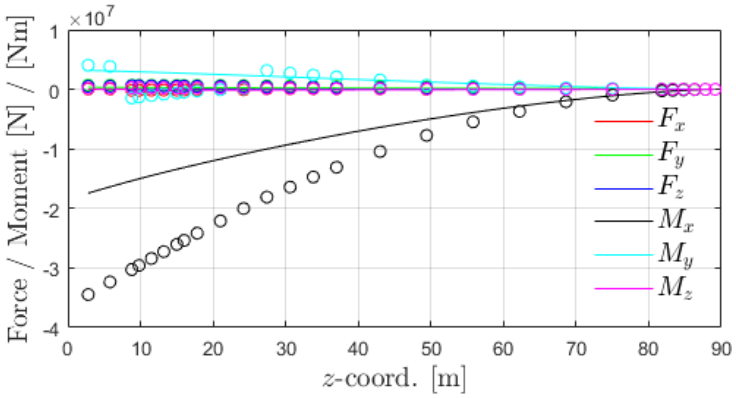

Figure 2.12: *Comparison of internal forces. Circles are table values from [3] while solid lines are internal forces retrieved from FRANS for original blade design.*

Designing WTB's in the industry, all DLC's must be taken into account i.e. a lot more load cases for the optimizing algorithm to handle, however, since this is a proof-of-concept study it is not needed here. Including all DLC's would increase the computational costs greatly and might also hinder convergence to optimum design.

CHAPTER 3

Formulation of optimization problem

It is the aim of any structural optimization to minimize (or maximize) an objective function, dependent on design variables, and subject to constraints. The optimal solution to the problem is the values of the design variables when no change in them can benefit the objective function. This chapter presents the problem formulations investigated for the use in this study, discussions on the considered objective functions and constraints, discussions on the optimization algorithms considered, the sensitivity analysis, and presentation of some of the changes and implementations made to BECAS.

3.1 General problem formulation

The standard negative null form of an optimization problem can be observed in eq. (3.1). It presents an objective function $f(\mathbf{x})$, dependent on the design variables $\mathbf{x}$. The objective function must be minimized while complying with the in-equality constraints $\mathbf{g}(\mathbf{x})$ and equality constraints $\mathbf{h}(\mathbf{x})$. The direction of the inequality sign for $\mathbf{g}(\mathbf{x})$ and the zero on the r.h.s. is what makes it a negative null problem (see appendix page 80 for other forms). Defining the right problem formulation is essential for the quality of the optimum final result, thus if objective and constraints are not carefully selected, either convergence to local minimum may occur or not convergence at all. The optimal design of a WTB for BTC effects is sought, meaning that the twist response to flapwise loading is desired as large as possible while considering structural integrity constraints. Since the desired blade response is a twist in the negative rotational direction around the z-axis of the blade, a minimization will push the design to a greater twist response. It should be stated that for non-convex problems, global optimum cannot be guaranteed. The objective function can be a combination of several objectives, which are weighted and summed according to the desired influence on the final design: $\sum f_i w_i$. The design variables are bound by the upper and lower limit x_{max} and x_{min} respectively. The sets of functions in $\mathbf{f}$, $\mathbf{g}$ and $\mathbf{h}$ can be linear or nonlinear, however, they should preferably be twice differentiable and as a minimum one time differentiable in order to use gradient based optimization algorithms.

$$\begin{aligned} \min_{\mathbf{x}\in\mathbb{R}} \quad & f(\mathbf{x}) \\ \text{s.t.} \quad & \mathbf{g}(\mathbf{x}) \leq 0 \\ & \mathbf{h}(\mathbf{x}) = 0 \\ & x_{min} \leq x_i \leq x_{max} \quad \forall i = 1, ..., n_{dv} \end{aligned} \tag{3.1}$$

An important discipline within optimization is the scaling of parameters. Large differences in parameters may lead to badly condition and singular matrices and a volatile design domain. Many optimization algorithms make use of line search, which is a method to chose a new design point, which can overshoot significantly if the design domain is badly scaled. The parametric study (chapter 4) and the full blade optimization (chapter 5), have been observed to give slightly better performance (less function evaluations needed for convergence) and robustness depending

on scaling of design variables and objective and constraint values. Scaling of variables is of less importance if the values already lie close to unity.

3.2 Objective and constraint functions

The objectives and constraints considered for this thesis work are governed by the ambitions in the wind energy industry: to build longer WTB's while ensuring the structural integrity. In this study the below listed parameters in table 3.1 has been considered and implemented as objective and/or constraints:

Table 3.1: *Considered parameters for objectives and constraints for the optimization problem formulation. N is number of cross sections, n_λ is number of eigenfrequencies considered in the study, $\mathbf{x}_{dv}$ is a vector with the design variables directly associated with a particular cross section, n_p is number of patches*

Parameter	Obj.	Constr.	Constr. notation	
Compliance	√			
Tip displacement	√	√	$u_y^{tip}(\mathbf{x}) - \left(u_y^{tip}\right)^{max} \leq 0$	
Tip twist	√	√	$u_\varphi^{tip}(\mathbf{x}) - \left(u_\varphi^{tip}\right)^{max} \leq 0$	
BTC factor	√	√	$\alpha_n(\mathbf{x}) - \alpha_n^{max} \leq 0,$	$\forall n = 1, ..., N \vee x_i \in \mathbf{x}_{dv}$
Eigenfrequencies		√	$f_j^{min} \leq f_j(\mathbf{x}) \leq f_j^{max},$	$\forall j = 1, ..., n_\lambda$
Failure criteria		√	$FI_p^{min} \leq FI_p(\mathbf{x}) \leq FI_p^{max},$	$\forall p = 1, ..., n_p \vee x_i \in \mathbf{x}_{dv}$

Other possible options for objectives could be to minimize the stresses in the structure, minimize root bending moments, minimize mass, or maximizing lowest eigenfrequencies. Due to the minimization formulation, the optimization algorithms will minimize the objective and therefore one should choose objective where the minimum is sought. Maximization, when mentioned in this thesis paper, is therefore meant as maximizing the blade twist response and not maximizing the numerical value of the objective function.
The constraints considered for this thesis work are purely in-equality constraints. Equality constraints certainly have their place, especially if a certain response is sought e.g. end twist of -5°. However, to limit the already vast possible problem formulations with the considered objective and constraints, it was determined to leave equality out of this thesis study.

The above constraints are all deemed relevant for a WTB's structural integrity and covers many of the aspects that must be controlled for the blade to be approved by e.g. international standards, certification bodies and authorities. The list is far from exhausted as many other constraint to WTB's exist: fatigue damage, buckling, logistic constraint, manufacturing constraint, etc.

Compliance

Usual topology optimization use the static compliance to minimize the volume e.g. mass and obtaining a stiff structure. The compliance is defined as the external work done on the structure by external static loads and is calculated as:

$$C = \mathbf{p}^T\mathbf{u} = \mathbf{u}^T\mathbf{K}_g\mathbf{u} \tag{3.2}$$

where $\mathbf{u}$ and $\mathbf{p}$ is the beam nodal displacements in each d.o.f. and loads respectively and $\mathbf{K}_g$ is the global FE beam stiffness matrix. The compliance is not considered as a constraint since

knowledge of compliance values prior to optimization is needed to set the bounds.

Tip displacement

The tip displacement as an objective function will be minimized by increasing the stiffness of the WTB. Here the tip displacement is in the flapwise direction i.e. positive y-axis direction (see e.g. figure 1.2). By only considering deflection in a single direction for the tip of the blade, a single objective value is obtained and no summation over weighted values is needed. By minimizing the flapwise tip deflections, the design must present a high stiffness, which is desirable in a WTB due the clearance between the blade tip and the tower of the wind turbine. With increasingly longer blades, the higher stiffness is required to keep the blade tip clear of the tower. To obtain high stiffness, the fiber angles must align with the WTB spanwise axis and thus oppose e.g. constraints on the minimum twist desired for the blade.
Tip displacement as a constraint is argued to be a crucial one. Without limitations to the tip displacements, the blade is in severe risk of hitting the tower during high loads and gusts. Furthermore, logistic issues such as demolding and transportation is impossible with too low flapwise bending stiffness in the blade. The tip displacement as a constraint is determined the same way as described for the tip displacement as objective function. The flapwise displacement in the positive y-direction of the tip of the blade can be extracted from the global FE beam equilibrium equation, established by FRANS, by solving for the beam element displacement field. The full displacement field is calculated by solving the equilibrium equations (2.12) such that:

$$\mathbf{u} = \mathbf{K}_g^{-1}\mathfrak{p} \tag{3.3}$$

The tip displacement is the second d.o.f. of the end node in the beam FE displacement field $\mathbf{u}$. To elaborate, an all null vector, $\mathbf{e}$, with the length equal to the length of $\mathbf{u}$ is defined. On the k^{th} entry, the element in the vector is $\mathbf{e}_k = 1$ corresponding to the d.o.f. one wish to extract. The k^{th} d.o.f. is obtained by the dot product:

$$u_y^{tip} = \mathbf{e}^T \cdot \mathbf{u} \tag{3.4}$$

where u_y^{tip} is the beam tip deflection in the y-direction.

Tip twist

To observe the amount of twist towards feather possible for the WTB, the end twist is considered as an objective. The optimization algorithm will then find the fiber angles resulting in the maximum obtainable twist, if no active constraints are present. If constraint are applied they might limit the amount of twist obtainable depending on the constraint values.
The tip twist as an in-equality constraint is used to limit the twist response of the WTB and thus the orientation of the fibers. Defining an upper and/or lower bound will allow for the tip twist to obtain a value in the desired range.
The tip twist is found, as with the tip displacement, from the solution to eq. (3.3) and then extracting the correct d.o.f. (last one) from the displacement field vector $\mathbf{u}$:

$$u_\varphi^{tip} = \mathbf{e}^T \cdot \mathbf{u} \tag{3.5}$$

where u_φ^{tip} is the beam tip twist around the z-axis.

BTC factor

The BTC factor, as defined in eq. (2.9), is a possibility as an objective for maximizing the twist response. For a prismatic cantilever beam with uniform cross sections along its span, only a single BTC factor is considered since the cross section is uniform. However, with various and multiple cross sections, the objective function will be a weighted function with elements for each unique cross section. In relation to the coordinate system BECAS uses, the BTC factor is defined as:

$$\alpha^{(n)}(\mathbf{x}_{dv}) = \frac{K_{46}^{(n)}(\mathbf{x}_{dv})}{\sqrt{K_{44}^{(n)}(\mathbf{x}_{dv})K_{66}^{(n)}(\mathbf{x}_{dv})}}, \qquad n = 1, ..., N \tag{3.6}$$

where superscript n denotes a specific cross section of the structure. The BTC factor is only dependent on the design variables directly associated with the current considered cross section n, and thus the design variables $\mathbf{x}$ are presented with a subscript dv to denote this dependency i.e. $\mathbf{x}_{dv}$ is a vector containing the relevant design variables. The diagonal stiffness terms K_{44} and K_{66} from the cross section stiffness matrix is for the flapwise bending stiffness and torsional stiffness respectively. The off-diagonal stiffness term K_{46} is the flapwise bending-torsion coupling. For the full stiffness matrix and nomenclature see appendix page 83. The sign of K_{46} denotes which direction the structure will twist i.e. negative value will result in negative rotation direction around beam axis. Maximization of the twist response is thus equivalent to minimizing the BTC factor for each considered section (recall that a negative twist will result in the blade twisting towards feather). To combine the several values into a single objective value a weighted summation can be used:

$$\alpha(\mathbf{x}) = \sum_{n=1}^{N} w^{(n)}\alpha^{(n)}(\mathbf{x}_{dv}) \tag{3.7}$$

where the weighting parameters, $w^{(n)}$, are selected to control the influence of the different BTC factors and could for example take values in the range $w^{(n)} \in [0; 1]\forall n$. The weighting parameters are not a function of the design variables. Combining the different coupling factors for each section into a single one, makes the factor a function of all design variables.
For a WTB with large difference in cross section properties, it will be time consuming to tune all the weighting factors. A benefit from this, however, is control of the location of high BTC effects along the blade. For example, at the root end, where the effects of the off-axis fiber angles contribute less to the end twist due to its circular shape but presents highly reductions in bending stiffness i.e. increasing tip deflection , it is undesirable to introduce BTC[10]. For the full blade optimization, a spanwise section from root to a z-coordinate out towards the tip, will not be considered for BTC. When considering BTC factor of multiple unique sections, it has been chosen to have an uniform weighting. This way, the optimizer will have to sought out the benefits and disadvantages of having large material couplings near root rather than mid-span and tip regions. Doing this, another advantage is that the optimal design will not be affected by earlier conceptions of how the distribution should be.

3.2.1 Eigenfrequencies

Eigenfrequencies of WTB's are an important aspect of their design requirements. Depending on the frequencies, severe damage or catastrophic failure may occur due to resonance or instabilities. The change in fiber angles introduce a reduced bending stiffness which changes the mode shapes. The interaction between the aerodynamic forces and the blade can in extreme cases lead to

negative aerodynamic dampings, as shown by Petersen et al. [54]. Another aspect is the coupling between flapwise frequencies and torsional frequencies which might create a flutter instability. Therefore, the distance between eigenfrequencies is controlled by selecting upper and lower bounds for individual eigenfrequencies. The classical formulation in FE theory for the structural eigenvalue problem is[6]:

$$\left(\mathbf{K}_g - \omega_j^2 \mathbf{M}_g\right) \mathbf{v}_j = 0, \qquad j = 1, ..., n_d \tag{3.8}$$

where n_d is the number of degree of freedom and $\mathbf{K}$ and $\mathbf{M}$ is defined in section 2.3.2. The matrices are assumed positive definite and symmetric. The eigenvalue problem above yields the eigenvalues $\boldsymbol{\omega}$ linked with the corresponding eigenvectors $\mathbf{V} = \left[\mathbf{v}_1, ..., \mathbf{v}_{n_{dof}}\right]$ and are provided in ascending order i.e. $\omega_1 \leq \omega_2 \leq \cdots \leq \omega_{n_{dof}}$.

Multiple frequencies can be handled with either a constraint such that the subsequent eigenfrequency must be 10-20% larger than the preceeding one: $\lambda_{j+1} = \lambda_j * 1.2$ or with method described by Seyranian et al.[56]. The conversion from eigenvalue to eigenfrequency ([rad^{-2}] to [Hz]) is $\lambda_j = \sqrt{\omega_j}/(2\pi)$.

3.2.2 Failure criteria

The failure of a material may be characterized as the instant the material partly or fully lose its load carrying abilities. In a composite material, this may occur in a number of ways not limited to delamination, fiber-pull-out, core failure, single ply failure, buckling, and ultimate failure where the strain or stresses internally in the composite exceeds their limits and the structure is tared apart. Due to their complexity; fatigue failure, crack propagation, delamination, buckling, and fiber-pull-out, are not considered in this study. Since the strength is very directional for a composite, maximum strain (Max Strain), maximum stress (Max Stress), and other common failure criteria such as Tsai-Wu and Tsai-Hill are instead considered. These failure criteria are able to, based on material experimental data, estimate the failure of laminae. Furthermore, by using mentioned failure criterias no scaling of the constraints are needed since failure criterias usually have values around one. In a FE mesh, every element exhibits its own strain and stress i.e. the number of Failure Index(es) (FI), which is the numeric output from a failure criteria, is equal to n_e. All of the failure criterias presented below can be found in e.g. [34], [36] or [72].
In context of optimization, stresses have long seen their use. It was quickly discovered that stress constraints pose multiple problems: not only does the number of constraints increases significantly, but, the optimization might results in a local minima being unable to reach true optimum. This was first illustrated with a 3 bar truss system, defined by Sved and Ginos [64], where the true optima could only be achieved by removing one of the bars. This was not possible due to the stress constraint. In weight optimization of truss structures, decreasing the cross sectional area of a beam increases the stress in it, leading to intermediate grey designs, and the bar cannot be removed. This is known as the stress singularity. Cheng and Guo [18] introduced a relaxed method that solved the optimization problem iteratively, called the epsilon-method. Whether this problem arises in laminate designs has been discussed and proved by Bruyneel and Duysinx [12] and occurs with the removal of zero thickness plies.
In this study, the geometry and thickness is fixed, thus removing plies will not occur. The stress singularity is therefore not suspected to occur.

The large amount of constraints can be handled by considering aggregation functions. Duysinx and Sigmund [25] introduced a global stress measure using P-norm methods and doing so reduced the local stress constraints to a single global constraint but resulted in problems

controlling the stress at a local level. Verbart et al. [67] states that P-norm and P-mean aggregation functions usually are used to aggregate non-negative stress criteria, such as the von Mises stress, into a global function (see Le et al. [39] and Holmberg et al [31]). The fact that P-norm and P-mean are restricted to non-negative values is not a problem, since failure criteria are used which results in values larger than zero. If a FI is larger than 1, the material fails. Alternatively, the Kreisselsmeier-Stainhauser can be used, which is not restricted to non-negative values.

The patching of elements are used to reduce the amount of fiber angles subject to change in the full blade study, however, it has a second benefit in the form of reduced number of FI's needed as stress constraints. Instead of the mentioned aggregation functions above, the maximum FI of a patch of elements is chosen which e.g. brings down the amount of constraints for a WTB cross section from 500 (n_e cross section FE's, each with its own stress vector) to 80 for each patch of elements. Using a maximum constraint approach, the most violated constraint value i.e. highest FI of a patch is considered. This introduces some difficulties since the constraint function will most likely not be continuous since the maximum may jump between elements as a new iteration is performed. However, with the elements patched together in subparts that share materials, material orientations, and placement in the cross section, the stresses will not deviate greatly elements between. To this measure, the Tsai-Wu failure criteria and its like is preferred over Max Strain and Max Stress failure criteria, since Tsai-Wu collects the stresses to a single value while the others presents one for each directional stress and shear stress.

In the following sections, the failure criteria considered, implemented and used in this study is presented.

Max Stress

The Max Stress constraints are defined as the ratio between the stress in the material and the known stress limits for the material. The limits are defined with lab tests, measuring the composite material properties or with simplified methods such as the Rule of Mixture[72]. The sign of the stress is included such that a compression limit value is used if the stress evaluated at the element is negative i.e. experiencing compression (limits $\bar{\sigma}^t_{ii}$ / $\bar{\sigma}^c_{ii}$ for tensile and compression respectively). The shear stress, σ_{ij}, is treated as sign independent and the absolute value is used. Eq. (3.9) presents the Max Stress definition and eq. (3.10) presents the FI evaluation from the Max Stress constraint fractions. When the FI takes on a value above 1, material failure is predicted to occur.

$$\begin{array}{rcl} \bar{\sigma}^c_{ii} < & \sigma_{ii} & < \bar{\sigma}^t_{ii} \\ & |\sigma_{ij}| & < |\bar{\sigma}_{ij}| \end{array} \tag{3.9}$$

$$FI_{MaxStress} = \begin{cases} \sigma_{ii}/\bar{\sigma}^t_{ii}, & \text{if} \quad \sigma_{ii} \geq 0, \quad i = 1,2,3 \\ \sigma_{ii}/\bar{\sigma}^c_{ii}, & \text{if} \quad \sigma_{ii} < 0, \quad i = 1,2,3 \\ |\sigma_{ij}|/|\bar{\sigma}_{ij}|, & \qquad\qquad\quad i,j = 1,2,3 \end{cases} \tag{3.10}$$

Three FI's are calculated for each of the general directions components as the fraction between stress value and the proper material limit selected from the sign of the stress. Another three FI are calculated for each of the shear components, summing to a total of six FI and thus six stress constraints for the finite element.

Max Strain

Equally simple and useful are the Max Strain criteria. Here, instead of the material stresses in an element, the material strains are used. Eq. (3.11) presents the relation and eq. (3.12) presents the failure criteria as the ratio between the material strains and the material known limits. As with the Max Stress criteria, the Max Strain is relative to the sign of the strain.

$$\begin{array}{rcl} \bar{\varepsilon}^c_{ii} < & \varepsilon_{ii} & < \bar{\varepsilon}^t_{ii} \\ & |\varepsilon_{ij}| & < |\bar{\varepsilon}_{ij}| \end{array} \tag{3.11}$$

$$FI_{MaxStrain} = \begin{cases} \varepsilon_{ii}/\bar{\varepsilon}^t_{ii}, & \text{if} \quad \varepsilon_{ii} > 0, \quad i = 1,2,3 \\ \varepsilon_{ii}/\bar{\varepsilon}^c_{ii}, & \text{if} \quad \varepsilon_{ii} < 0, \quad i = 1,2,3 \\ |\varepsilon_{ij}|/|\bar{\varepsilon}_{ij}|, & \quad\quad\quad\quad\quad\quad i,j = 1,2,3 \end{cases} \tag{3.12}$$

Both Max Stress and Max Strain failure criteria are preexisting in BECAS. Common for the Max Stress and Max Strain criteria is that the components are evaluated independently, meaning that the loads in different direction neither interact or contribute to each other[72]. This is a main insufficiency of the criterias as the combined loading effects (e.g. how one shear loading can affect the strength in principle direction) are omitted in the models. Most popular efforts to account for these are the model known as Tsai-Hill and Tsai-Wu failure criteria. They take their offset in empirical observations and thus contain empirical determined constants that must be set prior to calculation. Although generally considered as more accurate and physical, the methods do not predict failure modes (type of failure e.g. delamination or fiber-pull-out), only whether failure occurs based on material stresses.

In BECAS, Tsai-Wu and Hashin failure criteria are preexisting, where the first of the two are considered in this study. The Hashin failure criteria was originally also considered and implemented with validated gradients against a central finite difference check, however, to limit the already considerable amount of the thesis work on failure constraints, it was deemed that the Tsai-Wu failure criterion is sufficient and represents a more sophisticated and inclusive method than the simple Max Strain and Stress. The theory and sensitivity results of the Hashin failure criterion can be seen in the appendix page 80).

Tsai-Wu

The Tsai-Wu failure criterion is defined below as implemented in BECAS. For a reference one can look to Tsai and Hahn's *Introduction to Composite Materials*[66] or Kassapoglou's *Design and Analysis of Composite Structures With Application to Aerospace Structures*[36], although not represented in a similar fashion.

$$FI_{Tsai-Wu} = A + B \tag{3.13}$$

where

$$A = -\frac{\sigma^2_{11}}{\bar{\sigma}^t_{11}\bar{\sigma}^c_{11}} - \frac{\sigma^2_{22}}{\bar{\sigma}^t_{22}\bar{\sigma}^c_{22}} - \frac{\sigma^2_{33}}{\bar{\sigma}^t_{33}\bar{\sigma}^c_{33}} + \frac{\sigma^2_{12}}{\bar{\sigma}^2_{12}} + \frac{\sigma^2_{23}}{\bar{\sigma}^2_{23}} + \frac{\sigma^2_{13}}{\bar{\sigma}^2_{13}} + ... \tag{3.14}$$

$$\frac{C_{12}\sigma_{11}\sigma_{22}}{\sqrt{\bar{\sigma}^t_{11}\bar{\sigma}^c_{11}\bar{\sigma}^t_{22}\bar{\sigma}^c_{22}}} + \frac{C_{23}\sigma_{22}\sigma_{33}}{\sqrt{\bar{\sigma}^t_{22}\bar{\sigma}^c_{22}\bar{\sigma}^t_{33}\bar{\sigma}^c_{33}}} + \frac{C_{13}\sigma_{11}\sigma_{33}}{\sqrt{\bar{\sigma}^t_{11}\bar{\sigma}^c_{11}\bar{\sigma}^t_{33}\bar{\sigma}^c_{33}}} \tag{3.15}$$

$$B = \left(\frac{1}{\bar{\sigma}_{11}^t} + \frac{1}{\bar{\sigma}_{11}^c}\right)\sigma_{11} + \left(\frac{1}{\bar{\sigma}_{22}^t} + \frac{1}{\bar{\sigma}_{22}^c}\right)\sigma_{22} + \left(\frac{1}{\bar{\sigma}_{33}^t} + \frac{1}{\bar{\sigma}_{33}^c}\right)\sigma_{33} \tag{3.16}$$

The constants C_{ij} are coupling constants and takes values in the range $C_{ij} \in [-2...0]$ with a recommended value of -1 for each, which is used in this study. As observed in the equations above, the loading is now coupled.

3.3 Sensitivities

This section presents the sensitivities of the considered objective and constraint functions which must be provided to the gradient based optimization algorithms. First, a small discussion on the choice of sensitivity calculation method.

When sensitivities of displacements of a FE system is needed, two methods are generally considered: the direct analytical and the adjoint method. The first mentioned is preferred when the number of constraints is larger than the number of design variables and uses the chain-rule for the equilibrium equation $\mathbf{K}_g\mathbf{u} = \mathbf{p}$ to obtain the displacement derivative. This means the FE system of equilibrium equations are solved for each design variable x_i which can be costly if a large system exists i.e. large amount of elements. The adjoint method is preferred when the number of design variables are larger than number of constraints. The derivative of the displacements are not calculated explicitly but a zero function is added in the calculation containing an arbitrary, fixed real vector[4]. Definition of this vector results in the elimination of the state vector derivative i.e. the displacement gradient which results in one backsubstitution per response (objective and constraints) whereas the direct method needed one backsubstitution per design variable.

In this study, the adjoint method was initially not considered used since the FE beam formulation presents a manageable system in that not being significantly large (approximately 20 beam elements). Were this a topology optimization of the cross section, the adjoint method would have be considered since each 2D cross section FE would impose a design variable. The stress constraints, presented earlier, exhibits a FI for each patch of elements which quickly surpass the number of design variables. This is since FI's for all the patches in the cross section are considered in the optimization whereas only a selected batch of patches exhibit design variables e.g. caps element patches and/or shell elements patches. This means the number of constraints are higher than number of design variables when failure criteria constraints are considered.

3.3.1 Compliance

The gradient of the compliance is calculated here. Assuming independent static loads and that the cross section stiffness matrix is symmetric, the following is obtained by differentiating eq. (3.2):

$$\frac{\partial C}{\partial x_i} = \mathbf{p}^T\frac{\partial \mathbf{u}}{\partial x_i} = \mathbf{u}^T\mathbf{K}_g\frac{\partial \mathbf{u}}{\partial x_i} \tag{3.17}$$

Above the relation $\mathbf{u}^T\mathbf{K}_g = \mathbf{p}^T$ from eq. (2.12) is used. This is used again to determine the displacement field gradient $\partial\mathbf{u}/\partial x_i$ using the product rule:

$$\frac{\partial \mathbf{K}_g}{\partial x_i}\mathbf{u} + \mathbf{K}_g\frac{\partial \mathbf{u}}{\partial x_i} = \mathbf{0} \leftrightarrow \frac{\partial \mathbf{u}}{\partial x_i} = -\mathbf{K}_g^{-1}\frac{\partial \mathbf{K}_g}{\partial x_i}\mathbf{u} \tag{3.18}$$

Inserting above in eq. (3.17) yields the final expression for the gradient of the compliance matrix

$$\frac{\partial C}{\partial x_i} = -\mathbf{u}^T \frac{\partial \mathbf{K}_g}{\partial x_i}\mathbf{u} \tag{3.19}$$

3.3.2 Cross section stiffness matrix

The analytic term for the cross section stiffness matrix gradient, $\partial \mathbf{K}_s/\partial x_i$, w.r.t. the design variables x_i is determined in this section. It involves first determining the derivative of the cross section solution followed by the compliance matrix gradient, $\partial \mathbf{F}_s/\partial x_i$. Restating the compliance eq. (2.40) here for convenience:

$$\mathbf{F}_s = \mathbf{W}^T \mathbf{G} \mathbf{W} \tag{3.20}$$

Gradient of $\mathbf{F}_s$ is then obtained by using the chain rule:

$$\frac{\partial \mathbf{F}_s}{\partial x_i} = \frac{\partial \mathbf{W}^T}{\partial x_i}\mathbf{G}\mathbf{W} + \mathbf{W}^T \frac{\partial \mathbf{G}}{\partial x_i}\mathbf{W} + \mathbf{W}^T \mathbf{G} \frac{\partial \mathbf{W}}{\partial x_i} \tag{3.21}$$

where

$$\frac{\partial \mathbf{W}}{\partial x_i} = \frac{\partial \mathbf{K}^{-1}}{\partial x_i}\mathbf{F} \tag{3.22}$$

from eq. (2.30). This can also be stated as (see appendix page 79 for illustration of this little mathematical alternation):

$$\frac{\partial \mathbf{W}}{\partial x_i} = -\mathbf{K}^{-1}\frac{\partial \mathbf{K}}{\partial x_i}\mathbf{K}^{-1}\mathbf{F} = -\mathbf{K}^{-1}\frac{\partial \mathbf{K}}{\partial x_i}\mathbf{W} \tag{3.23}$$

Inserting this in eq. (3.21) gives

$$\frac{\partial \mathbf{F}_s}{\partial x_i} = -\mathbf{W}^T \frac{\partial \mathbf{K}^T}{\partial x_i}\mathbf{K}^{-T}\mathbf{G}\mathbf{W} + \mathbf{W}^T \frac{\partial \mathbf{G}}{\partial x_i}\mathbf{W} - \mathbf{W}^T \mathbf{G}\mathbf{K}^{-1}\frac{\partial \mathbf{K}}{\partial x_i}\mathbf{W} \tag{3.24}$$

Defining $\mathbf{V} = \mathbf{K}^{-T}\mathbf{G}\mathbf{W}$ and assuming $\mathbf{G}^T = \mathbf{G}$ the above results in

$$\frac{\partial \mathbf{F}_s}{\partial x_i} = -\mathbf{W}^T \frac{\partial \mathbf{K}^T}{\partial x_i}\mathbf{V} + \mathbf{W}^T \frac{\partial \mathbf{G}}{\partial x_i}\mathbf{W} - \mathbf{V}^T \frac{\partial \mathbf{K}}{\partial x_i}\mathbf{W} \tag{3.25}$$

which in the end can be used for the cross section stiffness gradient:

$$\frac{\partial \mathbf{K}_s}{\partial x_i} = \frac{\partial \mathbf{F}_s^{-1}}{\partial x_i} \tag{3.26}$$

$\mathbf{G}$,$\mathbf{K}$ and $\mathbf{W}$ all dependent on the design variable through the rotated material constitutive matrix, $\mathbf{Q}_e$, as observed in section 2.3.3 by eq. (2.26).

3.3.3 Tip deflection and twist gradient

From the global equilibrium equation eq. (2.12), restated below for convenience, the gradient of the WTB tip deflection and twist can be determined.

$$\mathbf{K}_g(\boldsymbol{x})\mathbf{u}(\boldsymbol{x}) = \mathbf{p} \tag{3.27}$$

calculating $\partial \mathbf{u}(\boldsymbol{x})/\partial \boldsymbol{x}$ and still assuming loads to be independent:

$$\frac{\partial \mathbf{K}_g(\boldsymbol{x})}{\partial x_i}\mathbf{u}(\boldsymbol{x}) + \mathbf{K}_g(\boldsymbol{x})\frac{\partial \mathbf{u}(\boldsymbol{x})}{\partial x_i} = \frac{\partial \mathbf{p}}{\partial x_j} = \mathbf{0} \tag{3.28}$$

$$\mathbf{K}_g(\boldsymbol{x})\frac{\partial \mathbf{u}(\boldsymbol{x})}{\partial x_i} = -\frac{\partial \mathbf{K}_g(\boldsymbol{x})}{\partial x_i}\mathbf{u}(\boldsymbol{x}) \tag{3.29}$$

$$\frac{\partial \mathbf{u}(\boldsymbol{x})}{\partial x_i} = -\mathbf{K}_g(\boldsymbol{x})^{-1}\left(\frac{\partial \mathbf{K}_g(\boldsymbol{x})}{\partial x_i}\mathbf{u}(\boldsymbol{x})\right) \tag{3.30}$$

The above is known as the pseudo-load due to its similarity to the equilibrium equations. The gradient of the global stiffness matrix is needed. The global stiffness matrix is defined in eq. (2.10) but is restated here for convenience:

$$\mathbf{K}_g = \sum_{b=1}^{n_b}\mathbf{K}_b = \sum_{b=1}^{n_b}\int_0^{L_b}\mathbf{B}_b^T\mathbf{K}_s\mathbf{B}_b \mathrm{d}z \tag{3.31}$$

The gradients thus become:

$$\frac{\partial \mathbf{K}_g}{\partial x_i} = \sum_{b=1}^{n_b}\frac{\partial \mathbf{K}_b}{\partial x_i} = \sum_{b=1}^{n_b}\int_0^{L_b}\mathbf{B}_b^T\frac{\partial \mathbf{K}_s}{\partial x_i}\mathbf{B}_b \mathrm{d}z \tag{3.32}$$

with the gradient of the cross section stiffness matrix provided in eq. (3.26).

3.3.4 Eigenfrequencies gradients

The method to obtain the derivatives of the eigenfrequencies follows that proposed by Seyranian et al. [56] which has seen its use in e.g. [6] and in [13].
The structural eigenvalue problem can be stated as:

$$\mathbf{K}_g\mathbf{v}_j = \lambda_j\mathbf{M}_g\mathbf{v}_j, \qquad j = 1, ..., n_{dof} \tag{3.33}$$

where $\lambda_j = \omega_j^2$ and $\mathbf{M}_g$-orthonormalization is assumed: $\mathbf{v}_j^T\mathbf{M}_g\mathbf{v}_k = \delta_{jk}$ such that:

$$\mathbf{v}_j^T\mathbf{M}_g\mathbf{v}_k = \begin{cases} 1 & \text{if } j = k \\ 0 & \text{if } j \neq k \end{cases} \qquad j, k = 1, ..., n_{dof} \tag{3.34}$$

and eigenvectors a $\mathbf{K}_g$-orthogonal; $\mathbf{v}_j^T\mathbf{K}_g\mathbf{v}_k = \lambda_j\delta_{jk}$ such that:

$$\mathbf{v}_j^T\mathbf{K}_g\mathbf{v}_k = \begin{cases} \lambda_j & \text{if } j = k \\ 0 & \text{if } j \neq k \end{cases} \qquad j, k = 1, ..., n_{dof} \tag{3.35}$$

the gradient (single case) can be obtained by differentiation of eq. (3.33):

$$\frac{\partial \mathbf{K}_g}{\partial x_i}\mathbf{v}_j + (\mathbf{K} - \lambda_j\mathbf{M}_g)\frac{\partial \mathbf{v}_j}{\partial x_i} = \frac{\partial \lambda_j}{\partial x_i}\mathbf{M}_g\mathbf{v}_j + \lambda_j\frac{\partial \mathbf{M}_g}{\partial x_i}\mathbf{v}_j \tag{3.36}$$

$$\frac{\partial \lambda_j}{\partial x_i} = \mathbf{v}_j^T\left(\frac{\partial \mathbf{K}_g}{\partial x_i} - \lambda_j\frac{\partial \mathbf{M}_g}{\partial x_i}\right)\mathbf{v}_j \tag{3.37}$$

3.3.5 Failure criteria gradients

The three considered failure criteria, Max Strain, Max Stress and Tsai-Wu, either needs the material strains or stresses to evaluate the FI. The material stress in an element, $\boldsymbol{\sigma}_m$, is given by eq. (3.38) and the derivative w.r.t. design variable (fiber orientation) is presented in eq. (3.39).

$$\boldsymbol{\sigma}_m = \mathbf{Q}_m \boldsymbol{\varepsilon}_m \tag{3.38}$$

$$\frac{\partial \boldsymbol{\sigma}_m}{\partial x_i} = \mathbf{Q}_m \frac{\partial \boldsymbol{\varepsilon}_m}{\partial x_i} \tag{3.39}$$

The strain in the material coordinate system, $\boldsymbol{\varepsilon}_m$, is the global strain, $\boldsymbol{\varepsilon}_g$, rotated with standard rotation matrix, $\mathbf{T}$, see if necessary appendix page 75.

$$\boldsymbol{\varepsilon}_m = \mathbf{T}\boldsymbol{\varepsilon}_g\mathbf{T}^T \tag{3.40}$$

The gradient of the material strain in an element is:

$$\frac{\partial (\boldsymbol{\varepsilon}_m)_e}{\partial x_i} = \begin{cases} \dfrac{\partial \mathbf{T}}{\partial x_i}(\boldsymbol{\varepsilon}_g)_e\mathbf{T}^T + \mathbf{T}\dfrac{\partial (\boldsymbol{\varepsilon}_g)_e}{\partial x_i}\mathbf{T}^T + \mathbf{T}(\boldsymbol{\varepsilon}_g)_e\dfrac{\partial \mathbf{T}^T}{\partial x_i} & \text{, if} \quad e \in p_i \\ \mathbf{T}\dfrac{\partial (\boldsymbol{\varepsilon}_g)_e}{\partial x_i}\mathbf{T}^T & \text{, otherwise} \end{cases} \tag{3.41}$$

meaning that if the element does not belong to a patch associated with the specific design variable x_i, the partial derivative of the transformation matrix $\mathbf{T}$ is zero. The interpretation of this is that a change in fiber angle, or stiffness, for one ply/patch of elements does not affect the local strains in other plies/patches. The global strain for element e is calculated with the cross section warping displacement solution (and reusing cross section gradient arrays found in section **??**:

$$(\boldsymbol{\varepsilon}_g)_e = \mathbf{S}\mathbf{Z}_e\boldsymbol{\varphi} + \mathbf{B}_e\mathbf{N}_e\mathbf{u} + \mathbf{S}\mathbf{N}_e\frac{\partial \mathbf{u}}{\partial z} \tag{3.42}$$

where $\boldsymbol{\varphi} = \mathbf{Y}\boldsymbol{\theta}$, $\mathbf{u} = \mathbf{X}\boldsymbol{\theta}$ and $\partial\mathbf{u}/\partial z = \partial\mathbf{X}/\partial z\boldsymbol{\theta}$. The gradient is calculated element-wise, and below the subscript e is dropped for the strain for abbreviation.

$$\boldsymbol{\varepsilon}_g = \mathbf{S}\mathbf{Z}_e\mathbf{Y}\boldsymbol{\theta} + (\mathbf{B}_e\mathbf{N}_e\mathbf{X}\boldsymbol{\theta}) + \left(\mathbf{S}\mathbf{N}_e\frac{\partial \mathbf{X}}{\partial z}\boldsymbol{\theta}\right) \tag{3.43}$$

of which the gradient is found with the product rule:

$$\frac{\partial \boldsymbol{\varepsilon}_g}{\partial x_i} = \mathbf{S}\mathbf{Z}_e\left(\frac{\partial \mathbf{Y}}{\partial x_i}\boldsymbol{\theta} + \mathbf{Y}\frac{\partial \boldsymbol{\theta}}{\partial x_i}\right) + \mathbf{B}\mathbf{N}_e\left(\frac{\partial \mathbf{X}}{\partial x_i}\boldsymbol{\theta} + \mathbf{X}\frac{\partial \boldsymbol{\theta}}{\partial x_i}\right) + \mathbf{S}\mathbf{N}_e\left(\frac{\partial}{\partial x_i}\frac{\partial \mathbf{X}}{\partial z}\boldsymbol{\theta} + \frac{\partial \mathbf{X}}{\partial z}\frac{\partial \boldsymbol{\theta}}{\partial x_i}\right) \tag{3.44}$$

The derivative of the warping solution to a unit load, $\mathbf{X}, \mathbf{Y}$, and $\partial\mathbf{X}/\partial z$ w.r.t. the design variables, x_i, is obtained in a similar manor as for the cross section stiffness matrix gradients. Restating eq. (2.30), differentiating w.r.t. to x_i and isolating the warping solution gradient:

$$\mathbf{K}\mathbf{W} = \mathbf{F} \rightarrow \frac{\partial \mathbf{W}}{\partial x_i} = \frac{\partial \mathbf{K}^{-1}}{\partial x_i}\mathbf{F} + \mathbf{K}^{-1}\frac{\partial \mathbf{F}}{\partial x_i} \tag{3.45}$$

Here $\partial\mathbf{F}/\partial x_i = 0$, $\mathbf{K}^{-1}\mathbf{F} = \mathbf{W}$ and by using chain rule the above can be reformulated to:

$$\frac{\partial \mathbf{W}}{\partial x_i} = -\mathbf{K}\frac{\partial \mathbf{K}}{\partial x_i}\mathbf{W} \tag{3.46}$$

which is very convenient since above is all known values from the displacement gradient calculation. The cross section forces and moments will change with varying fiber angles:

$$\boldsymbol{\theta} = \mathbf{K}_b \mathbf{u}_{edof} \rightarrow \frac{\partial \boldsymbol{\theta}}{\partial x_i} = \frac{\partial \mathbf{K}_b}{\partial x_i}\mathbf{u}_{edof} + \mathbf{K}_b \frac{\partial \mathbf{u}_{edof}}{\partial x_i} \tag{3.47}$$

Above, $\mathbf{K}_b$ is the beam element stiffness matrix of beam b and $\mathbf{u}_{edof}$ is the nodal displacements of beam element b. Everything for evaluating global strains (3.44), local strains (3.41), and local stresses (3.39) are now known.

Max Stress gradient

The stress gradient in the material coordinate system is obtained by eq. (3.39). Using the value obtained by this expression, the Max Stress FI derivative is easily found as:

$$\frac{\partial FI_{MaxStress}}{\partial x_i} = \begin{cases} \dfrac{\partial \sigma_{kk}}{\partial x_i}\dfrac{1}{\bar{\sigma}^t_{kk}}, & \text{if} \quad \sigma_{kk} > 0, \quad k = 1,2,3 \\ \dfrac{\partial \sigma_{kk}}{\partial x_i}\dfrac{1}{\bar{\sigma}^c_{kk}}, & \text{if} \quad \sigma_{kk} < 0, \quad k = 1,2,3 \\ \left|\dfrac{\partial \sigma_{kl}}{\partial x_i}\right| \cdot \left|\dfrac{1}{\bar{\sigma}_{kl}}\right| & k,l = 1,2,3 \end{cases} \tag{3.48}$$

Max Strain gradient

The strain gradient in the material coordinate system is found using eq. (3.41). The Max Strain FI gradient is then found as:

$$\frac{\partial FI_{MaxStrain}}{\partial x_i} = \begin{cases} \dfrac{\partial \varepsilon_{kk}}{\partial x_i}\dfrac{1}{\bar{\varepsilon}^t_{kk}}, & \text{if} \quad \varepsilon_{kk} > 0, \quad k = 1,2,3 \\ \dfrac{\partial \varepsilon_{kk}}{\partial x_i}\dfrac{1}{\bar{\varepsilon}^c_{kk}}, & \text{if} \quad \varepsilon_{kk} < 0, \quad k = 1,2,3 \\ \left|\dfrac{\partial \varepsilon_{kl}}{\partial x_i}\right| \cdot \left|\dfrac{1}{\bar{\varepsilon}_{kl}}\right| & k,l = 1,2,3 \end{cases} \tag{3.49}$$

The gradients of the Max Strain and Max Stress FI's are convenient since no modifications are needed in the BECAS implementation. Instead of providing the material strain and stresses, the gradient values are instead used as inputs. It is important to notice the dependence on the principal stress or strain signs since this determines whether the material experiences compression or tensile loads. It is thus not the sign of the gradient which should be considered when calculating the gradients of the above.

Tsai-Wu gradient

Using the product rule, the Tsai-Wu FI gradient value can be calculated as:

$$\frac{\partial FI_{Tsai-Wu}}{\partial x_i} = \frac{\partial A}{\partial x_i} + \frac{\partial B}{\partial x_i} \tag{3.50}$$

where (using $\partial\sigma/\partial x_i = \sigma'$ for abbreviation):

$$\frac{\partial A}{\partial x_i} = -\frac{2\sigma_{11}\sigma'_{11}}{\bar{\sigma}^t_{11}\bar{\sigma}^c_{11}} - \frac{2\sigma_{22}\sigma'_{22}}{\bar{\sigma}^t_{22}\bar{\sigma}^c_{22}} - \frac{2\sigma_{33}\sigma'_{33}}{\bar{\sigma}^t_{33}\bar{\sigma}^c_{33}} + \frac{2\sigma_{12}\sigma'_{12}}{\bar{\sigma}^2_{12}} + \frac{2\sigma_{23}\sigma'_{23}}{\bar{\sigma}^2_{23}} + \frac{2\sigma_{13}\sigma'_{13}}{\bar{\sigma}^2_{13}} + C + D + E \quad (3.51)$$

with

$$C = \frac{C_{12}\sigma'_{11}\sigma_{22}}{\sqrt{\bar{\sigma}^t_{11}\bar{\sigma}^c_{11}\bar{\sigma}^t_{22}\bar{\sigma}^c_{22}}} + \frac{C_{12}\sigma_{11}\sigma'_{22}}{\sqrt{\bar{\sigma}^t_{11}\bar{\sigma}^c_{11}\bar{\sigma}^t_{22}\bar{\sigma}^c_{22}}}$$

$$D = \frac{C_{23}\sigma'_{22}\sigma_{33}}{\sqrt{\bar{\sigma}^t_{22}\bar{\sigma}^c_{22}\bar{\sigma}^t_{33}\bar{\sigma}^c_{33}}} + \frac{C_{23}\sigma_{22}\sigma'_{33}}{\sqrt{\bar{\sigma}^t_{22}\bar{\sigma}^c_{22}\bar{\sigma}^t_{33}\bar{\sigma}^c_{33}}}$$

$$E = \frac{C_{13}\sigma'_{11}\sigma_{33}}{\sqrt{\bar{\sigma}^t_{11}\bar{\sigma}^c_{11}\bar{\sigma}^t_{33}\bar{\sigma}^c_{33}}} + \frac{C_{13}\sigma_{11}\sigma'_{33}}{\sqrt{\bar{\sigma}^t_{11}\bar{\sigma}^c_{11}\bar{\sigma}^t_{33}\bar{\sigma}^c_{33}}}$$

and

$$\frac{\partial B}{\partial x_i} = \left(\frac{1}{\bar{\sigma}^t_{11}} + \frac{1}{\bar{\sigma}^c_{11}}\right)\frac{\partial \sigma_{11}}{\partial x_i} + \left(\frac{1}{\bar{\sigma}^t_{22}} + \frac{1}{\bar{\sigma}^c_{22}}\right)\frac{\partial \sigma_{22}}{\partial x_i} + \left(\frac{1}{\bar{\sigma}^t_{33}} + \frac{1}{\bar{\sigma}^c_{33}}\right)\frac{\partial \sigma_{33}}{\partial x_i} \quad (3.52)$$

3.3.6 BTC factor

The BTC factor, as defined in eq. (3.6) and restated below for convenience, has also been considered as both objective and constraint. To this matter, the gradient is also determined. The parameter is defined as the fraction between the K_{46} element in cross section and the square root of the product of K_{44} and K_{66}:

$$\alpha_n(\mathbf{x}_{dv}) = \frac{K^{(n)}_{46}(\mathbf{x}_{dv})}{\sqrt{K^{(n)}_{44}(\mathbf{x}_{dv})K^{(n)}_{66}(\mathbf{x}_{dv})}}, \qquad n = 1, ..., N \quad (3.53)$$

where all stiffness terms are dependent on the fiber angle. The gradient of the BTC factor is then (leaving out $(\mathbf{x}_{dv})$ and (n) for abbreviation):

$$\frac{\partial \alpha_n}{\partial x_i} = \begin{cases} \dfrac{\dfrac{\partial K_{46}}{\partial x_i}}{\sqrt{K_{44}K_{66}}} - \dfrac{1}{2}\dfrac{K_{46}\left(\dfrac{\partial K_{44}}{\partial x_i}K_{66} + K_{44}\dfrac{\partial K_{66}}{\partial x_i}\right)}{(K_{66}K_{44})^{3/2}} & \text{if} \quad x_i \in \mathbf{x}_{dv} \\ 0 & \text{if} \quad x_i \notin \mathbf{x}_{dv} \end{cases} \quad (3.54)$$

The gradient values are then summed with the same weightings as defined in eq. (3.7):

$$\frac{\partial \alpha}{\partial x_i} = \sum_{n=1}^{N} w_n \frac{\partial \alpha_n}{\partial x_i} \quad (3.55)$$

3.4 Validation

The analytic sensitivities are validated against self-build numeric finite difference gradients checks. Both IPOPT and *fmincon* are accompanied with derivative checkers, however, these have, from experience, showed to be less reliable. The error values presented in this section, rely on the self-build finite difference checks. Prior to the results is a small introduction to the

theory behind the sensitivity validation.

A finite difference gradient is simply an easy way to estimate the derivative or slope of a function. The evaluation of a function, $f(\mathbf{x})$, with a small perturbation step forwards or backwards, $\pm h$, added to the independent variable, $\mathbf{x}$, allows for the approximation of the gradient. Most common is the forward finite difference and central finite difference methods where the latter is presented in eq. (3.56).

$$\frac{\partial f(\mathbf{x})}{\partial x_i}_{CFD} \approx \frac{f(\mathbf{x} + h \cdot \mathbf{e}_i) - f(\mathbf{x} - h \cdot \mathbf{e}_i)}{2h} \tag{3.56}$$

The vector $\mathbf{e}$ is the size of $\mathbf{x}$ with all zero except for a single element at the index i. The method requires 2 function evaluations and is therefor more expensive than the forward finite difference method that only has a single perturbation direction but also exhibits less accuracy compared to the central finite difference. Derivation, discussions and more of finite-difference derivative approximations can be found in for example the book *Numerical Optimization* by J. Nocedal[49].

Error of gradients, vector

For a vector of gradient values, the infinity norm is used to determine a combined error of the vector errors, that is for example the difference between analytic obtained displacement and rotation values $\partial\mathbf{u}/\partial z$, and the finite difference ones:

$$\epsilon_u = \max_i \left(\left|\left| \frac{\partial \mathbf{u}}{\partial x_i} - \frac{\partial \mathbf{u}}{\partial x_i}_{CFD} \right|\right|_{Inf} \right), \quad \forall i = 1, ..., n_{dv} \tag{3.57}$$

To elaborate: the analytic gradients of each element in $\mathbf{u}$ is compared with a numerical gradient by subtracting one from the other. That leaves a column vector of errors pr. design variable $i = 1, ..., n_{dv}$. The maximum error is found as the maximum infinity norm of each column vector. Doing so can reveal the design variable providing the largest error which will be used to investigate the truncation and conditional error since the numeric gradient is highly sensitive to perturbation step size.

Error of gradients, array

For an array of gradient values, the error is found as the Frobenius norm of the difference between the two matrices. This is the case for e.g. the cross section stiffness matrix.

$$\epsilon_{\mathbf{K}_s} = \max_i \left(\left|\left| \frac{\partial \mathbf{K}_s}{\partial x_i} - \frac{\partial \mathbf{K}_s}{\partial x_i} \right|\right|_{Fro} \right), \quad \forall i = 1, ..., n_{dv} \tag{3.58}$$

3.4.1 Gradient errors

All gradient values have been compared to a central finite difference check and the results are summarized in this section by presenting the errors calculated with the above mentioned methods and variable perturbation steps in figures 3.1a and 3.1b. The test case is the sandwich beam presented in chapter 4, with material properties provided in MPa, density in 1e-6 kg/m^3 and the load equally scaled to MN. This is done due to the norms' sensitivity to size of value. If the elements in a vector or array are large e.g. 1e6, the calculated gradient errors would also be larger. From the figures, it is observed that, depending on the perturbation step, all errors can present values below 1e-6 which is deemed sufficient. Eigenvalues present the highest minimum error at h-step=5e-3 with an error of 4.3e-7 (rad/s)^2.

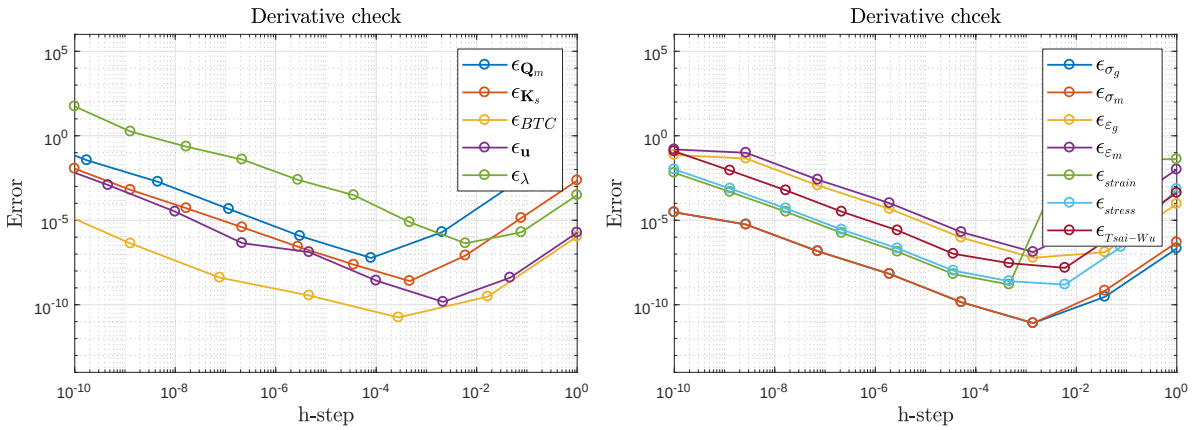

Figure 3.1: ***a****: Errors for material constitutive matrix (*$\mathbf{Q}_m$*), cross section stiffness matrix (*$\mathbf{K}_s$*), BTC factor (**BTC**), beam FE displacement field for displacement and twist (*$\mathbf{u}$*), eigenfrequencies (*λ*).* ***b****: Errors for global stress (*$\boldsymbol{\sigma}_g$*), material stress (*$\boldsymbol{\sigma}_m$*), global strain (*$\boldsymbol{\varepsilon}_g$*), material strain (*$\boldsymbol{\varepsilon}_m$*), failure criteria Max Strain (**strain**), failure criteria Max Stress (**stress**), failure criteria Tsai-Wu (**Tsai-Wu**).*

3.5 Optimization of composites in general

Optimization of composite structures is a challenging problem due to the non-convexity and multi-material composition. Structural optimization usually considers minimization of mass or compliance with the aim of obtaining a low weight and stiff structure and can be generalized into three subcategories: shape-, sizing/material and topology optimization where this study is closest to sizing/material. Optimizing materials in a structure is complicated due to the discrete design variables and to utilize a gradient based optimization algorithm, some form of continuation is needed. Discrete design variables stems from the composite industry, where fiber mats are produced in only off-the-shell angles such as $[0°, \pm 45°, 0°/90°]$. Obtaining angles different than the mentioned is possible, however, the cost of the production limits the selection. Recent developments has led to discrete material optimization (DMO) methods that are applicable to use for optimization of composite structures and has been demonstrated to be capable of composite optimization problems using gradient based numerical optimization algorithms. The DMO scheme developed by Stegmann and Lund[61] could be implemented to give a more realistic design of the optimum bend-twist coupled WTB, however, this is left for future work. Instead, for this study, the fiber angles/design variables are modeled as continuous which was the common method prior to DMO, see e.g. Pedersen[52][53], Stegmann and Lund[61], and Blasques and Stolpe[7].

3.6 Discussion on solvers

This section presents the discussion on choice of optimization algorithm. First it must be recognized, that the full scale blade optimization problem to be solved is nonlinear, constrained, and large-scale i.e. a large amount of design variables and constraints and likely many local minimums. This means that the below considered solvers will likely converge to local minimum.
A right at hand algorithm is the Sequential Quadratic Programming (SQP) which is implemented in the MATLAB function *fmincon*. SQP approximates the problem to a convex, nested problem by a second order Taylor expansion at a given design point $\mathbf{x}_k$. The solution to the nested problem is the new design point and the problem is iteratively solved this way until

no reduction in objective is found in any feasible directions, determined by constraint boundaries and gradient information. The method is known for its capabilities to handle significant nonlinearities[49] and is thus a desirable choice for this study.
The other algorithm used in this study is the Interior Point OPTimization (IPOPT, pronounced "eye-pee-opt")[69]. It utilizes an interior-point line-search filter method where the objective and constraint functions can be linear/nonlinear and convex/non-convex. The optimization problem to be solved contains inequality constraints which means that IPOPT will utilize slack variables to turn them into equality constraints before solving the problem with a barrier method. Slack variables result in a large increase of variables and all constraints are considered all the time, however, its ability to handle large-scale problems might prove sucessfull where SQP is not. As with SQP, IPOPT is likely unable to escape local minima since it searches only locally in the design domain. An alternative to SQP and IPOPT is genetic algorithms which both can handle nonlinear problems and possibly escape local minimums. However, this comes with a considerable computational cost due to the many function evaluations needed. The IPOPT algorithm can be downloaded with no charge together with a MATLAB toolbox including dozens of other optimization algorithms from inverseproblem.co.nz [33]. The motivation for using IPOPT is the large amount of design variable that can occur of proper patching of elements are not provided or that patching is not realized in the framework. Then the number of finite elements in the cross section mesh drastically increase the problem size. Furthermore, it will be interesting to observe the performance of the two algorithms.
Both algorithms may start from an unfeasible point, however, for any non-convex problem and gradient based numerical algorithm, the solution depends on the point of departure.

3.7 Framework and implementation

The framework used for the optimization is build up using an input script, defining and building the structures needed for the optimization and the structures needed to run BECAS for the evaluation of above considered objective and constraint functions. The calculation of cross section stiffness matrices, the assembly of the FE beam model and the evaluation of response, eigenfrequencies, and stresses are all done by BECAS/FRANS as well as a majority of the pre- and post-processing functions. Template files, allowing for the analysis of the DTU10MW reference WTB is distributed with BECAS, and the pre-processing module, using shellexpander.py, made for an easy way to import the WTB into BECAS as well as changing initial layups. Without this, GMSH would have been the alternative to descritize the cross section. The structure of the created framework takes its inspiration from the framework presented in the DTU course *46415 - Structural analysis and design optimization of wind turbine blades*, which presented an organized and simplified optimization framework. The present contributions to the structure is the sensitivity calculations, the sensitivity validation, and extending the pre- and post-processing modules to accommodate blade optimization in a efficient way. A lot of work has been put into proper bookkeeping which both keeps track of chosen elements subject to fiber rotation as well as allows for skipping calculating and storing arrays of zeros. An example of this is the element constitutive matrix gradient that exists only for the specific associated element to the considered design variable whereas the rest is null i.e. $\partial \mathbf{Q}_e / \partial x_i$ only has a value when the element belongs to a specific patch $e \in p$. All other $e \notin p$ are null. This is implemented in most of the framework, however, without exploited fully e.g. the cross section stiffness matrix is repeatably calculated even when no change have been made for example between objective and constraints evaluations. It is left for future work to further improve the framework.

The computational cost (time) of the cross section stiffness calculation and more are reduced by utilizing parallel computing with MATLAB's local parallel pool function. This also allows for the framework to be used on high performance clusters, although this have not been tested yet. The pool function allows MATLAB to utilize a computers multiple core by distributing the evaluations in a for-loop. As of now, this has been implemented for the cross section stiffness matrix evaluations and the strain, stress, and failure criterion evaluations since these were the most expensive. The cost of using parallel computing is the higher amount of RAM needed and some requirements to parameters being passed inside the loop.

A large part of the thesis work was dedicated to develop the framework and troubleshoot the sensitivities. One persistent sign error was found early in the project and in an attempt to locate the origin of this error, the rotation of the element material constitutive matrix was changed. Originally, this was a generated function from the symbolic computing environment Maple using a theory presented in [55], but was changed in an effort to rule out the sign error. The new calculation is attached in the appendix page 82.

CHAPTER 4

Validation of framework

This section presents the simplified study which was performed prior to the full blade optimization. The motivation is to investigate the framework robustness and gain experience regarding the two different solvers SQP (via *fmincon*) and IPOPT. The simplified study contains the optimum design of a sandwich cantilever beam, subjected to end twist-, end displacement-, eigenfrequencies-, stress-, strain-, and/or failure criteria constraints. The findings will aid in the full blade optimization by appropriate selection of problem formulation and starting point as well as having a functioning optimization framework with validated sensitivities.

4.1 Problem formulation

One of the aims of the parametric study is to obtain a suitable problem formulation for the optimization of the large scale DTU10MW reference blade. The idea is, that some formulations obtain the desired BTC response better than others due to the composition of choosing the objective, constraints and optimization algorithm. It is possible that one composition might achieve the global optimum where others will be stuck at local minimums and not reach the desired response.
To gain insight in this, four problem formulations are investigated: (**a**) minimization of compliance (**b**) minimization of tip flapwise deflection, (**c**) maximization of tip twist to flapwise loading (**d**) maximization of BTC effects towards feather, see page 45. The aim is to determine the problem formulation that will be used in the full blade optimization. Problem formulations (**a**) and (**b**) have the same purpose of minimizing the tip deflection i.e. obtain a stiff structure and to introduce BTC effects in the design, a constraint is defined with a minimum tip twist, $\left(u_{\varphi}^{tip}\right)^{min}$ for these two. This case is opposite for problem formulations (**c**) and (**d**), where the maximization of the bend-twist response is desired. Here, a constraint on the maximum allowable tip flapwise deflection, $\left(u_{y}^{tip}\right)^{max}$ is defined, such that the amount of BTC in the structure is limited. The deflection constraint is also highly relevant in WTB design, as discussed in section 3.2.
Common for the four problem formulations are the first two eigenfrequency constraints which have a lower and upper bound, meaning that the eigenfrequencies can lie anywhere in between f_j^{min} and f_j^{max}. Furthermore, for each patch of elements in the cross section, an upper, FI_p^{max}, and lower, FI_p^{min}, bound on the FI is defined. The lower bound might be redundant since the lowest value the FI can obtain is 0 since it is the fraction of element material stress/strain and the material limit value. If stresses or strains goes to zero, so does the FI. The design variables x_i can take any real numbered values between its bounds of x_{min} and x_{max} making it a continuous design variable. As discussed in section 3.5, industrial standards limits the available fiber angles to a few discrete values. Discrete values can not be directly applied to a gradient based solvers since functions and variables must be continuous to be differentiable. Nevertheless, the continuous fiber angles used as design variables in this thesis work will provide an estimate of how the optimal design could look although not directly applicable in the industry.

(a) *Minimize compliance*

$$
\begin{aligned}
\min_{\mathbf{x}\in\mathbb{R}^{n_{dv}}} \quad & C(\mathbf{x}) \\
\textbf{s.t.} \quad & u_{\varphi}^{tip}(\mathbf{x}) - \left(u_{\varphi}^{tip}\right)^{min} \leq 0 \\
& f_j^{min} \leq f_j(\mathbf{x}) \leq f_j^{max} && \forall j = 1, ..., n_f \\
& FI_p^{min} \leq FI_p(\mathbf{x}) \leq FI_p^{max} && \forall p = 1, ..., n_p \quad \wedge x_i \in \mathbf{x}_{dv} \\
& x_{min} \leq x_i \leq x_{max} && \forall i = 1, ..., n_{dv}
\end{aligned}
$$

(b) *Minimize tip deflection in flapwise direction*

$$
\begin{aligned}
\min_{\mathbf{x}\in\mathbb{R}^{n_{dv}}} \quad & u_{y}^{tip}(\mathbf{x}) \\
\textbf{s.t.} \quad & u_{\varphi}^{tip}(\mathbf{x}) - \left(u_{\varphi}^{tip}\right)^{max} \leq 0 \\
& f_j^{min} \leq f_j(\mathbf{x}) \leq f_j^{max} && \forall j = 1, ..., n_f \\
& FI_p^{min} \leq FI_p(\mathbf{x}) \leq FI_p^{max} && \forall p = 1, ..., n_p \quad \wedge x_i \in \mathbf{x}_{dv} \\
& x_{min} \leq x_i \leq x_{max} && \forall i = 1, ..., n_{dv}
\end{aligned}
$$

(c) *Maximize tip twist response to flapwise loading*

$$
\begin{aligned}
\min_{\mathbf{x}\in\mathbb{R}^{n_{dv}}} \quad & u_{\varphi}^{tip}(\mathbf{x}) \\
\textbf{s.t.} \quad & u_{y}^{tip}(\mathbf{x}) - \left(u_{y}^{tip}\right)^{max} \leq 0 \\
& f_j^{min} \leq f_j(\mathbf{x}) \leq f_j^{max} && \forall j = 1, ..., n_f \\
& FI_p^{min} \leq FI_p(\mathbf{x}) \leq FI_p^{max} && \forall p = 1, ..., n_p \quad \wedge x_i \in \mathbf{x}_{dv} \\
& x_{min} \leq x_i \leq x_{max} && \forall i = 1, ..., n_{dv}
\end{aligned}
$$

(d) *Maximize BTC effects towards feather*

$$
\begin{aligned}
\min_{\mathbf{x}\in\mathbb{R}^{n_{dv}}} \quad & \alpha(\mathbf{x}) \\
\textbf{s.t.} \quad & u_{y}^{tip}(\mathbf{x}) - \left(u_{y}^{tip}\right)^{max} \leq 0 \\
& f_j^{min} \leq f_j(\mathbf{x}) \leq f_j^{max} && \forall j = 1, ..., n_f \\
& FI_p^{min} \leq FI_p(\mathbf{x}) \leq FI_p^{max} && \forall p = 1, ..., n_p \quad \wedge x_i \in \mathbf{x}_{dv} \\
& x_{min} \leq x_i \leq x_{max} && \forall i = 1, ..., n_{dv}
\end{aligned}
$$

4.2 Simple sandwich beam

The validation study is performed on a sandwich cantilever and prismatic beam with top and bottom faces as CRFP laminae and a core between, since carbon fibers was found to produce the largest BTC effects c.f. section 2.2.1. The material properties are presented in table 4.2 and the material limits in table 4.3. The length and cross section dimensions are given in figure 4.1. The design variables are the fiber angles in the faces that can take values irrespectively of each other. The beam is subject to an end point load of 30kN in the positive y-direction creating internal shear forces and bending moments. The minimum tip deflection is obtained by having the fiber angles in the two faces go to zero and thus aligned with the beam axis. The beam have similarities to a WTB by having high stiffness (and high density) material far away from the neutral axis and a weak (and low density) core in between. It should be pointed out that a thin walled beam would have even more resemblance with a WTB, however, the present sandwich beam was deemed sufficient to validate the framework. The FE beam representation is modeled using 4 elements to a total of 13 nodes. The cross section grid is made with GMSH

with 728 Q4 elements and is based on the convergence study presented in section 2.5.

Table 4.2: *Material data for core material (Divinycell H60[22]) and CFRP materials[73] used in simple sandwich beam*

	E_{11} [GPa]	E_{22} [GPa]	E_{33} [GPa]	G_{12} [GPa]	G_{13} [GPa]	G_{23} [GPa]	ν_{12} [-]	ν_{13} [-]	ν_{23} [-]	ρ [kg/m^3]
Core	0.13	0.13	0.13	0.035	0.035	0.035	0.35	0.35	0.35	100
GFRP	142.0	9.81	9.81	6.0	6.0	3.77	0.3	0.3	0.42	1800

Table 4.3: *Material strength data for core material (Divinycell H60[22]) and CFRP materials[73] used in simple sandwich beam*

Stress [MPa]	$\bar{\sigma}^t_{11}$	$\bar{\sigma}^t_{22}$	$\bar{\sigma}^t_{33}$	$\bar{\tau}_{12}$	$\bar{\tau}_{13}$	$\bar{\tau}_{13}$	$\bar{\sigma}^c_{11}$	$\bar{\sigma}^c_{22}$	$\bar{\sigma}^c_{33}$
Core	3.5	3.5	3.5	1.6	1.6	1.6	-2.0	-2.0	-2.0
CRFP	1800	40	40	120	80	80	-1200	-220	-220
Strain [-]	$\bar{\varepsilon}^t_{11}$	$\bar{\varepsilon}^t_{22}$	$\bar{\varepsilon}^t_{33}$	$\bar{\gamma}_{12}$	$\bar{\gamma}_{13}$	$\bar{\gamma}_{13}$	$\bar{\varepsilon}^c_{11}$	$\bar{\varepsilon}^c_{22}$	$\bar{\varepsilon}^c_{33}$
Core	0.0269	0.0269	0.0269	0.4	0.4	0.4	-0.0182	-0.0182	-0.0182
CRFP	0.013	0.004	0.004	0.015	0.01	0.01	-0.009	-0.021	-0.021

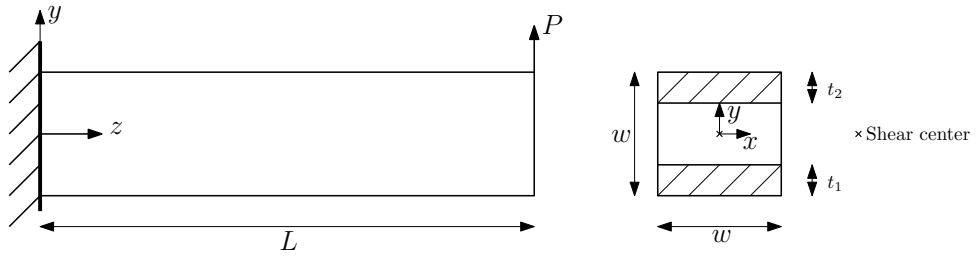

Figure 4.1: *Sandwich cantilever beam used for parametric study.* $L = 10m$, $w = 0.25m$, $t_1 = t_2 = 0.025m$, $P = 30kN$

4.3 The design domain

Considering a minimization of tip displacement in y-direction or maximizing the negative twist response of the simple sandwich beam presented in section 4.2 subject to two design variables that describe the fiber angles in the beam faces, a graphical presentation has been created to give insight into the design domain. A surface plot of the beam tip displacement in the y-direction and a surface plot of the end beam twist as function of face fiber angles are presented in figure 4.2a and 4.2b, respectively. Likewise, a contour plot of each response is also presented in figure 4.3a and 4.3b. The surface plots can reveal saddle-points, local minimum, and give a visual appealing interpretation of the design domain. Contour plots, presents the same design domain and global minimum is clearly determined, however, saddle-points and local minimums can be more difficult to interpret. Combined, the surface and contour plot provides valuable information of the design domain which can be utilized when defining the optimization problem. From these plots, the functions are determined as non-convex which is well known for optimization of composites structures using fiber angles as design variables. The twist response is likewise non-convex but with local minimums that easily can retain an optimization algorithm. For example, a starting point at the wrong side of the saddle-point

at [60;-60] will prevent gradient based algorithms to find the true optima, unless an "escape" mechanism has been build in.

As stated earlier, for a minimization of tip displacement in the y-direction, the angles in both faces must be aligned with the beam z-axis which is evident in both the contour and surface plots for the displacement with a global minimum at $\mathbf{x} = [0°, 0°]$. A maximization of the negative twist response through material BTC, requires the fiber angles in both faces to present values of approximately -20° to -30°. The fiber angles presenting the lowest deflection is not coinciding with the design providing maximum twist, thus both optimal solution cannot be obtained simultaneously.

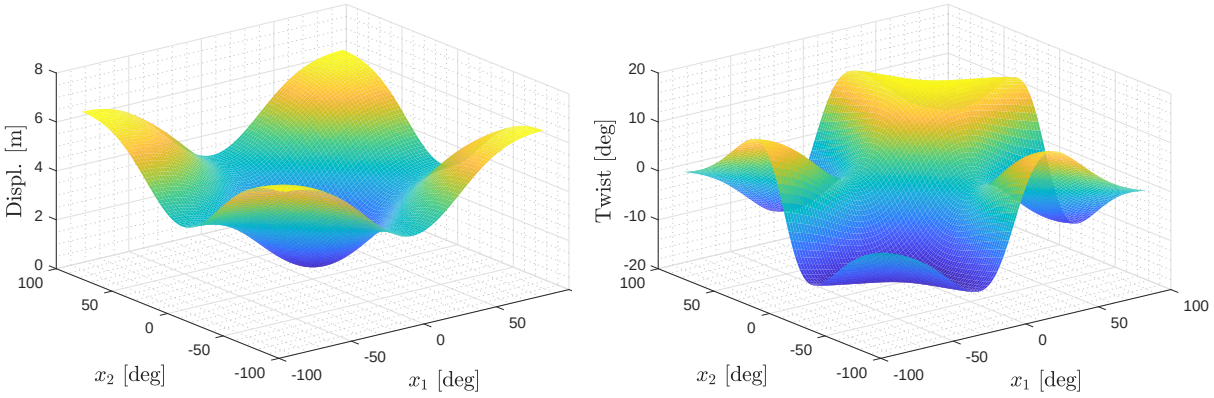

(a) *Displacement in y-direction* **(b)** *Twist around z-axis*

Figure 4.2: *Surface plots of the end point deflection and twist as function of top and bottom lamina fiber angles.*

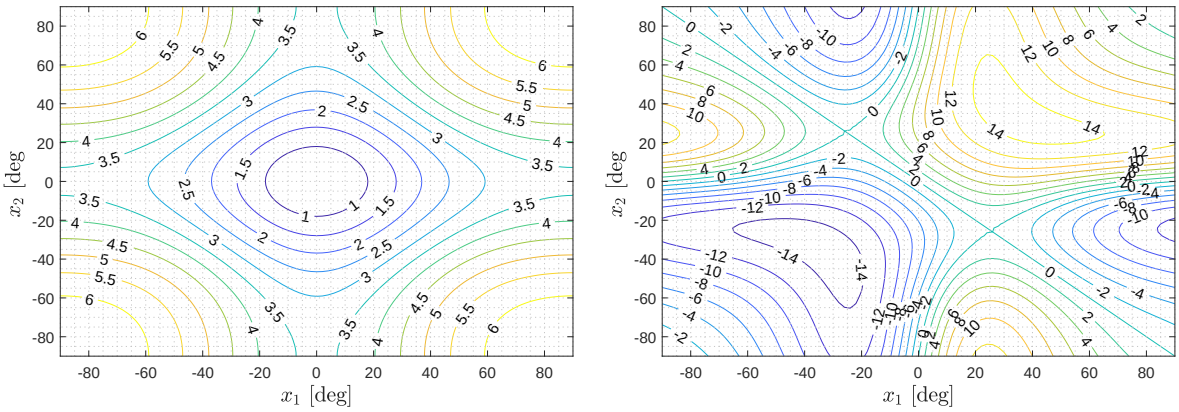

(a) *Displacement* **(b)** *Twsit*

Figure 4.3: *Contour plots of the end point deflection and twist as function of top and bottom lamina fiber angles.*

4.4 Testing the problem formulations and framework

The approach to developing the framework and performing the parametric study was to gradually implement and apply the constraints to the optimization problem until all constraint and sensitivities had been implemented. The results presented in this section includes all the implemented constraints defined in the four problem formulation on page 45 i.e. tip displacement, tip twist, frequencies, and FI's. Only the first two eigenfrequencies are considered with upper and lower constraints to limit the problem size. The four different failure criteria, discussed in section 3.2.2, have all been tested with the framework and most showed similar results, however, a few did not. The results presented in this section are for the Max Strain failure criterion. The defined constraint values and bounds are presented in table 4.4. As observed in the table, an additional test case, (**a***), is formulated which is a copy of (**a**) but with the objective compliance scaled to approximately 1 (originally in the order of 1e5). This provided an improvement in the number of function evaluations for the SQP algorithm, however, an increase for the IPOPT algorithm.

Table 4.4: *Defined constraint and bound values for considered problem formulations to validate framework.*

Constraint & bounds	(**a**)	(**a***)	(**b**)	(**c**)	(**d**)
$\left(u_{\varphi}^{tip}\right)^{min}$	-4°	-4°	-4°	-	-
$\left(u_{y}^{tip}\right)^{min}$	-	-	-	0.66m	0.66m
$[f_1^{min}; f_1^{max}]$	[5.0; 9.0]Hz	[5.0; 9.0]Hz	[5.0; 9.0]Hz	[5.0; 9.0]Hz	[5.0; 9.0]Hz
$[f_2^{min}; f_2^{max}]$	[9.0; 11.0]Hz	[9.0; 11.0]Hz	[9.0; 11.0]Hz	[9.0; 11.0]Hz	[9.0; 11.0]Hz
$\left[FI_p^{min}; FI_p^{max}\right] \forall p$	[0; 1.0]	[0; 1.0]	[0; 1.0]	[0; 1.0]	[0; 1.0]
$[x_{min}; x_{max}]$	$[-90°; 90°]$	$[-90°; 90°]$	$[-90°; 90°]$	$[-90°; 90°]$	$[-90°; 90°]$

The in-equality constraints are defined such that the optimum point will be $\mathbf{x} = [-5.614; -5.614°]$ with a tip end twist of -4°, a tip deflection in y-direction of 0.66m, eigenfrequencies of $\mathbf{f} = [7.421; 9.803]$Hz, and a FI index for each patch of elements in the cross section of 0.25. Thus, either the displacement or the twist constraint is active while remaining constraints are inactive given the bounds in table 4.4. Optimization formulations with alternating active constraints and using the SQP-method have also been tested and verified to converge to an optimum point on the constraint boundary, however, these results have been left out of this thesis report due to abbreviation.
Two starting points are selected as $x_{initial,1} = [-40°, -60°]$ and $x_{initial,2} = [0°, 0°]$ for the design variables where x_1 is the fiber angle in the bottom lamina and x_2 denotes the fiber angle for the top lamina. For (**a**), (**a***), and (**b**) the starting point $x_{initial,1}$ is feasible whereas $x_{initial,2}$ is not. Contrary, for (**c**) and (**d**) the starting point $x_{initial,2}$ is feasible whereas $x_{initial,1}$ is not. The solvers are therefore tested from both a feasible and non-feasible point. Both design variables are subject to the bounds $x_{min} = -90°$ and $x_{max} = 90°$ for all problem formulations.
Figure 4.4 presents number of function evaluations for the problem formulation created to test the framework and aid in the selection of proper formulation for the full blade optimization. That is, the number of function evaluations needed to converge to a stationary point of which no decrease in objective can be obtained in all feasible directions. It is divided into four bundles where the optimization algorithm performance, IPOPT and SQP, are compared from two starting points. Each bar corresponds to a problem formulation, defined on page 45, with the constraint values and bounds presented in table 4.4. For both starting points, the IPOPT for

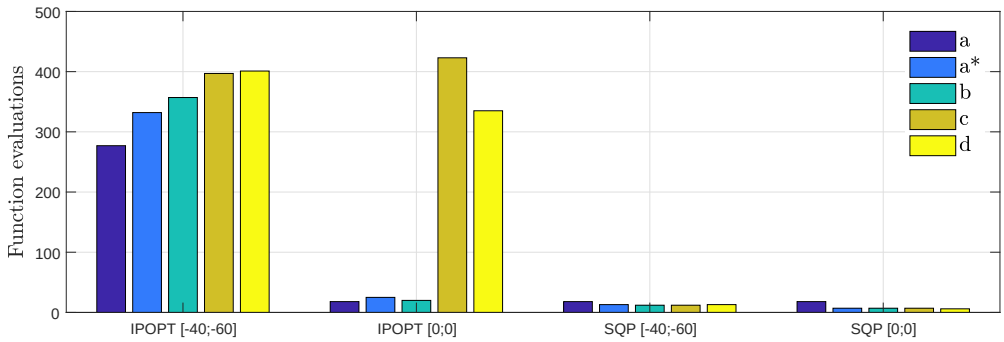

Figure 4.4: *Function evaluations for tested formulations with algorithms IPOPT and SQP from two different starting positions: (**a**) minimize compliance - (**a***) minimize scaled compliance - (**b**) minimize tip tip deflection y-direction - (**c**) maximize tip twist around z-axis - (**d**) minimize BTC factor.*

(**c**) and (**d**) shows a very slow convergence towards the optimum while for (**a**), (**a***) and (**b**) it only shows a slow convergence when the starting point is $[-40°; -60°]$. A possible interpretation of this is that IPOPT either takes small steps (starting point is relatively far from optimum for $[-40°; -60°]$ for cases (**a**), (**a***) and (**b**) but close to optimum when the starting point is $[0; 0]$ for the same cases) or that its performance is related to feasible versus non-feasible starting points, that is, starting points where the constraints are violated to a larger extend. The final fiber orientations at the end of the optimization is plotted in figure 4.6 for $\mathbf{x}_{initial} = [0; 0]$ and in figure 4.5 for $\mathbf{x}_{initial} = [-40; -60]$. Here it is observed that only one formulation, minimization of twist (**c**), failed to converge to optimal point and ended with a relative error of approximately 26%. For the starting point $\mathbf{x}_{initial} = [-40; -60]$, IPOPT only converged to acceptable values for formulations (**a**) and (**b**) with relative errors of less than 1%. The formulation case (**a***) converged to a point with ±5% error of the bottom and top fiber angle respectively. The final two formulations, (**c**) and (**d**), presents significant errors up to approximately 265% for $x_{initial,1}$.

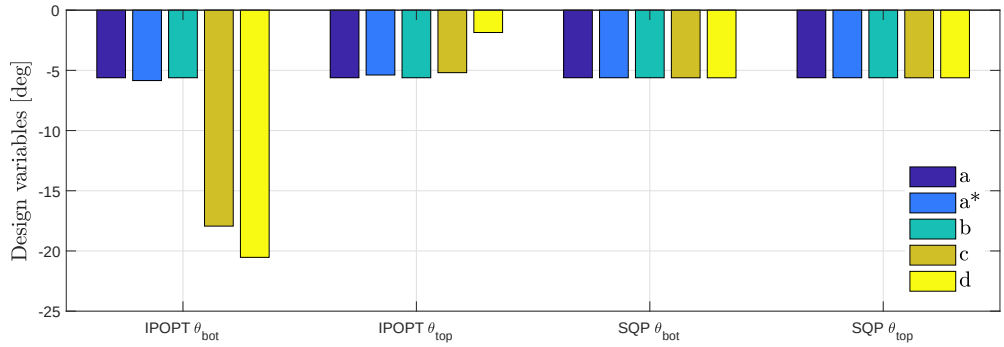

Figure 4.5: *Converged top and bottom fiber angle for tested formulations with algorithms IPOPT and SQP for starting position $x_{initial,1} = [-40°; -60°]$: (**a**) minimize compliance - (**a***) minimize scaled compliance - (**b**) minimize tip tip deflection y-direction - (**c**) maximize tip twist around z-axis - (**d**) minimize BTC factor.*

SQP shows much more consistent results where all formulations converged to global optimum. The highest function count of 18 for both starting points was reduced to 13 and 8 for $\mathbf{x}_{initial} = [0; 0]$ and $\mathbf{x}_{initial} = [-40; -60]$, respectively, by scaling the compliance to approximately unity. Needless to say, SQP presents by far the quickest convergence towards global optimum whereas IPOPT both is significant slower and fails to converge to global optimum in 5 out of 10 cases.

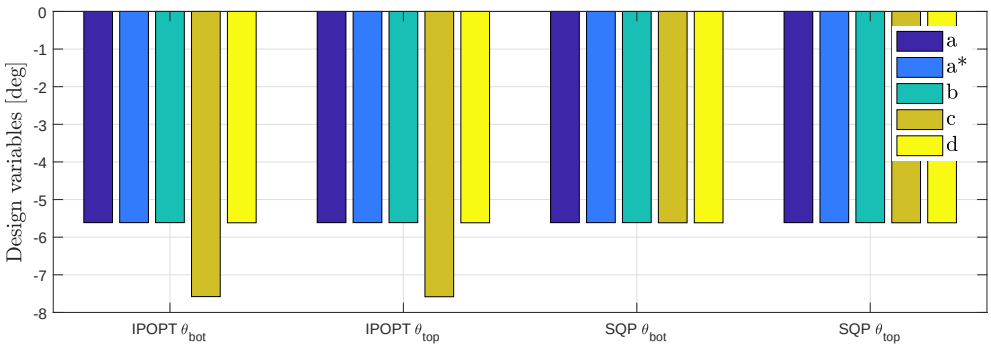

Figure 4.6: *Converged top and bottom fiber angle for tested formulations with algorithms IPOPT and SQP for starting position* $x_{initial,2} = [0°; 0°]$*: (**a**) minimize compliance - (**a***) *minimize scaled compliance - (**b**) minimize tip tip deflection y-direction - (**c**) maximize tip twist around z-axis - (**d**) minimize BTC factor.*

Based on the study presented in this chapter, SQP with any starting point is predicted to show good performance and convergence to constrained optimum, although a constrained global optimum cannot be guaranteed for the full blade optimization. The simplified composite beam presented here is too simple (prismatic and simple geometry) to transfer the presented design domain directly to the design domain of a WTB. More discussion on this in chapter 5.

4.5 Discussion on results

The above presented results show a clear favor for the SQP algorithm, however, it should be noted that IPOPT is generally considered as a robust and fast solver and such a small problem, as the one investigated, should be no problem for IPOPT. In fact, equal performance was expected from the two algorithms, thus, it is very surprising that IPOPT shows evaluations counts many times higher. Even more peculiar, the poor performance is only present for some of the problem formulation cases. Without being able to provide any evidence, a bug must be present in the framework. Some of the things considered and investigated as the cause are sensitivities, bounds on constraints, scaling, and passing of the parameters to IPOPT. The sensitivities have been subject to a repeating validation check using the self defined finite difference checks without locating any errors, and furthermore, the same sensitivities are used with SQP. The bounds and scaling, if not defined properly, could be the cause, however, again the same are used for SQP with the addition of lower bounds for IPOPT which are selected sufficiently large e.g. -20° for (**a**), (**a***) and (**b**). When passing the Jacobian (sparse array with design sensitivities) to IPOPT, one can pass a zero-one array along with it, where each non-zero entry defines a non-zero gradient value in the Jacobian. Now, for such a small problem, the zero-one array is easily identified and to be sure, one can leave it out and IPOPT will assume a full Jacobian. This and more have been tried to no avail, and it is left for future work to locate the bug. Instead, the SQP algorithm is selected for the blade optimization.

CHAPTER 5

Full blade optimization results

- interpolated to more sections along beam as described in 2.3.2.

This chapter presents the results obtained for the DTU10MW reference WTB optimization for BTC effects. The validated framework and most promising problem formulations from chapter 4 are used in this study and findings are presented. Relevant findings in literature are presented to illustrate what to expect and an introduction to the design of the WTB is presented followed by obtained optimized designs. Unfortunately, the results are not what was desired and only to some degree correspond to findings in literature. Different approaches have been tried to solve this which will be discussed.

5.1 Literature findings

Ong and Tsai[51] investigated the benefits of changing unidirectional glass fibers in the spar cap of a SERI-8 blade to carbon fibers and also included models where the carbon fibers where 20° off blade axis. This angle was based on earlier studies by the same authors where they maximized the BTC parameter in D-spars and verified this experimentally[50]. In their work, they concluded that changing fibers from glass to carbon and orienting them 20° off axis mitigated a reduction in the flapwise bending stiffness of the blade. They concluded the modified blade maintained its structural integrity with wind speeds up 70m/s.
Bottasso et al.[9] performed structural optimization with a prescribed aerodynamic shape for a 2MW rotor blade where the aim was cost minimization. The framework presented in the paper, contained multilevel analysis tools such that a complete load envelope and fatigue loads are considered by a multibody aero-servo-elastic simulation. For each iteration and design change, strain and stress evaluations are made on a FE low level beam model with cross sections evaluated using their own implementation of Giavotto[29], thus have similarity to the software used in the present study. Their findings showed significant stress concentrations between the root and the maximum chord regions (approx 1/3 from root towards tip) and concluded that the effects were not captured on the cross section discretized model level.
Bottasso et al.[10] also used their optimization framework for designing a 45m rotor blade for a 2MW wind turbine with BTC effects with the purpose of load alleviation. They conclude that BTC for load alleviation by twist to feather is possible and indeed reduces fatigue damage in the blade. Furthermore, their study showed benefits of including off axis unidirectional (UD) fiber rotations in the shells by obtaining the same amount of BTC as only changing the caps fiber angles could present. This resulted in less increase in weight and less reduction in bending stiffness. The paper also presented a parametric study on partially coupled blades, meaning that only part of the blade is subject to fiber rotations. The conclusion was that avoiding fiber rotations from the blade root to about the span of maximum chord is beneficial in the sense that benefits from rotating the fibers near root increases fatigue damage and only contributes slightly to the coupling.
Bagherpour et al.[2] recently investigated BTC and load mitigation effects in the DTU10MW reference WTB as a demonstration example of their tool *hGAST*. They concluded that no power

loss were present due to BTC effects and that, maximum BTC was obtained at 22.5° which was selected based on their literature findings. This paper was found during the thesis project period and their aims are very similar to the problem formulation for this thesis work. Bagherpour et al.'s research will be used to compare the optimized blade design, obtained in this study.

From the above findings, a rather detailed picture of how the optimized design will look for optimum BTC effects can be deducted. Fiber angles of approximately 20-22°, positive towards leading edge from mid axis in caps and possibly also in shells, will provide the desired BTC. Furthermore, to limit loss of bending stiffness, glass fibers can be substituted with carbon fibers and inclusion of shells to the design variables may also mitigate this. Selecting correct spanwise sections will lessen the computational burden in the form of fewer design variables but will still allow for high couplings in the blade, as found from [10] above.

5.2 Introduction to reference wind turbine blade

5.3 sec:IntroductiontoReferenceWTB

This section presents a small introduction to the DTU10MW reference WTB[3]which can be acquired from [21]. The wind turbine and rotor blades were designed at the Technical University of Denmark (DTU) as part of a Light Rotor project. The blade is 86.4m in length and, in this study, partitioned in 27 section along the blade span, see figure 5.1 and 5.2. The blade cross section is sectioned into patches as blade sub-parts as defined in figure 5.3 (following a template file accompanying BECAS) and the material layup of each sub-part is presented in the appendix page 85 as well as the material properties and strength limits on page 84. Following the divided cross section in figure 5.3, each patch will have a more or less uniform stress level (except parts crossing the chord line e.g. webs where flapwise bending produces compression at the suction side and tension at the pressure side), and thus a single FI can be considered for each patch instead of each cross section element. The maximum FI of all the elements in a patch is used when evaluating stress constraints, as discussed in section 3.2.2.

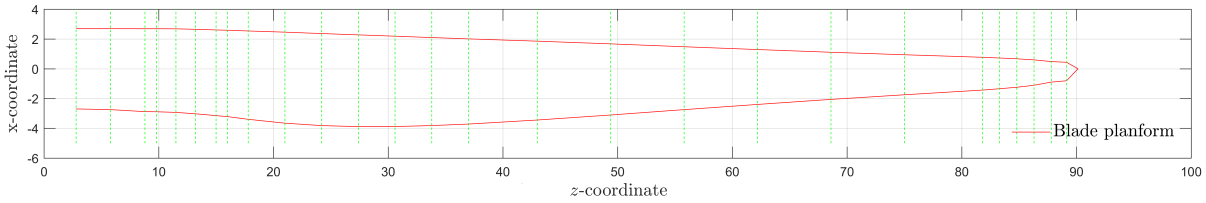

Figure 5.1: *DTU10MW reference WTB planform, green vertical stippled lines are placements of cross sections.*

Without any modifications to the blade, the response to the selected load case, presented in section 2.6, is a flapwise tip deflections of 13.54m and a tip twist response of -2.537°. The first two eigenfrequencies of the WTB (1^{st} flapwise and 1^{st} edgewise) is $[0.619; 0.947]$Hz and the maximum FI for each section using the different failure criteria, presented in 3.2.2, is illustrated in figure 5.4. A rather unfortunate discovery is made with this plot, since the original design violates Max Stress and Tsai-Wu failure criteria significantly for almost the entire span of the blade. Only the Max Strain criterion presents values below the FI constraint maximum value of 1.0. Although alot of time has been invested in looking for a cause and solution for this, one could not be found. It is most likely that the blade design, available from [21] with the provided layup and cross section discretizations, only has been tested in BECAS with Max

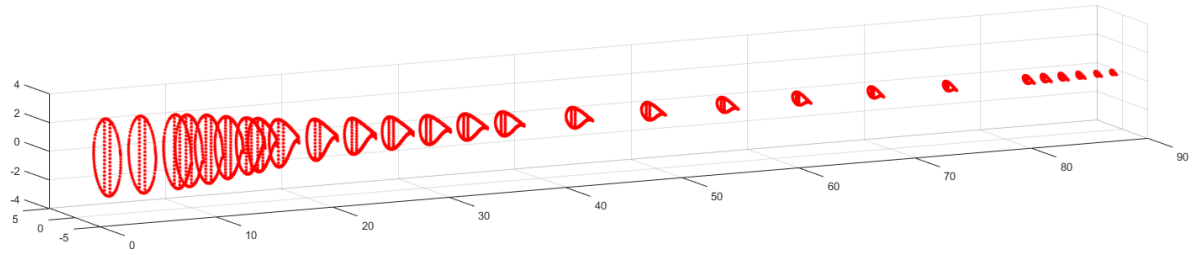

Figure 5.2: *DTU10MW reference WTB cross sections.*

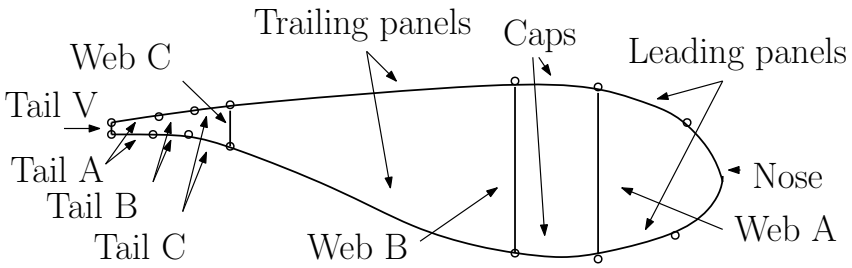

Figure 5.3: *Blade cross section patches*

Strain criterion and thus constructed to fulfill this. The FI constraint violation is similar for several random checks of the different load cases and is assumed to present the same for the all 14 load cases available. The solution for this issue has been to only use Max Strain criterion in the full blade optimization, since this is the only one not violated from the original design. Another possible solutions could be to try the optimization scheme regardless of the initial design constraint violation, and see if the framework can provide a design that does not violate failure criteria constraints.

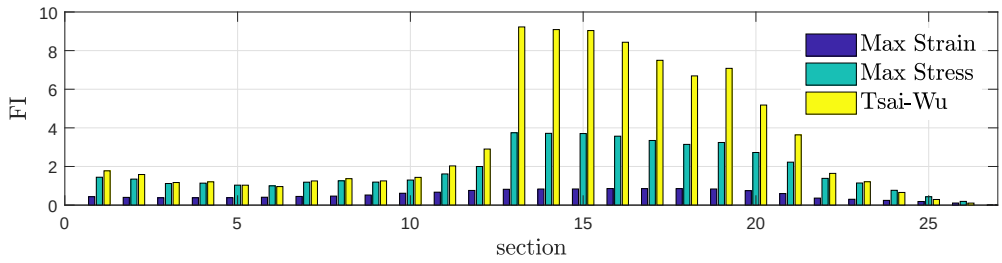

Figure 5.4: *Max Strain, Max Stress and Tsai-Wu failure criteria for the initial blade design considering load case 9 (see section 2.6).*

Another possible cause could be high stress concentrations at e.g. connections between webs and caps. An example is given in figure 5.5 where the Max Stress FI is 2.7 (recall that it must be <1.0 for no failure to be predicted) for the stresses in the transverse direction in the material coordinate system σ_{33}. Investigating this further, it seems that this sort of concentration is present throughout the blade and is the cause for both the high Max Stress and Tsai-Wu FI's. A mesh refinement might mitigate this, however, this could also be a more severe problem of the node connection between webs and caps. More time is needed to investigate this or change the framework to not consider stresses in the transverse direction but is left for future work. Instead the Max Strain criterion is used.

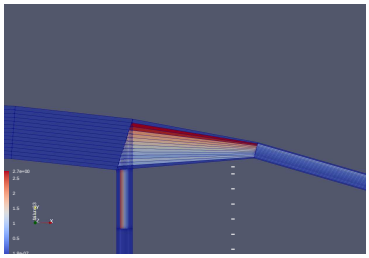

(a) *Close up of stress concentration*

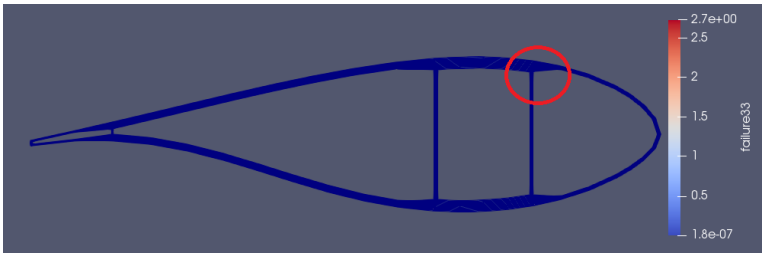

(b) *Cross section*

Figure 5.5: *(**a**) Close-up of FI for Max Stress criterion and (**b**) cross section number 20 with Max Stress FI pr. element for transverse stresses σ_{33} in the material coordinate system, made with ParaView*

5.4 Optimization of wind turbine blade

In this section, it was desired to present a converged optimal design for BTC effects in the blade, obtained with both IPOPT and SQP. The constraints of eigenfrequencies, displacement or twist, and failure criteria should not be violated since this will mean that the blade would fail. Both algorithms fail to converge to a result where a significant increase in the twist response is obtained and where constraints are not violated. Judging on the history of the optimization scheme, the optimization algorithm show little convergence to the design found in literature, that being fiber angles of 20° off-axis.

Constraints and bounds defined for the optimization are a maximum displacement of $\left(u_y^{tip}\right)^{max} = 20\text{m}$, an upper and lower bound for the first eigenfrequency of $\left[f_j^{min}; f_j^{max}\right] = [0.2; 0.7]\text{Hz}$ and for the second eigenfrequency of $\left[f_j^{min}; f_j^{max}\right] = [0.8; 1.4]\text{Hz}$, and a Max Strain FI lower and upper bound of $\left[FI_p^{min}; FI_p^{max}\right] = [0; 1.0]\,\forall p$. The eigenfrequencies bounds are defined based on the starting values for the original blade design and, with fiber angles being rotated off axis and thus lowering the stiffness, taken into account the decrease in eigenfrequencies values. This gives some room for the optimization to reach higher values of fiber angles. The maximum displacement is somewhat arbitrary chosen and was selected to see how much BTC effect the optimization algorithm could obtain. A more realistic displacement bound is the maximum allowable displacement based on the loaded WTB tip distance to the tower including tilt and cone angles stated in[3]. The non-loaded WTB-tower clearance is stated as 18.3m while the minimum tower clearance during DLC1.3 is 5.9m resulting in a tip deflection of 12.4m. Choosing this value as tip deflection constraint would pose no feasible point in the design domain since the original design, with defined extreme load case, already violates it.

5.4.1 Obtained results

Based on the literature findings, a choice was made to change the TRIAX (fiber mats with $[-45, 0, 45]$ fiber angles) layers in the cap to UNIAX (fiber mats with a single fiber angle) due to higher effects of changing fiber orientations achieved with the more anisotropic material. Initial optimization was performed with the SQP algorithm from a starting point of [0° ;0°] with the load case 9 distribution applied to beam nodes and the through thickness descritized with 8 elements resulting in 9 design variables pr. considered section (from section 11 to 27 based on literature findings) to a total of 136 design variables. The problem formulation **(c)** (maximization of negative twist response) with only the displacement constraints enabled

was used and the algorithm reached a stationary point in 29 iterations with 80 function calls where the displacement constraint was satisfied. Unfortunately, the objective function actually increased to present lower coupling though fiber rotations where all positive. Time was invested to figure out why this was so, with special focus on the twist gradients, however, the problem seemed to be the applied loads. An error was indeed discovered that prevented updating the F1D.in file to FRANS with the loads. Better convergence was now obtained, however, the objective did not present the desired improvement that is a larger tip rotation.

To see if this effect was unique for the problem formulation, optimization using formulation (**d**) (maximization of BTC effects by minimizing the BTC factor) and SQP was also performed and still only considering a displacement constraint and starting point as above. A limit of 500 function calls was set which was reached in 247 iterations taking approximately 10.4 hours without reaching an optimum. A summary of the optimization history can be observed in figure 5.6. From 5.6a a rather peculiar phenomenon is observed. Where the maximization of twist response through a minimization of twist value is expected to show all positive fiber angles.

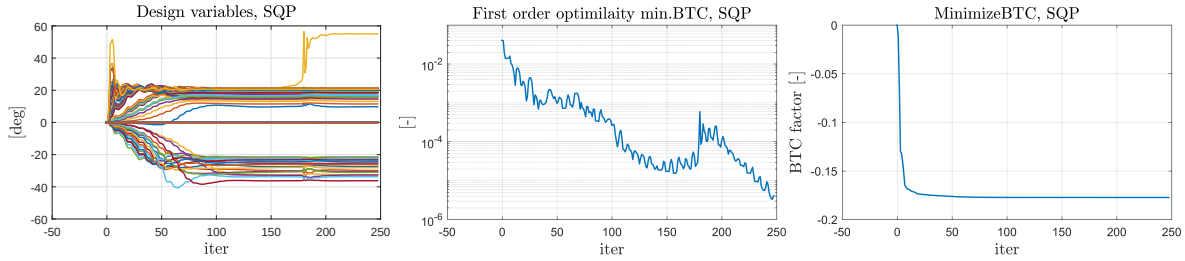

(a) *Design variable history* **(b)** *1st Order Opt.* **(c)** *Objective history*

Figure 5.6: *History for maximization of twist response by minimization of the BTC factor for each considered section weighted equally for the full scale blade using SQP and a single tip displacement constraint.*

In an effort to achieve a better result, the fiber angles in the shells were also included as design variables and the TRIAX layers were changed to UNIAX. This was done to see whether the change in fiber angles in caps alone was insufficient to generate the desired BTC effects. This slightly improved the end twist to -3.158° but ended in an in-feasible point since the displacement constraint was violated with by 20%.

In a last effort, the IPOT algorithm was used with problem formulation (**b**), based on the discussion made in section 4.4, and constraints on the twist of $\left(u_{\varphi}^{tip}\right)^{min} = -4.5°$. Design variables showed more consistency with literature findings by obtaining values near 20° however could not converge to a stationary point before max CPU-time of 12 hours was reached.
The closest to an optimum blade design achieved with IPOPT for formulation (**b**) considering fiber angles in both caps and shells and all defined constraints is presented in figure 5.7. However, final design show significant flapwise tip deflection leading to the conclusion that the desired BTC effect is set too high. Furthermore, FI from the Max Strain failure criterion could not be kept beneath set maximum value for sections 15 to 21 corresponding to the spanwise section 37-75m. The design cannot be said to have converged to a local minimum since constraints are violated.

In order to simplify the problem, the number of design variables are reduced to a single fiber orientation for each of the sections 11 to 27. The load was changed from a distributed load

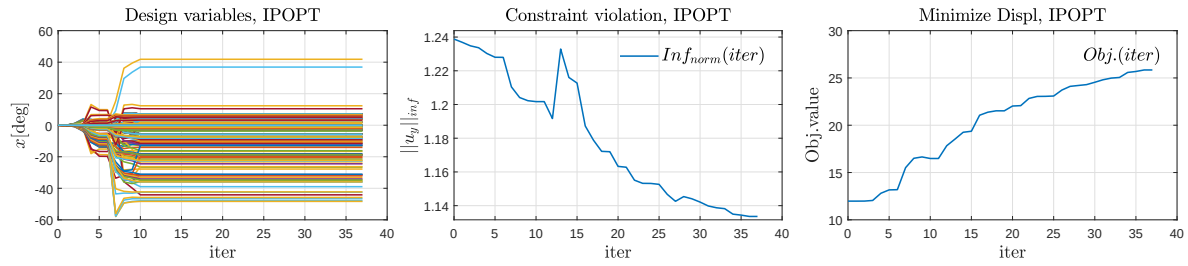

(a) *Design variable history* **(b)** *Constraint violation* **(c)** *Objective history*

Figure 5.7: *History for minimization of flapwise tip deflection with a constraint on the minimum tip twist for the full scale blade using IPOPT and defined constraint for problem formulation (**b**).*

based on the values obtained in section 2.6, to a single point load of 100kN applied to the end node of the end last element in the tip of the blade. By alternating the 17 design variables between the bounds [-30°;30°], the figures 5.8a and 5.8b was created. Here, the displacement response (constraint) and twist response (objective) is presented as a function of fiber angles when all 17 design variables are equal. As expected, 5.8a presents an increase in tip deflection in the positive y-direction as fiber angles moves away from the 0° point. In 5.8b the twist response behavior is more or less as expected, with decreasing twist angle with decreasing fiber angle rotations, however, the change in objective is smaller than expected. Comparing to literature, Bagherpour et al.[2] presented a tip twist of up to 5.5° for fiber angles of approximately 20°, which could not be reproduced.

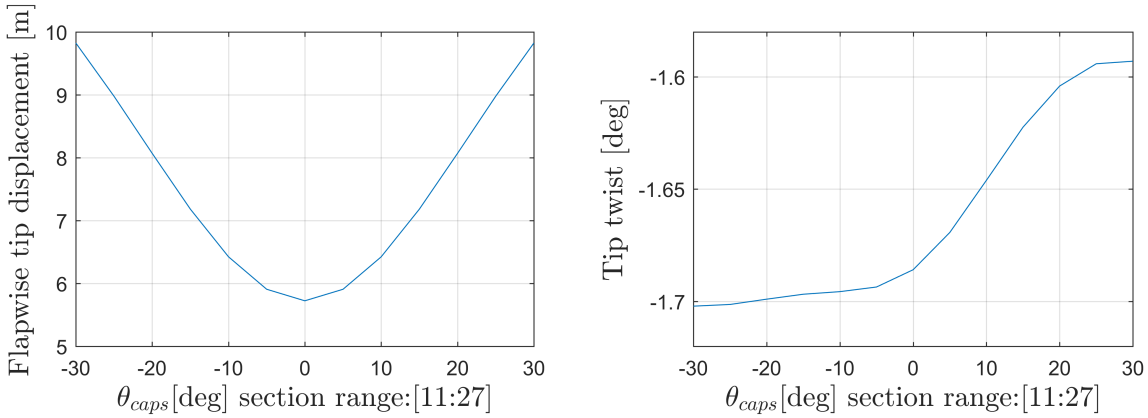

(a) *Tip displacement* **(b)** *Tip twist*

Figure 5.8: *Tip displacement in the y-direction and twist response around z-axis for a positive flapwise loading*

Knowing that there exists an optimum for the very simple case, a tryout is performed to see if similar results can be obtained with a more realistic load setting. Using load case 9 and the reduced number of design variables to a single fiber orientation in the caps per considered sections 11 to 27, a minimization of the twist response (**c**) with a displacement constraint of 20m was performed using the SQP algorithm. The optimization history is presented in figure 5.9 and shows a converged result in 114 iterations with 244 function evaluation. The 17 design variables converged to near -20° angles with a final objective twist of -2.993°. The objective function value decrease shows a lower value than what could be obtained from other optimization runs and therefore this design is selected to transfer to HAWC2 and observe in a aeroelastic setting in chapter 6.

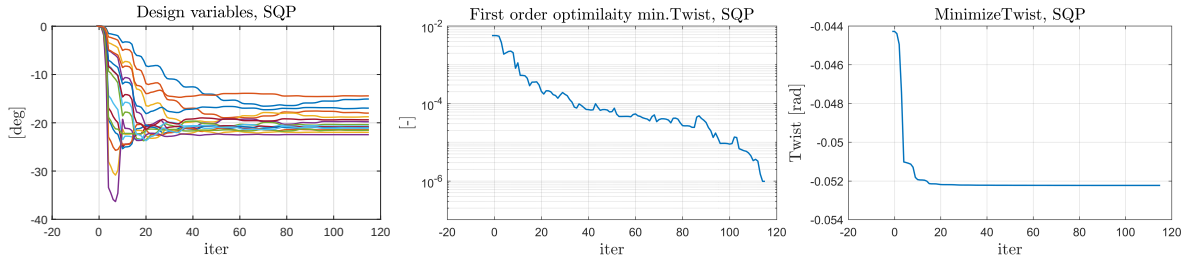

(a) *Design variable history* **(b)** *1^{st} Order Opt.* **(c)** *Objective history*

Figure 5.9: *History for minimization of tip twist rotation value with a constraint on the maximum tip deflection for the full scale blade using SQP for problem formulation (**c**).*

5.5 Discussion on implementation and results

This section discusses what is thought to be causing the problems with the framework that prevents the optimization algorithms to converge to optimal or local solutions with a significant change between initial and final twist.

5.5.1 Sensitivities

First thought that comes to mind is the sensitivities to be the root of the problems. There is no question that providing wrong gradients to a gradient based numerical optimization algorithm provides little chance for the algorithm to select appropriate search directions. The continuously returning of in-feasible design points, where the constraints are violated, those indeed lead to the notion that something is amiss with the gradients. A significant amount of the project time has been used on obtaining analytic expressions, implement in the framework and validate gradients with central finite difference gradients. However, most of the validation was made with the simple composite beam case to test the framework, since it was deemed to time consuming to redo the sensitivity validation for the WTB as well.

5.5.2 Changing layup and thickness

Although some effort was made to investigate this, further research into the benefits of where the fiber angle changes are made is needed. Findings in literature, described in the beginning of this chapter, showed that both caps and shells could be considered and that BTC could be obtained for different and smaller sections along the blade by rotating the fibers to higher angles. A consistent and structured investigation into this is needed to compare the benefits or disadvantages of this. Some conclusions may be transferred from Bottasso et al. [10], however, there's a significant difference between the 2MW WTB used in the paper and the 10MW WTB used in present study. In the same paper, Bottasso et al. mentioned that laminate thickness also plays a role regarding how much BTC that can be obtained. With more investigation into this subject, the final objective value might be able to be increased further.

5.5.3 Loads

The loads selected was chosen to give a conservative design, however, the edgewise bending load might be preventing the blade to twist and the extreme flapwise bending might prove to high to obtain the desired twist without violating the displacement constraint. Reducing the flapwise bending loads and excluding the edgewise loading may prove to allow better convergence and less constraint violations since constraints are defined from structural considerations. Another

issue with the load might be a wrong direction of application or a wrong sign. The coordinate system should be double checked with the F1D.in file to make sure distributed loads are applied on the nodes in correct nodal d.o.f.
Recall the initial blade design twist of -2.5374° (original design). This response indicates that transferring load applications point to shear center is insufficient since a simple point load parallel to the cross section through shear center should produce no torsion. The shear center is defined by BECAS based on the cross section stiffness terms and thus should successfully capture both geometrical and material couplings. In fact transforming loads to shear center would lead to no improvements in the optimization objective, because the shear center would change with changing fiber angles.

5.5.4 Higher discretization

Increasing number of element in the cross sections will increase the detail and might capture more of the anisotropic material orientation effects. No convergence study was made for the mesh sizes and thus results might be mesh dependent meaning one discretization will provide one result while the next is significantly different. The python program, shellexpander.py, used to import and discretize the cross sections can easily add more elements through thickness of the laminates, however, to the authors knowledge, the circumferential discretization for caps, shell, leading- and trailing edge and width-wise discretization of the webs cannot be discretized further. Another aspects of this is the RAM usage of the framework, when more design variables are added. As of now, the limit is approximately 700 design variables in total before stored arrays becomes to large. This has to do with the inefficiencies of the storage (even temporary) of the strain, stresses and failure indexes. Six strain/stress/FI elements are stored for each considered cross section for each cross section element. This is multiplied with number design variables i.e. N-by-n_e-by-6-by-n_{dv} (or N x n_e x 6 x n_{dv}) is a significant amount of storage needed. Some efforts have been made since a lot of this is just stored zeroes e.g. for the cross section matrix gradients, however, there is still room for improvements e.g. utilize sparse storage could show beneficial.

5.5.5 Coordinate system

In referenced papers in the beginning of this chapter, fiber angles are reported as positive towards the leading edge for the BTC blade design which is not in accordance with findings in the present study. This implies that the framework might be operating with a wrongly turned coordinate system. The coordinate system considered in BECAS has been the x-axis towards the leading edge of the blade, the y-axis positive towards the suction side, and z-axis along the span with beginning at root end. The coordinate system in FRANS is likewise so it is not obvious where the error occurs.

CHAPTER 6

HAWC2 results

This chapter presents the comparison of the original DTU10MW reference WTB response with the optimized WTB design response when subject to time domain simulations in both steady-state environment as well as in a turbulent wind field i.e. DLC 1.3. The flapwise deflection, the rotation around the longitudinal axis, and the root bending flapwise moments will be compared. The fatigue equivalent damage can be used to observe the load mitigation effects, however, a dataset was not successfully created during this study. Instead, a small discussion is presented.

6.1 HAWC2

The Horizontal Axis Wind turbine simulation Code 2 (HAWC2)[38], developed by DTU Wind Energy, is an aeroelastic simulation software intended for calculating wind turbine response in the time domain. It is very suitable for this project, since BECAS contains an export function, allowing for the optimal blade design to be exported to HAWC2 in correct format. Furthermore, the DTU10MW reference wind turbine model is distributed with HAWC2. This makes for an easy update of the WTB since one can almost directly overwrite the blade structural file and use the same turbine model and control in the simulations. Thus, comparison of the responses and mitigation effects is directly available.

6.2 Comparison of blade response during steady state

In this section, the original blade response in a steady state environment with just below rated wind speed is compared to the optimal blade design in the same environment. The motivation is to see the flapwise and torsional loading as well the blade response in the form of flapwise deflection and twist. Furthermore, to locate possible issues, e.g. resonance, with the new blade design, a stepped wind profile is simulated. This will reveal the blade response and the wind turbine control behavior through the entire operational wind speed interval.

6.2.1 Steady state and turbulent wind field with single wind speed

The steady state denotes a steady wind speed with no turbulence such that the only difference in wind speed seen by the blades are from the shear, meaning the increase in wind speed as one goes to higher altitudes. In the steady HAWC2 simulations, a power law is used with a shear factor of 0.2 for the wind shear and only a horizontal wind vector component. Figure 6.1 presents selected responses in a steady wind field and in a turbulent wind field. the oscillating signal for the steady wind field measurements is due to the wind shear, where the blades experience a maximum and minimum in relative wind speed once per revolution. The first row in figure 6.1 presents the flapwise bending moments at the root end of the WTB, the second row presents the WTB tip deflection in the y-direction (see figure A.6 in appendix page 86 for the coordinate system used in HAWC2), and the last row presents the rotation of the aerodynamic center selected to represent the twisting of the tip.

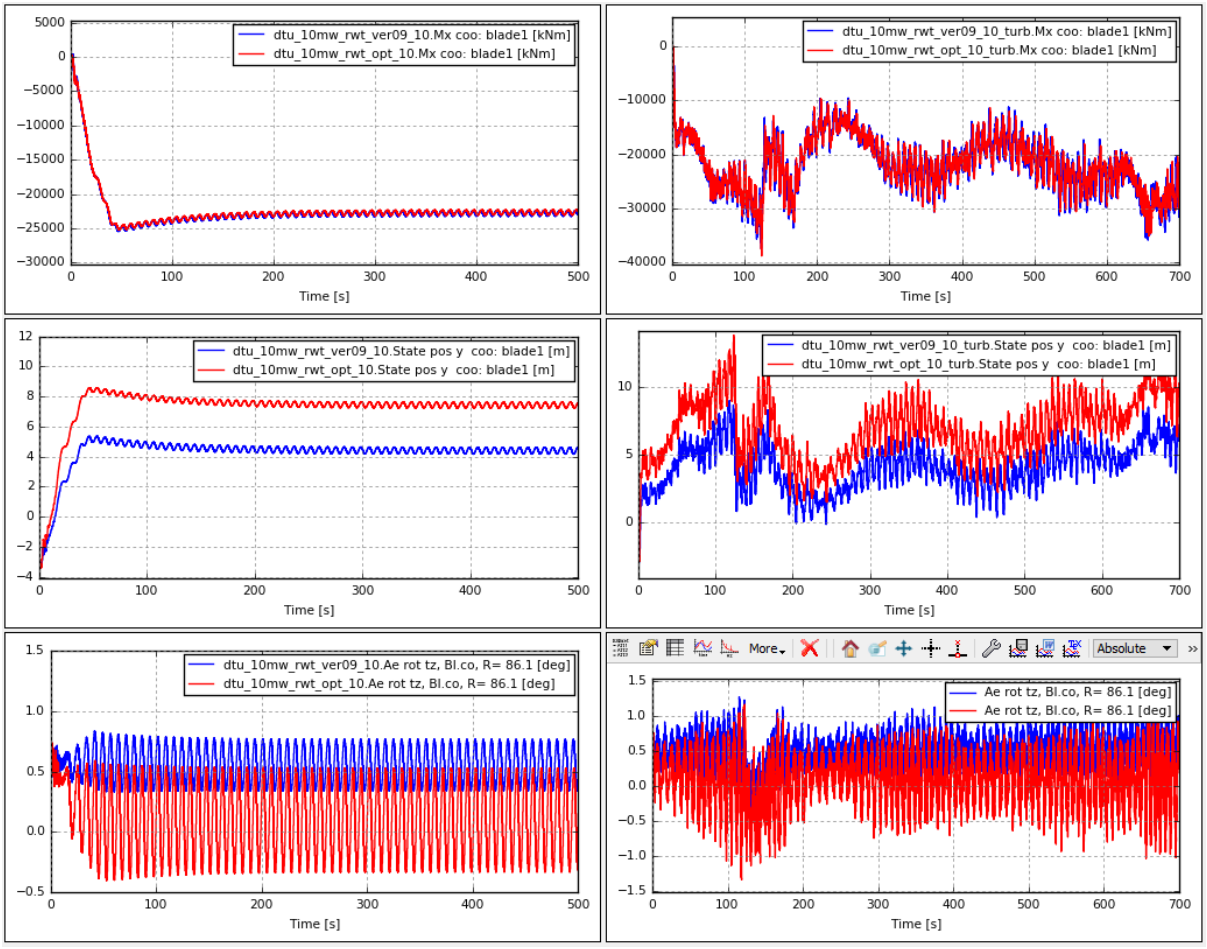

Figure 6.1: *Comparison of regular response between original blade and optimum blade for a wind speed of 10m/s. Blue signal is for the original blade design while red signal is for the optimized blade design.* ***Left*** *column: Steady state.* ***Right*** *Column: Turbulent wind field. Note the units are displayed in the legends.*

The sensor selected for the tip twist measurements has its basis in the aerodynamic module. It gives the local orientation of the chord related to blade root coordinates meaning that it is independent of pitch angle. The extracted angle is calculated in the closest aerodynamic point which is 1/4 chord also known as the aerodynamic center. The cross section with the measured blade twist, θ_z is presented in figure 6.2. Not that despite the orientation of the coordinate system, the twist is measured positive clockwise around z-axis following normal convention. The comparison between the original blade design and the optimized should therefore show a decrease in this angle as it is desired to have a negative rotation towards feather.

Concluding on the measured steady response, presented in figure 6.1, the root flapwise bending moment show little difference between the two blade designs, however one can observe the optimum design blade (red-line) to present a small reduction compared to the blue line. This is in good agreement literature findings, discussed in chapter 5, that the BTC effects can act as passive load mitigation. For the turbulent wind field, the load mitigation is not clearly visible and cannot be concluded from this plot.
The tip displacement in a steady wind field shows approximately 4m of extra deflection for the BTC blade compared to the original design. This is a major cost that likely will prove

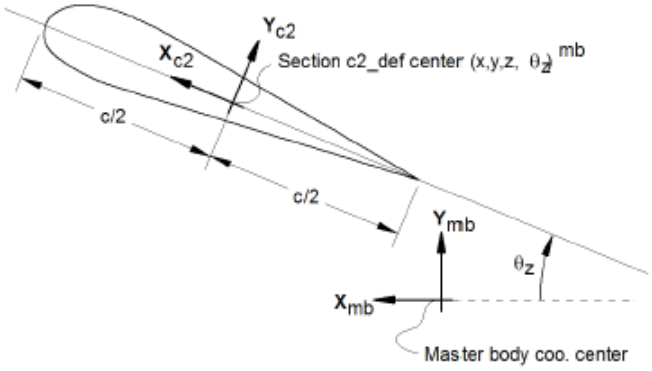

Figure 6.2: *Cross section of WTB as used in HAWC2[38] showing measurement of twisting angle with reference coordinate system being the **m**ain **b**ody coordinate system of the blade.*

troublesome in higher wind speed regions where gusts and turbulence will cause much higher deflections. For the wind speed of 10m/s, pitching of the blade have not yet initiated, which will not be done until the reference generator shaft rotational speed is surpassed near 11.4m/s, which is the DTU10MW reference wind turbine rated wind speed. For the turbulent wind field, high displacements are observed which reaches near the maximum allowable tip displacement. The last 2 plots in figure 6.1 presents the blade twist measured at the tip of the blade (86m radius). The blade pre-twist (used to optimize performance of the blade in the below rated wind speed region) of 3.43° is subtracted the signal to provide the true twist that results from the aerodynamic forces. In the steady wind speed environment, a clear difference is observed. Although the mean value between the two blade designs are rather small (approximately 0.4°) the BTC design show higher amplitudes in the oscillations related to the azimuth positions than the original blade design presents. This is explained with the higher BTC in the optimized design compared to the original blade design such that the flapwise bending of the blade twists the blade more compared to the non-modified blade. Recall that an initial twist response under flapwise bending was observed in the original blade design c.f. section **??**. The turbulent wind environment presents similar signals where the higher coupling induce higher oscillations and a lower mean twist value.

It is evident from the above observation, that the high reduction in flapwise bending stiffness severely increases the blade tip deflections. BTC can therefore not be introduced without also securing a minimum of the bending stiffness remain, which can either be done adding more material or changing material to higher stiffness materials.

6.2.2 Steady state with stepped wind speed

A quick estimation of the wind turbine's performance with the BTC blade is done with a stepped wind profile. The wind speed in a steady state environment is increased gradually with steps of 1m/s from cut in wind speed of 4m/s to cut out wind speed of 25m/s. The entire operational wind region is thus covered where the blade will experience different wind speeds, pitch settings and generator shaft speeds. The results can be used as a validation that the turbine control system effectively keeps the generator shaft rotational speed at an optimum and below harmful values as well as the effectiveness of the pitch system. Furthermore, instabilities, either due to blade or control systems, may show here.

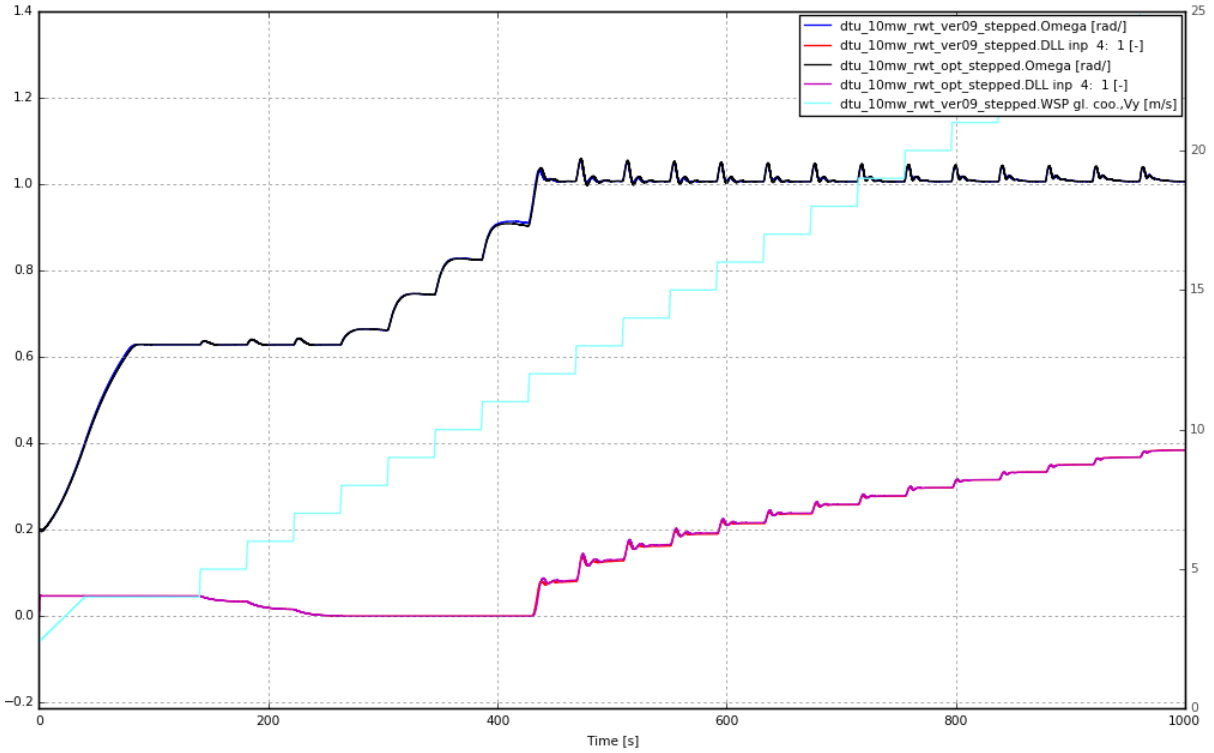

Figure 6.3: *A stepped wind profile from 4-25m/s with steps of 1. The right hand y-axis is the wind speed in m/s while the left hand side y-axis is for the rotational speed of the shaft in rad/s and the pitch of the blade in rad for both optimized and original blade designs.*

Figure 6.3 presents the stepped wind speed simulation performed with one the optimized BTC blade and the original one. From the coinciding lines of the generator shaft rotational speed (blue-original blade and black-optimized blade), it can be concluded that no significant changes occur and it can be inferred that the wind turbine presents equal power output. The BTC in the optimized blade is a small value larger than the original blade, thus its effect on the wind turbine performance can be assumed minor as well. As with the shaft rotational speed, the pitch angle (red-original blade and purple-optimized blade) show a high similarity.
Based in the stepped wind profile plot, it is concluded that no instabilities in either control system or blades are expected for a full turbulent DLC1.3 simulation for the fatigue damage estimation in the next section.

A note to the above must be given. Without a modal analysis of the blade and the wind turbine, possible resonance or instability issues cannot be predicted, however, with the stepped wind profile result, they are not predicted with some confidence.

6.3 Comparison of fatigue damage

The fatigue damage is evaluated from a large amount of simulations. Following the IEC 61400-1 (Ed. 3) standard, a Class 1A (the DTU10MW wind turbine belongs to this class which is the most extreme for offshore turbines), turbines must undergo numerous aero-servo-elastic time simulations in different operational settings and wind environments to be certified. To cover all the different load cases the standard specifies is out of the scope of this thesis, however, an important DLC is the DLC 1.2 which is used to evaluate the fatigue load damage. The

standard specifies that the wind turbine must be simulated in a normal turbulent environment i.e. NTM with three different yaw settings, [10°/0°/-10°], and through the operational mean wind speeds with steps of 2m/s: [4:2:26]m/s and using 2 seeds per mean wind speed. It is assumed that the wind turbine operates at an yaw angle of 0° 50% of the time while the remaining two yaw settings is 25% each. Based on the above, 72 simulations were needed for each blade design which could not be accomplished in this thesis work.

Based on the 72 simulations, the blades life time equivalent load for the root bending moment could be compared and the load mitigation effects visible by a lower value for the BTC blade compared to the same value from the original blade design.

CHAPTER 7

Future work

The work done in this thesis is but a small step down the path. This project has been confronted with issues that, unfortunately, could not be solved which is therefore left for future work. The possibilities and aspects of optimum wind turbine blade design results in a vast amount of topics that could have been handled if unlimited time was provided. Since it is not, some of these topics are presented here.

- Discrepancies between the internal forces and moments was found in section 2.6. The recovered forces and moments, based on the distributed loads, showed flapwise bending moments approximately half compared to the table values extracted from the DTU10MW reference wind turbine report[3]. The reason for this have not been located and is thus left for future work. One could argue whether they even are comparable, since one is obtained by using HAWC2 simulations with aerodynamic loads and the other from a simplified distributed load applied to a beam model. The forces from [3] relates to elastic axis and as do the forces in FRANS. It seems, that in the conversion from internal forces to external forces, too much information is lost. This is most likely not an unknown problem, however, more time is needed to investigate this.

- Validation of sensitivities with a 3rd party sensitivity validation tools must be performed. This could be performed with the in-build sensitivity validation check in IPOPT and *fmincon* which has been utilized early in the beginning of the project, but not followed through to the end. Furthermore, the sensitivities of the responses for the full blade optimization framework must be validated, since this was only done in a structured way for the simplified validation case concerning a composite beam.

- The build framework contains two algorithms for the optimization where it was found that the SQP outperformed IPPOT. This was unexpected, as IPOPT is generally perceived as a fast and robust solver. This issue could not be solved given, and thus it is left for future work.

- A fatigue analysis of the optimized WTB and the original WTB design could illustrate the load mitigation effects in the form of a reduced life time equivalent load for the flapwise root bending moment.

- The optimized blade twist response showed to be less than expected based on findings in literature. A FE-analysis of the optimized design in a more detailed environment such as Abaqus is proposed. This will also allow for buckling analysis which is currently not possible in the the BECAS software.

- To obtain more realistic layups, it is proposed to implement discrete material optimization scheme which will allow for discrete design variable in the form of standard off-the-shelf fiber angles as they are currently produced in the industry.

- A modal analysis to verify the structural integrity of the optimized blade. This will reveal important limitations to the amount of coupling possible due to instabilities and change in mode damping. Research on this exists e.g. [60], which could be implemented in the framework as additional constraints to the eigenfrequencies.
- Improved meshes and a convergence study is needed for any FE results to be completely validated. One of the improvements to the framework is a better mesh software that allow for more control of the cross section elements and their connections.

CHAPTER 8

Conclusion

The purpose of this thesis was to obtain an optimum design of the DTU 10MW reference wind turbine blade (WTB) designed for bend-twist coupling (BTC) effects and validate the load mitigation effects with the aeroelastic simulation tool HAWC2. In this work, the gradient numerical solvers SQP and IPOPT was used to obtain the optimum design with careful selected constraints to ensure the structural integrity of the WTB. More specifically, the tip deflection, tip twist, eigenfrequencies, and material stress limits was used as in-equality constraints in the optimization scheme while both tip deflection, tip twist, and the BTC factor was tested as objectives. The optimization framework was implemented together with BECAS and FRANS which in combination takes any cross section geometries with anisotropic materials oriented in arbitrary orientations and builds a FE beam model where deflections can be estimated given predefined loads. BECAS can, based on given internal loads, calculate the cross section element stresses which is then used with relevant material failure criteria.

An applicable analytic theory was sought in literature, that could predict the twist response of a composite beam under simple point loads. Many beam formulations was found, however, one particular by Chandra et al.[15] was presented together with analytic results, thus making it easy to compare beam response. Using this, a simple beam was analyzed analytically and numerically using BECAS and the results compared to each other as well as to the findings in literature with good agreements.
With the purpose of obtaining an optimum design of the WTB, a framework, with basis in BECAS, was build to perform the material optimization using the algorithms SQP and IPOPT. Sensitivity analysis of the considered objective and constraint functions was performed, implemented and validated against self build central finite difference numerical gradients.

To validate the frameworks capabilities and to gain knowledge on the performance and robustness of the two algorithms, four optimization problem formulations was made with different objectives: (**a**) minimization of compliance (**b**) minimization of tip flapwise deflection, (**c**) maximization of tip twist to flapwise loading (**d**) maximization of BTC effects towards feather. Comparing the performance from two different starting points and considering the structural integrity constraints of eigenfrequencies, deflection or twist and material failure indexes in the form of Max Strain, Max Stress and Tsai-Wu, it could be concluded that SQP generally performed better that IPOPT, both regarding converging to the global optimum as well as in number of function evaluations as a measure of computational time. However, signs of issues with the framework was located and discussed.

With the sensitivities, framework, algorithms, and problem formulation tested considering a simple sandwich cantilever beam, everything was in place for the full blade optimization. Unfortunately, the full blade optimization proved much more difficult than anticipated and with most of the project time invested in obtaining a robust framework that worked for a simple composite beam, little project time was left for troubleshooting, obtaining and validation an optimal WTB design for BTC effects. Efforts was made with simplified problem formulations

and a optimum blade design was achieved, however, only considering a single constraint. The blade design was exported to HAWC2.

To observe the load mitigation effects of BTC, simulations with the aeroelastic simulation software, HAWC2, was performed. The measured flapwise root bending moments, tip flapwise deflection and tip twist fell in good agreement with known results from literature, although, the BTC effect was much smaller.

Bibliography

[1] Tom Ashwill. Passive Load Control for Large Wind Turbines. In *51st AIAA/ASME/ASCE/AHS/ASC Structures, Structural Dynamics, and Materials Conference 18th AIAA/ASME/AHS Adaptive Structures Conference 12th*, pages 1–12, Albuquerque, New Mexico 87185, 2010. Sandia National Laboratories. URL: http://arc.aiaa.org/doi/abs/10.2514/6.2010-2577, doi:10.2514/6.2010-2577.

[2] Tohid Bagherpour, X.M. Li, D.I. Manolas, and V.A. Riziotis. Modeling of material bend-twist coupling on wind turbine blades. *Composite Structures*, 193(February):237–246, jun 2018. URL: https://linkinghub.elsevier.com/retrieve/pii/S0263822317337170, doi:10.1016/j.compstruct.2018.03.071.

[3] Christian Bak, Frederik Zahle, Robert Bitsche, Anders Yde, Lars Christian Henriksen, Anand Nata, and Morten Hartvig Hansen. Description of the DTU 10 MW Reference Wind Turbine. Technical Report 0092, Wind Energy - Technical University of Denmark, Roskilde, 2013. URL: https://dtu-10mw-rwt.vindenergi.dtu.dk, arXiv:arXiv:1011.1669v3, doi:10.1017/CBO9781107415324.004.

[4] Martin P. Bendsøe and O. (Ole) Sigmund. *Topology optimization : theory, methods, and applications*. Springer, 2003. URL: https://findit.dtu.dk/en/catalog/2395963283.

[5] Peter Berring, Kim Branner, Christian Berggreen, and Henrik W Knudsen. Torsional performance of wind turbine blades - part I: Experimental investigation. In *16th International Conference on Composite Materials, July 8-13 2007, Kyto Japan*, pages 1–10, 2007. URL: http://findit.dtu.dk/en/catalog/2359268971.

[6] J. P. Blasques. *Optimal Design of Laminated Composite Beams*. Phd, Technical University of Denmark, 2011. URL: http://orbit.dtu.dk/en/publications/optimal-design-of-laminated-composite-beams(26a24435-6bad-4816-8835-3228348e0a3f).html.

[7] José Pedro Blasques and Mathias Stolpe. Maximum stiffness and minimum weight optimization of laminated composite beams using continuous fiber angles. *Structural and Multidisciplinary Optimization*, 43(4):573–588, 2011. doi:10.1007/s00158-010-0592-9.

[8] J.P. Blasques and R.D. Bitsche. User ' s manual for BECAS - A cross section analysis tool for anisotropic and inhomogeneous beam sections of arbitrary geometry. Technical report, Wind Energy - DTU, 2015. URL: www.becas.dtu.dk, doi:1558407.

[9] C. L. Bottasso, F. Campagnolo, A. Croce, S. Dilli, F. Gualdoni, and M. B. Nielsen. Structural optimization of wind turbine rotor blades by multilevel sectional/multibody/3D-FEM analysis. *Multibody System Dynamics*, 32(1):87–116, jun 2014. URL: http://link.springer.com/10.1007/s11044-013-9394-3, doi:10.1007/s11044-013-9394-3.

[10] C.L. Bottasso, F. Campagnolo, A. Croce, and C. Tibaldi. Optimization-based study of bend-twist coupled rotor blades for passive and integrated passive/active load alleviation. *Wind Energy*, 17(April 2013):n/a–n/a, aug

2012. URL: http://onlinelibrary.wiley.com/doi/10.1002/we.1608/fullhttp://doi.wiley.com/10.1002/we.1543, arXiv:arXiv:1006.4405v1, doi:10.1002/we.1543.

[11] Povl Brøndsted and Rogier P. L. Nijssen. *Advances in wind turbine blade design and materials*. Woodhead Publishing Limited, Philidelphia, 2013. URL: http://www.sciencedirect.com/science/book/9780857094261, doi:10.1533/9780857097286.

[12] Michael Bruyneel and Pierre Duysinx. Note on singular optima in laminate design problems. *Structural and Multidisciplinary Optimization*, 31(2):156–159, feb 2006. URL: http://link.springer.com/10.1007/s00158-005-0569-2, doi:10.1007/s00158-005-0569-2.

[13] Christian Carstensen. *Large scale structural topology optimization of wind turbine blades with eigenfrequency constraints*. Msc, Technical University of Denmark, 2017. URL: http://findit.dtu.dk/en/catalog/2355769010.

[14] Ramesh Chandra and Inderjit Chopra. Structural response of composite beams and blades with elastic couplings. *Composites Engineering*, 2(5-7):347–374, 1992. doi:10.1016/0961-9526(92)90032-2.

[15] Ramesh Chandra, Alan D. Stemple, and Inderjit Chopra. Thin-walled composite beams under bending, torsional, and extensional loads. *Journal of Aircraft*, 27(7):619–626, jul 1990. URL: http://arc.aiaa.org/doi/10.2514/3.25331, arXiv:arXiv:1011.1669v3, doi:10.2514/3.25331.

[16] Fu-Kuo Chang, Richard A. Scott, and George S. Springer. Failure Strength of Nonlinearly Elastic Composite Laminates Containing a Pin Loaded Hole. *Journal of Composite Materials*, 18(5):464–477, sep 1984. URL: http://journals.sagepub.com/doi/10.1177/002199838401800506, doi:10.1177/002199838401800506.

[17] K Chaviaropoulos. Similarity rules for W/T up-scaling. Technical Report April, Centre for Renewable Energy Sources (CRES), Greece, 2007.

[18] G. D. Cheng and X. Guo. Epsilon-relaxed approach in structural topology optimization. *Structural Optimization*, 13(4):258–266, 1997. URL: http://link.springer.com/10.1007/BF01197454, doi:10.1007/BF01197454.

[19] V. H. Cortínez and M. T. Piovan. Vibration and Buckling of Composite Thin-Walled Beams With Shear Deformability. *Journal of Sound and Vibration*, 258(4):701–723, 2002. URL: http://linkinghub.elsevier.com/retrieve/pii/S0022460X02951461, doi:10.1006/jsvi.2002.5146.

[20] Philippe Jacques Couturier. *Structural modelling of composite beams with application to wind turbine rotor blades*. Phd, Technical University of Denmark, 2016. URL: http://findit.dtu.dk/en/catalog/2304732197.

[21] Danish Technical University. The DTU 10MW Reference Wind Turbine Project Site. URL: http://dtu-10mw-rwt.vindenergi.dtu.dk/.

[22] DiabGroup. Technical Data Divinycell H, 2018. URL: http://www.diabgroup.com/en-GB/Products-and-services/Core-Material/Divinycell-H.

[23] Antariksh Dicholkar. *Numerical and Experimental Investigations of bend-twist coupling effects for a small wind turbine blade*. Msc, Technical University of Denmark, 2017. URL: http://findit.dtu.dk/en/catalog/2385162036.

[24] DTU/Wind Energy. The BECAS software package - BECAS, 2016. URL: http://www.becas.dtu.dk/software.

[25] P. Duysinx and O. Sigmund. New developments in handling stress constraints in optimal material distribution. In *7th AIAA/USAF/NASA/ISSMO Symposium on Multidisciplinary Analysis and Optimization*, Reston, Virigina, sep 1998. American Institute of Aeronautics and Astronautics. URL: http://arc.aiaa.org/doi/10.2514/6.1998-4906, doi:10.2514/6.1998-4906.

[26] V. Fedorov and C. Berggreen. Bend-twist coupling potential of wind turbine blades. *Journal of Physics: Conference Series*, 524(1), 2014. doi:10.1088/1742-6596/524/1/012035.

[27] Vladimir Fedorov. *Bend-Twist Coupling Effects in Wind Turbine Blades*. Phd, Technical University of Denmark, 2012. URL: http://findit.dtu.dk/en/catalog/2389471291, arXiv:arXiv:1006.4405v1, doi:10.1002/we.

[28] Christophe Geuzaine and Jean-François Remacle. Gmsh: A 3-D finite element mesh generator with built-in pre- and post-processing facilities. *International Journal for Numerical Methods in Engineering*, 79(11):1309–1331, sep 2009. URL: http://doi.wiley.com/10.1002/nme.2579, doi:10.1002/nme.2579.

[29] V. Giavotto, M. Borri, P. Mantegazza, G. Ghiringhelli, V. Carmaschi, G.C. Maffioli, and F. Mussi. Anisotropic beam theory and applications. *Computers & Structures*, 16(1-4):403–413, 1983. URL: http://www.sciencedirect.com/science/article/pii/0045794983901797, doi:10.1016/0045-7949(83)90179-7.

[30] Zvi Hashin. Fatigue failure criteria for combined cyclic stress. *International Journal of Fracture*, 17(2):101–109, apr 1981. URL: http://link.springer.com/10.1007/BF00053514, doi:10.1007/BF00053514.

[31] Erik Holmberg, Bo Torstenfelt, and Anders Klarbring. Stress constrained topology optimization. *Structural and Multidisciplinary Optimization*, 48(1):33–47, 2013. doi:10.1007/s00158-012-0880-7.

[32] Chang-Ho Hong and Inderjit Chopra. Aeroelastic Stability Analysis of a Composite Rotor Blade. *Journal of the American Helicopter Society*, 30(2):57–67, apr 1985. URL: http://openurl.ingenta.com/content/xref?genre=article{&}issn=2161-6027{&}volume=30{&}issue=2{&}spage=57, doi:10.4050/JAHS.30.57.

[33] InverseProblem. OPTI Toolbox, 2018. URL: https://www.inverseproblem.co.nz/OPTI/index.php.

[34] Robert M. (Robert Millard) Jones. *Mechanics of composite materials*. Taylor & Francis, 2 edition, 1999. URL: http://findit.dtu.dk/en/catalog/2304901972.

[35] N.M. Karaolis, G. Jeronimidis, and PJ Mussgrove. Composite wind turbine blades: coupling effects and rotor aerodynamic performance. In *EWEC '89. European Wind Energy Conference and Exhibition*, volume 89, pages 244–248. Peregrinus, Peter, 1989. URL: http://findit.dtu.dk/en/catalog/2301951801.

[36] Christos Kassapoglou. *Design and Analysis of Composite Structures*. John Wiley & Sons, Ltd, 2010. URL: http://scholar.google.com/scholar?hl=en{&}btnG=Search{&}q=intitle:DESIGN+AND+ANALYSIS+OF+COMPOSITE+STRUCTURES{#}0, doi:10.1002/9780470972700.

[37] H. J. T. Kooijman. Bending-Torsion Coupling of a Wind Turbine Rotor Blade. Technical report, ECN, 1996. URL: ftp://ftp.ecn.nl/pub/www/library/report/1996/i96060.pdf.

[38] T. J. Larsen and A. M. Hansen. *How 2 HAWC2, the user's manual*. RISØ âĂŞ National Laboratory for Sustainable Energy Technical University of Denmark, Risø, 4-6 (en) edition, 2015. URL: www.hawc2.dk.

[39] Chau Le, Julian Norato, Tyler Bruns, Christopher Ha, and Daniel Tortorelli. Stress-based topology optimization for continua. *Structural and Multidisciplinary Optimization*, 41(4):605–620, apr 2010. URL: http://link.springer.com/10.1007/s00158-009-0440-y, doi:10.1007/s00158-009-0440-y.

[40] Huei-Jeng Lin and Wei-Ming Lai. A Study of Elastic Coupling to the Wind Turbine Blade by Combined Analytical and Finite Element Beam Model. *Journal of Composite Materials*, 44(23):2643–2665, nov 2010. URL: http://journals.sagepub.com/doi/10.1177/0021998310369578, doi:10.1177/0021998310369578.

[41] Don W. Lobitz and Paul S. Veers. Aeroelastic behavior of twist-coupled hawt blades. In *AIAA/ASME Wind Energy Symposium, 1998*, pages 75–83. American Institute of Aeronautics and Astronautics Inc, AIAA, 1998. URL: http://findit.dtu.dk/en/catalog/2342846114.

[42] Don W. Lobitz and Paul S. Veers. Load Mitigation with Bending/Twist-coupled Blades on Rotors using Modern Control Strategies. *Wind Energy*, 6(2):105–117, apr 2003. URL: http://doi.wiley.com/10.1002/we.74, doi:10.1002/we.74.

[43] D.W. Lobitz and P.S. Veers. Aeroelastic behavior of twist-coupled HAWT blades. *ASME/AIAA Wind Energy Symposium, Reno, NV*, pages 75–83, 1998. URL: http://www.mech.utah.edu/senior{_}design/05/uploads/WindTurbine/twist{_}couple1.pdf, doi:10.2514/6.1998-29.

[44] James F Manwell, Jon G McGowan, and Anthony L Rogers. *Wind energy explained: theory, design and application*. John Wiley & Sons Ltd., 2nd edition, 2009. doi:10.1002/9781119994367.

[45] Malcolm Mcgugan, Wieslaw Ostachowicz, Jens-Uwe Schröder-Hinrichs, and Marcin Luczak. *MARE-WINT: MAterials and REliability in offshore WINd Turbines technology*. Springer International Publishing, Cham, 2016. URL: http://link.springer.com/10.1007/978-3-319-39095-6, doi:10.1007/978-3-319-39095-6.

[46] MHI Vestas. MHI Vestas Receives Type Certificate for V164-9.5 MW, 2018. URL: http://www.mhivestasoffshore.com/mhi-vestas-receives-final-certification-for-9-5mw/.

[47] V. Middleton, P. Fitches, G. Jeronimidis, J. Feuchtwang, and S. J. R. Powles. Passive blade pitching for overspeed control of an HAWT. In S. Powles, editor, *Wind Energy. Proceedings of the 1998 Twentieth Bwea Wind Energy Conference*, pages 103–17. Professional Engineering Pub, 1998. URL: http://findit.dtu.dk/en/catalog/2383303270.

[48] R. P. L. (Delft University of Technology Faculty of Aerospace Engineering) Nijssen, M. B. (Delft University of Technology Wind Energy) Zaaijer, W. A. A. M. (Delft University of Technology Wind Energy) Bierbooms, G. A. M. (Delft University of Technology

Wind Energy) van Kuik, D. R. V. (Delft University of Technology Stevin II Laboratory / WMC Group) Delft, and Th. (Delft University of Technology Faculty of Aerospace Engineering) van Holten. The application of scaling rules in up-scaling and marinisation of a wind turbine. In *European Wind Energy Conference and Exhibition*, number July, pages 3–6, Copenhagen, 2001.

[49] Jorge Nocedal and Stephen J Wright. *Numerical Optimization*. Springer, New York, USA, second edi edition, 2006. URL: http://esc-web.lib.cbs.dk/login?url=http://dx.doi.org/10.1007/978-0-387-40065-5, arXiv:NIHMS150003, doi:10.1007/978-0-387-40065-5.

[50] Cheng-Huat Ong and Stephen W Tsai. Design, Manufacture and Testing of A Bend-Twist D-Spar. Technical Report c, Sandia National Laboratories (SNL), Albuquerque, NM, and Livermore, CA, jun 1999. URL: http://www.osti.gov/servlets/purl/9461-TuU6fW/webviewable/, doi:10.2172/9461.

[51] Stephen W. Ong, Cheng-huat and Tsai. The Use of Carbon Fibers in Wind Turbine Blade Design : a SERI-8 BLADE EXAMPLE. *SAND 2000-0478*, pages 1–74, 2000. URL: http://findit.dtu.dk/en/catalog/2287180089, doi:10.2172/752054.

[52] P. Pedersen. On optimal orientation of orthotropic materials. *Structural Optimization*, 1(2):101–106, jun 1989. URL: http://link.springer.com/10.1007/BF01637666, doi:10.1007/BF01637666.

[53] P. Pedersen. On thickness and orientational design with orthotropic materials. *Structural Optimization*, 3(2):69–78, jun 1991. URL: http://link.springer.com/10.1007/BF01743275, doi:10.1007/BF01743275.

[54] J T Petersen, H a Madsen, a Bjorck, P Enevoldsen, S Oye, H Ganander, and Et Al. Prediction of Dynamic Loads and Induced Vibrations in Stall. *RISO report, RISOE-R-1045(EN)*, (0), 1988.

[55] J N Reddy and J N Reddy. *Mechanics of laminated composite plates and shells : theory and analysis*. CRC Press, 2004. URL: http://findit.dtu.dk/en/catalog/2304902382.

[56] A. P. Seyranian, E. Lund, and N. Olhoff. Multiple eigenvalues in structural optimization problems. *Structural Optimization*, 8(4):207–227, dec 1994. URL: http://link.springer.com/10.1007/BF01742705, doi:10.1007/BF01742705.

[57] MAHMOOD M. SHOKRIEH and LARRY B. LESSARD. Progressive Fatigue Damage Modeling of Composite Materials, Part I: Modeling. *Journal of Composite Materials*, 34(13):1056–1080, jan 2000. URL: http://techpub.metapress.com/link.asp?target=contribution{&}id=NCNXDXP1JT6AE49E, doi:10.1106/NCNX-DXP1-JT6A-E49E.

[58] Siemens Gamesa. Siemens Gamesa SWT-8.0-154, 2016. URL: https://www.siemens.com/content/dam/internet/siemens-com/global/market-specific-solutions/wind/data{_}sheets/swt-8.0-154-data-sheet-wind-turbine.pdf.

[59] Alexander Stäblein and Morten Hartvig Hansen. Timoshenko beam element with anisotropic cross-sectional properties. *Proceedings of VII European Congress on Computational Methods in Applied Sciences and Engineering*, (June):5–10, 2016. doi:10.7712/100016.2377.9780.

[60] Alexander R. Stäblein, Morten H. Hansen, and Georg Pirrung. Fundamental aeroelastic properties of a bendâĂŞtwist coupled blade section. *Journal of Fluids and Structures*, 68:72–89, jan 2017. URL: http://linkinghub.elsevier.com/retrieve/pii/S0889974616303553, doi:10.1016/j.jfluidstructs.2016.10.010.

[61] J. Stegmann and Erik Lund. Discrete material optimization of general composite shell structures. *International Journal for Numerical Methods in Engineering*, 62(14):2009–2027, apr 2005. URL: http://doi.wiley.com/10.1002/nme.1259, doi:10.1002/nme.1259.

[62] Alan D. Stemple and Sung W. Lee. Finite-Element Model for Composite Beams with Arbitrary Cross-Sectional Warping. *AIAA Journal*, 26(12):1512–1520, dec 1988. URL: http://arc.aiaa.org/doi/10.2514/3.48797, doi:10.2514/3.48797.

[63] Bengt. Sundström. *Handbook of solid mechanics*. Department of Solid Mechanics, KTH, 2010. URL: http://findit.dtu.dk/en/catalog/2304902322.

[64] G. Sved and Z. Ginos. Structural optimization under multiple loading. *International Journal of Mechanical Sciences*, 10(10):803–805, oct 1968. URL: http://linkinghub.elsevier.com/retrieve/pii/0020740368900210, doi:10.1016/0020-7403(68)90021-0.

[65] S.P. Timoshenko. LXVI. On the correction for shear of the differential equation for transverse vibrations of prismatic bars. *The London, Edinburgh, and Dublin Philosophical Magazine and Journal of Science*, 41(245):744–746, may 1921. URL: https://www.tandfonline.com/doi/full/10.1080/14786442108636264, doi:10.1080/14786442108636264.

[66] Stephen W. (U.S. Air Force Materials Laboratory) Tsai and Thomas H. (Washington University) Hahn. *Introduction to Composite Materials Science*. Technomic Publishing Company, Westport, Connecticut, 1980. URL: http://findit.dtu.dk/en/catalog/2299725768.

[67] Alexander Verbart, Matthijs Langelaar, and Fred van Keulen. A unified aggregation and relaxation approach for stress-constrained topology optimization. *Structural and Multidisciplinary Optimization*, 55(2):663–679, feb 2017. URL: http://link.springer.com/10.1007/s00158-016-1524-0, doi:10.1007/s00158-016-1524-0.

[68] V.V. Volovoi, D.H. Hodges, C.E.S. Cesnik, and B. Popescu. Assessment of beam modeling methods for rotor blade applications. *Mathematical and Computer Modelling*, 33(10-11):1099–1112, may 2001. URL: http://linkinghub.elsevier.com/retrieve/pii/S0895717700003022, doi:10.1016/S0895-7177(00)00302-2.

[69] Andreas Wächter and Lorenz T Biegler. On the Implementation of an Interior Point Filter Line Search Algorithm for Large-Scale Nonlinear Programming. *Mathematical Programming*, 106(1):25–57, 2005. URL: http://findit.dtu.dk/en/catalog/2262849010.

[70] S. E. S. E. Yamada and C. T. Sun. Analysis of laminate strength and its distribution. *Composites*, 12:275–284, jul 1978. URL: http://findit.dtu.dk/en/catalog/2367896316.

[71] Frederik Zahle, Carlo Tibaldi, Christian Pavese, Michael K. McWilliam, Jose P. A. A. Blasques, and Morten H. Hansen. Design of an Aeroelastically Tailored 10 MW Wind Turbine Rotor. *Journal of Physics: Conference Series*, 753(6):1–11, sep 2016. URL: http://stacks.iop.org/1742-6596/753/i=6/a=062008?key=crossref.aad3ea790a3b9c7cdc9876565a9b1cd0, doi:10.1088/1742-6596/753/6/062008.

[72] Dan Zenkert and Mark Battley. *Foundations of fibre composites : notes for the course: Composite lightweight structures*. DTU - Technical University of Denmark. Department of Mechanical Engineering DTU Mekanik, Kgs. Lyngby, 2nd edition, 2006. URL: http://findit.dtu.dk/en/catalog/2304902175.

[73] Dan Zenkert and Mark Battley. Foundations of Fibre Composites, Laminate and Sandwhich Structures, 2009.

CHAPTER A

Appendix

A.1 Airfoil sketch with relative angles

Below is a sketch of an airfoil from a WTB with the relative angles and force vectors defined.

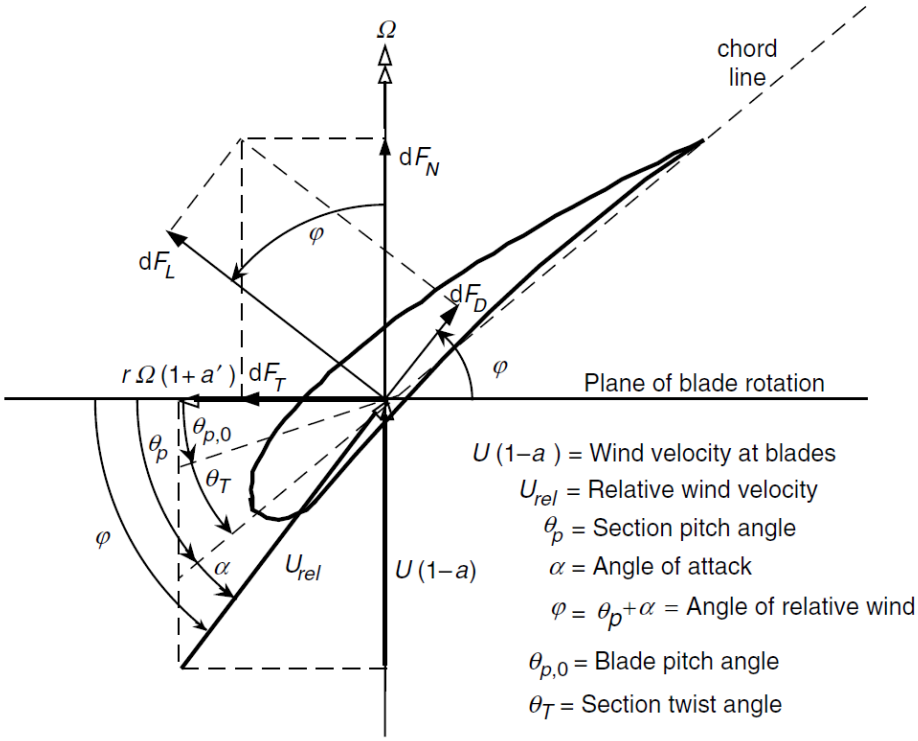

Figure A.1: *Definition of airfoil relative angles, taken from[44]*

A.2 Transformation matrix

Standard rotation matrix for transforming strains and stresses.

$$\mathbf{T} = \begin{bmatrix} \cos(x) & 0 & -\sin(x) \\ 0 & 1 & 0 \\ \sin(x) & 0 & \cos(x) \end{bmatrix} \tag{A.1}$$

A.3 Analytic beam slope and twist by Chandra et al.

This section presents the analytic method presented by Chandra et al. [15] to estimate a clamped thin walled composite beam's bending slope and twist rate when subjected to a point

load at the free end. The method presented here, builds on the coupled nonlinear analysis of Hong and Chopra [32] which results in a simplified linear analysis that estimates bending slope and twist rate for thin walled symmetric composite beams. In this simplified version, the transverse shear effects are neglected. The reduced stiffness matrix is presented as:

$$\begin{bmatrix} M \\ T \end{bmatrix} = \begin{bmatrix} EI & K_p \\ K_p & GJ \end{bmatrix} \begin{bmatrix} w'' \\ \phi' \end{bmatrix} \tag{A.2}$$

where w'' is the bending curvature and ϕ' is the twist derivative. The terms in the reduced stiffness matrix are defined with CLT:

$$EI = \sum_{k=1}^{N} \int\int_{1,2} (\bar{C}_{11})_k \zeta^2 d\eta d\zeta + \sum_{l=1}^{M} \int\int_{3,4} (\bar{C}_{11})_l \zeta^2 d\eta d\zeta \tag{A.3}$$

$$GJ = \sum_{k=1}^{N} \int\int_{1,2} (\bar{C}_{66})_k \zeta^2 d\eta d\zeta + \sum_{l=1} \int\int_{3,4} (\bar{C}_{66})_l \eta^2 d\eta d\zeta \tag{A.4}$$

$$K_p = \sum_{k=1}^{N} \int\int_{1,2} (\bar{C}_{16})_k \hat{\zeta} \zeta d\eta d\zeta \tag{A.5}$$

1,2 represents top and bottom laminates of box beam; 3,4 represents left and right side laminates of box beam. Stiffness terms are defined as:

$$\begin{gathered} \bar{C}_{11} = \bar{Q}_{11} - \bar{Q}_{12}^2/\bar{Q}_{22} \\ \bar{C}_{16} = \bar{Q}_{16} - \bar{Q}_{12} \times \bar{Q}_{26}/\bar{Q}_{22} \\ \bar{C}_{66} = \bar{Q}_{66} - \bar{Q}_{26}^2/\bar{Q}_{22} \end{gathered} \tag{A.6}$$

Where $\bar{Q}$ is the stiffness matrix of the kth lamina in $x-\eta$ or $x-\zeta$ plane. N is the number of layers in the laminate 1 or 2 and M is the number of layers in the laminate 3 or 4. η and ζ are the coordinates in the plane of cross section. Including the warping function λ the coordinates are $\hat{\zeta} = \zeta + \lambda, \eta$ and $\hat{\eta} = \eta - \lambda$. The assumed warping function is $\lambda = \beta\zeta\eta$, where $\beta = (c-d)/(c+d)$ for uniform wall thickness of the cross section. c and d are the width and height of the beam respectively. The definition of the cross section and coordinate system can be observed in figure A.2. The structural response is then estimated with:

$$w_{,x} = \frac{P}{2(EI - K_p^2/GJ)}(2Lx - x^2) \tag{A.7}$$

$$\phi = \frac{K_p/GJ}{2(EI - K_p^2/GJ)} P(2Lx - x^2) \tag{A.8}$$

where P is the point load applied at the free end of the beam through the shear center. L is the length of the beam and x is the span-wise coordinate.

A.3.1 Comparison to findings in literature, the Chandra et al. experiment

Using GMSH the following cross section grid for the validation of Chandra et al.'s experiments is created and presented below in figure A.3.
The obtained cross section stiffness matrix for this mesh and using the material properties and layup presented in section 2.4, is presented below (element placements has been changed to match that of Stäblein et al. [59]).

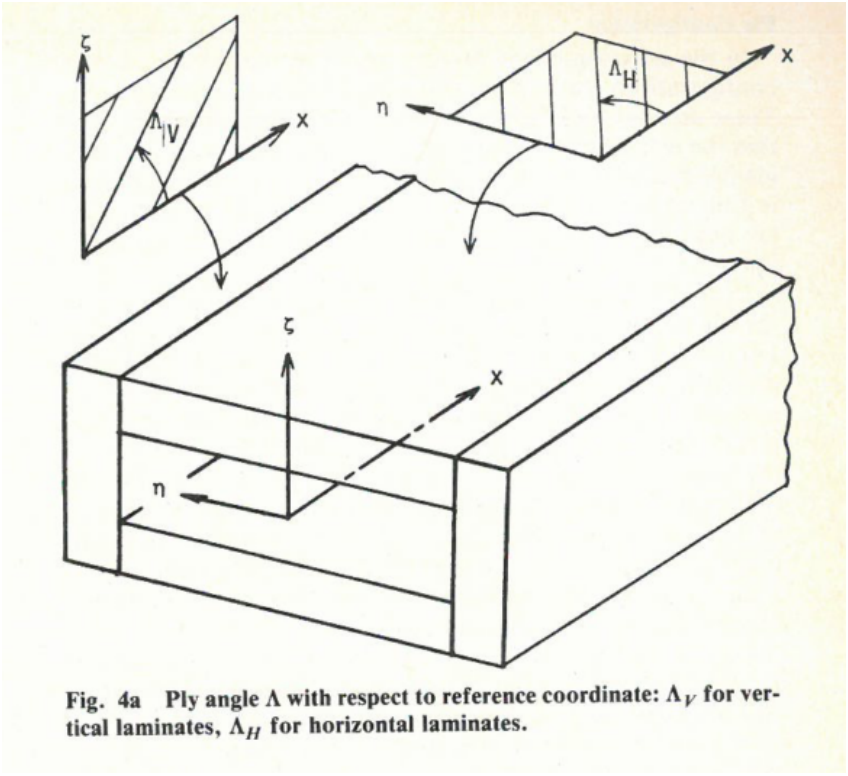

Fig. 4a Ply angle Λ with respect to reference coordinate: Λ_V for vertical laminates, Λ_H for horizontal laminates.

Figure A.2: *The coordinate system definition of the cross section, taken from [32]*

$$\mathbf{K}_{s,present} = \begin{bmatrix} 11.349e5 & 2.8454e5 & -14.501 & 14.322 & 4.5545 & 0 \\ & 4.1670e5 & -19.666 & 15.630 & -2.1972 & 0 \\ & & 3.0710e5 & 0 & 0 & 9.1284 \\ & & & 61.407 & -20.780 & 0 \\ & & & & 34.678 & 0 \\ & & & & & 81.068 \end{bmatrix} \tag{A.9}$$

whereas the cross section stiffness matrix obtained by Stäblein et al. [59] is:

$$K_{s,Stäblain} = \begin{bmatrix} 11.387e5 & 2.909e5 & 0 & -30.458 & 12.674 & 0 \\ & 4.189e5 & 0 & -11.932 & 8.689 & 0 \\ & & 3.122e5 & 0 & 0 & 12.302 \\ & & & 62.962 & -21.741 & 0 \\ & & & & 35.146 & 0 \\ & & & & & 80.594 \end{bmatrix} \tag{A.10}$$

Small difference occurs especially at off diagonal terms and at entries [1,3] and [2,3] St.äblein et al. reports null. Diagonal terms are close with a percentage of difference. The difference might be due differences in number of FE since no convergence study has presently been made to leave this out. There is no mention of how many elements is used in Stäblain et al.'s article. The material properties from different sources are reported below in table A.1. The Frobenius norm of the difference between present stiffness matrix and the one presented by Stäblein et al. is 1.1249e+04 Pa.
The material data used in this study is that of Stäblein et al. by assuming $E_{33} = E_{22}$, $G_{13} = G_{12}$, and $\nu_{13} = \nu_{12}$.

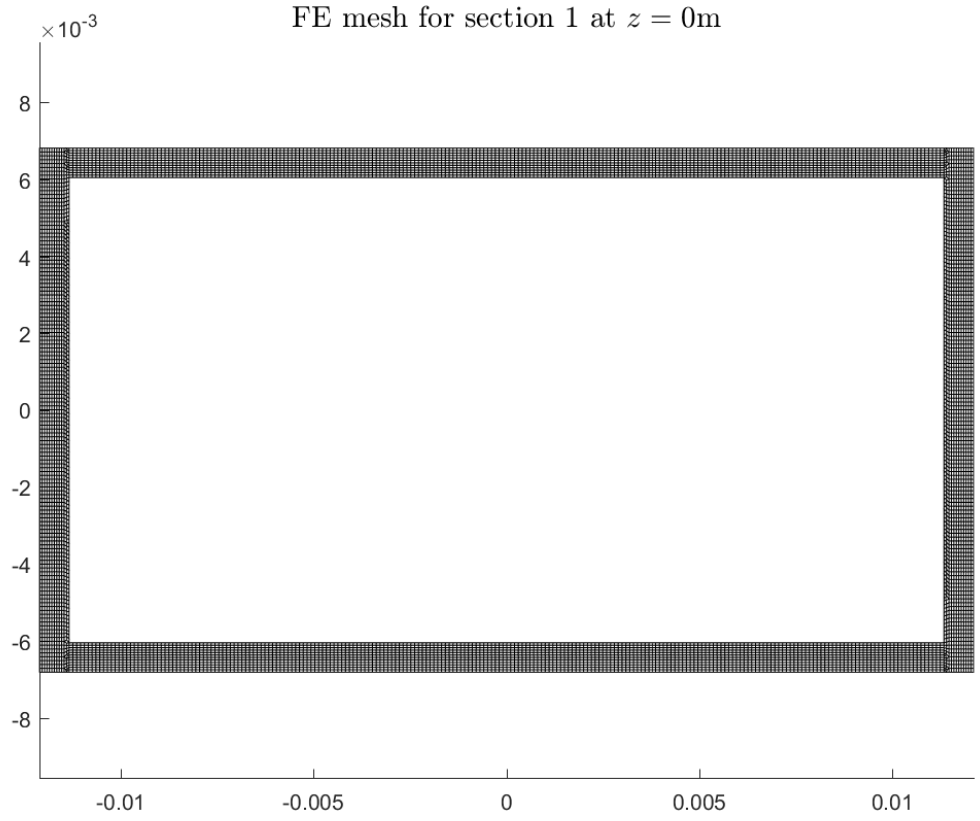

Figure A.3: *Cross section mesh of beam used in Chandra et al. with 8767 Q4 elements*

A.4 GMSH - Example file

An example of a GMSH input.geo file for generation of cross section structured mesh. This example is for a prismatic sandwich beam with two laminae for faces separated with a core in between.

```
lc = 1e-2;
w = .25;
t1 = .025;

Point(1) = {-w/2, -w/2, 0, lc};
Point(2) = {w/2, -w/2, 0, lc};
Point(3) = {w/2, -w/2+t1, 0, lc};
Point(4) = {w/2, w/2-t1, 0, lc};
Point(5) = {w/2, w/2, 0, lc};
Point(6) = {-w/2, w/2, 0, lc};
Point(7) = {-w/2, w/2-t1, 0, lc};
Point(8) = {-w/2, -w/2+t1, 0, lc};

Line(1) = {1,2};
Line(2) = {2,3};
```

Table A.1: *Comparison of material properties from original experiments by Chandra et al. [15], as reported by Stäblein et al.[59], and finally as reported by Couturier [20]*

	E_{11}	E_{22}	E_{33}	G_{12}	G_{23}	G_{13}	ν_{12}	ν_{23}	ν_{13}
Chandra (PSI)	20.59e6	1.42e6		0.89e6			0.42		
Chandra (convert to GPa)	141.96	9.79		6.14			0.42		
Stäblein (GPa)	142	9.81		6.00	3.77		0.30	0.42	
Couturier (GPa)	142.0	9.79	9.79	6.00	4.80	6.00	0.42	0.02	0.42

```
Line(3) = {3,8};
Line(4) = {8,1};

Line(5) = {8,3};
Line(6) = {3,4};
Line(7) = {4,7};
Line(8) = {7,8};

Line(9) = {7,4};
Line(10) = {4,5};
Line(11) = {5,6};
Line(12) = {6,7};

Curve Loop(2) = {1,2,3,4};
Curve Loop(1) = {5,6,7,8};
Curve Loop(3) = {9,10,11,12};

Plane Surface(1) = {1};
Plane Surface(2) = {2};
Plane Surface(3) = {3};

Transfinite Surface(1) = {8,3,4,7};
Transfinite Surface(2) = {1,2,3,8};
Transfinite Surface(3) = {7,4,5,6};

Recombine Surface(1);
Recombine Surface(2);
Recombine Surface(3);

Physical Surface(1) = 1;
Physical Surface(2) = 2;
Physical Surface(3) = 3;
```

A.5 Chain rule - inverse

Assuming symmetric matrix the following is valid:

$$\mathbf{K}\mathbf{K}^{-1} = \mathbf{I} \tag{A.11}$$

of which the partial derivative is

$$\frac{\partial \mathbf{K}}{\partial x}\mathbf{K}^{-1} + \mathbf{K}\frac{\partial \mathbf{K}^{-1}}{\partial x} = 0 \tag{A.12}$$

and isolating for the derivative of the inverse matrix:

$$\frac{\partial \mathbf{K}^{-1}}{\partial x} = -\mathbf{K}^{-1}\frac{\partial \mathbf{K}}{\partial x}\mathbf{K}^{-1} \tag{A.13}$$

A.6 Standard forms

From lecture slides of the course ME46060 - Engineering Optimization - Concepts and Applications 2017.

Positive null form

$$\begin{array}{ll} \underset{\mathbf{x}\in\mathbb{R}}{min} & f(\mathbf{x}) \\ \text{s.t.} & \mathbf{g}(\mathbf{x}) \geq 0 \\ & \mathbf{h}(\mathbf{x}) = 0 \end{array} \tag{A.14}$$

Negative unity form

$$\begin{array}{ll} \underset{\mathbf{x}\in\mathbb{R}}{min} & f(\mathbf{x}) \\ \text{s.t.} & \mathbf{g}(\mathbf{x}) \leq 1 \\ & \mathbf{h}(\mathbf{x}) = 1 \end{array} \tag{A.15}$$

Positive unity form

$$\begin{array}{ll} \underset{\mathbf{x}\in\mathbb{R}}{min} & f(\mathbf{x}) \\ \text{s.t.} & \mathbf{g}(\mathbf{x}) \geq 1 \\ & \mathbf{h}(\mathbf{x}) = 1 \end{array} \tag{A.16}$$

A.7 Hashin failure criteria

The Hashin failure criteria is presented here as implemented in BECAS. It builds on the theory of Hashin[30] and Yamada et al.[70] and adapted by Chang et al.[16]. The version implemented in BECAS is the one adopted by Shokrieh et al.[57].

Fiber tension-compression

$$f_{fiber} = \begin{cases} \sqrt{\left(\sigma_{11}/\bar{\sigma}^t_{11}\right)^2 + \left(\sigma_{12}/\bar{\sigma}_{12}\right)^2 + \left(\sigma_{13}/\bar{\sigma}_{13}\right)^2} & \text{, if} \quad \sigma_{11} > 0 \\ \sqrt{\sigma_{11}/\bar{\sigma}^c_{11}} & \text{, if} \quad \sigma_{11} < 0 \\ 0 & \text{, otherwise} \end{cases} \tag{A.17}$$

Matrix tension-compression

$$f_{matrix} = \begin{cases} \sqrt{\left(\sigma_{22}/\bar{\sigma}^t_{22}\right)^2 + \left(\sigma_{12}/\bar{\sigma}_{12}\right)^2 + \left(\sigma_{23}/\bar{\sigma}_{23}\right)^2} & \text{, if} \quad \sigma_{22} > 0 \\ \sqrt{\left(\sigma_{22}/\bar{\sigma}^c_{22}\right)^2 + \left(\sigma_{12}/\bar{\sigma}_{12}\right)^2 + \left(\sigma_{23}/\bar{\sigma}_{23}\right)^2} & \text{, if} \quad \sigma_{22} < 0 \\ 0 & \text{, otherwise} \end{cases} \tag{A.18}$$

Noraml tension-compression

$$f_{normal} = \begin{cases} \sqrt{\left(\sigma_{33}/\bar{\sigma}^t_{33}\right)^2 + \left(\sigma_{13}/\bar{\sigma}_{13}\right)^2 + \left(\sigma_{23}/\bar{\sigma}_{23}\right)^2} & \text{, if} \quad \sigma_{33} > 0 \\ \sqrt{\left(\sigma_{33}/\bar{\sigma}^c_{33}\right)^2 + \left(\sigma_{13}/\bar{\sigma}_{13}\right)^2 + \left(\sigma_{23}/\bar{\sigma}_{23}\right)^2} & \text{, if} \quad \sigma_{33} < 0 \\ 0 & \text{, otherwise} \end{cases} \tag{A.19}$$

Fiber-matrix shearing

$$f_{fiber-matrix} = \begin{cases} \sqrt{\left(\sigma_{11}/\bar{\sigma}_{11}^{c}\right)^2 + \left(\sigma_{12}/\bar{\sigma}_{12}\right)^2 + \left(\sigma_{13}/\bar{\sigma}_{13}\right)^2} & \text{, if} \quad \sigma_{11} < 0 \\ 0 & \text{, otherwise} \end{cases} \tag{A.20}$$

A.7.1 Hashin gradient

Using the notation $\partial\sigma/\partial x_i = \sigma'$ for abbreviation the following presents the gradient values of the FI using the Hashin failure criteria.

Fiber tension-compression gradient

$$f_{fiber} = \begin{cases} \dfrac{\sigma_{11}\sigma'_{11}}{K_{fiber} * \left(\bar{\sigma}_{11}^{t}\right)^2} + \dfrac{\sigma_{12}\sigma'_{12}}{K_{fiber} * \bar{\sigma}_{12}^2} + \dfrac{\sigma_{13}\sigma'_{13}}{K_{fiber} * \bar{\sigma}_{13}^2} & \text{, if} \quad \sigma_{11} > 0 \\ \dfrac{1}{2}\dfrac{\sigma'_{11}}{\sqrt{\dfrac{\sigma_{11}}{\bar{\sigma}_{11}^{c}} * \bar{\sigma}_{11}^{c}}} & \text{, if} \quad \sigma_{11} < 0 \\ 0 & \text{, otherwise} \end{cases} \tag{A.21}$$

where

$$K_{fiber} = \sqrt{\frac{\sigma_{11}^2}{\left(\bar{\sigma}_{11}^{t}\right)^2} + \frac{\sigma_{12}^2}{\bar{\sigma}_{12}^2} + \frac{\sigma_{13}^2}{\bar{\sigma}_{13}^2}}$$

Matrix tension-compression

$$f_{matrix} = \begin{cases} \dfrac{\sigma_{22}\sigma'_{22}}{K_{matrix}^{t} * \left(\bar{\sigma}_{22}^{t}\right)^2} + \dfrac{\sigma_{12}\sigma'_{12}}{K_{matrix}^{t} * \bar{\sigma}_{12}^2} + \dfrac{\sigma_{23}\sigma'_{23}}{K_{matrix}^{t} * \bar{\sigma}_{23}^2} & \text{, if} \quad \sigma_{22} > 0 \\ \dfrac{\sigma_{22}\sigma'_{22}}{K_{matrix}^{c}\left(\bar{\sigma}_{22}^{c}\right)^2} + \dfrac{\sigma_{12}\sigma'_{12}}{K_{matrix}^{c}\bar{\sigma}_{12}^2} + \dfrac{\sigma_{23}\sigma'_{23}}{K_{matrix}^{c}\bar{\sigma}_{23}^2} & \text{, if} \quad \sigma_{22} < 0 \\ 0 & \text{, otherwise} \end{cases} \tag{A.22}$$

where

$$K_{matrix}^{t} = \sqrt{\frac{\sigma_{22}^2}{\left(\bar{\sigma}_{22}^{t}\right)^2} + \frac{\sigma_{12}^2}{\bar{\sigma}_{12}^2} + \frac{\sigma_{23}^2}{\bar{\sigma}_{23}^2}}$$

$$K_{matrix}^{c} = \sqrt{\frac{\sigma_{22}^2}{\left(\bar{\sigma}_{22}^{c}\right)^2} + \frac{\sigma_{12}^2}{\bar{\sigma}_{12}^2} + \frac{\sigma_{23}^2}{\bar{\sigma}_{23}^2}}$$

Noraml tension-compression

$$f_{normal} = \begin{cases} \dfrac{\sigma_{33}\sigma'_{33}}{K_{normal}^{t} * \left(\bar{\sigma}_{33}^{t}\right)^2} + \dfrac{\sigma_{13}\sigma'_{13}}{K_{normal}^{t} * \bar{\sigma}_{13}^2} + \dfrac{\sigma_{23}\sigma'_{23}}{K_{normal}^{t} * \bar{\sigma}_{23}^2} & \text{, if} \quad \sigma_{33} > 0 \\ \dfrac{\sigma_{33}\sigma'_{33}}{K_{normal}^{c} * \left(\bar{\sigma}_{33}^{c}\right)^2} + \dfrac{\sigma_{13}\sigma'_{13}}{K_{normal}^{c} * \bar{\sigma}_{13}^2} + \dfrac{\sigma_{23}\sigma'_{23}}{K_{normal}^{c} * \bar{\sigma}_{23}^2} & \text{, if} \quad \sigma_{33} < 0 \\ 0 & \text{, otherwise} \end{cases} \tag{A.23}$$

where

$$K^t_{normal} = \sqrt{\frac{\sigma^2_{33}}{\left(\bar{\sigma}^t_{33}\right)^2} + \frac{\sigma^2_{13}}{\bar{\sigma}^2_{13}} + \frac{\sigma^2_{23}}{\bar{\sigma}^2_{23}}}$$

$$K^c_{normal} = \sqrt{\frac{\sigma^2_{33}}{\left(\bar{\sigma}^c_{33}\right)^2} + \frac{\sigma^2_{13}}{\bar{\sigma}^2_{13}} + \frac{\sigma^2_{23}}{\bar{\sigma}^2_{23}}}$$

Fiber-matrix shearing

$$f_{fiber-matrix} = \begin{cases} \dfrac{\sigma_{11}\sigma'_{11}}{K_{fm} * \left(\bar{\sigma}^c_{11}\right)^2} + \dfrac{\sigma_{12}\sigma'_{12}}{K_{fm} * \bar{\sigma}^2_{12}} + \dfrac{\sigma_{13}\sigma'_{13}}{K_{fm} * \bar{\sigma}^2_{13}} & \text{, if} \quad \sigma_{11} < 0 \\ 0 & \text{, otherwise} \end{cases} \tag{A.24}$$

where

$$K_{fm} = \sqrt{\frac{\sigma^2_{11}}{\left(\bar{\sigma}^c_{11}\right)^2} + \frac{\sigma^2_{12}}{\bar{\sigma}^2_{12}} + \frac{\sigma^2_{13}}{\bar{\sigma}^2_{13}}} \tag{A.25}$$

A.7.2 Gradient validation with central finite difference check

The Hashin failure criterion gradients are validated with a central finite difference check and step size is gradually decreased from 1 to small values to see where the minimum truncation and conditional error occurs. The result is presented in figure A.4. It is observed that the Hashin failure criterion gradient error is as low as 1e-8 for a perturbation step size of approximately 1e-3. It can be concluded that the gradient calculation is correct.

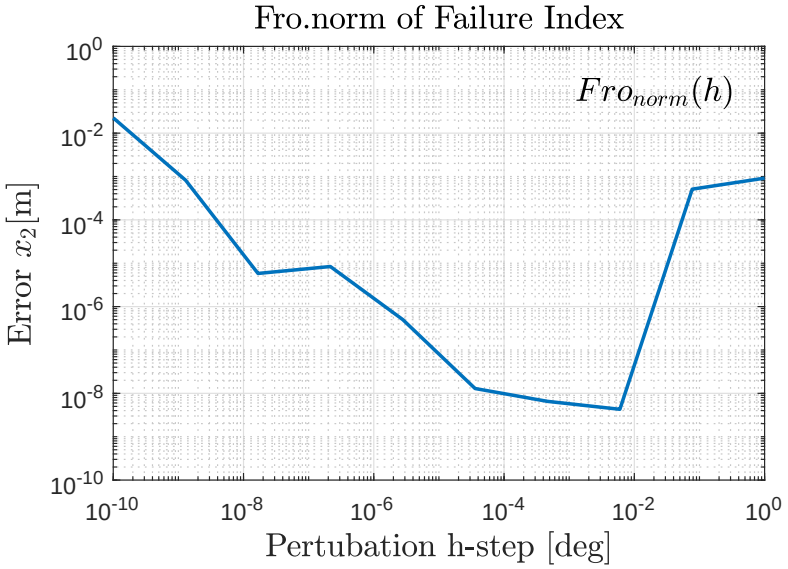

Figure A.4: *Truncation and conditional error of Hashin failure criterion gradient*

A.8 Material rotated constitutive matrix

Here the new implementation of the rotation of the element constitutive matrix (fiber rotation).

The compliance matrix is defined as:

$$\mathbf{Q}_m^{-1} = \mathbf{S}_m = \begin{bmatrix} \frac{1}{E_1} & -\frac{\nu_{12}}{E_1} & \frac{-\nu_{13}}{E_1} & 0 & 0 & 0 \\ \frac{-\nu_{12}}{E_1} & \frac{1}{E_2} & \frac{-\nu_{23}}{E_2} & 0 & 0 & 0 \\ \frac{-\nu_{13}}{E_1} & \frac{-\nu_{23}}{E_2} & \frac{1}{E_3} & 0 & 0 & 0 \\ 0 & 0 & 0 & \frac{1}{G_{23}} & 0 & 0 \\ 0 & 0 & 0 & 0 & \frac{1}{G_{13}} & 0 \\ 0 & 0 & 0 & 0 & 0 & \frac{1}{G_{12}} \end{bmatrix} \tag{A.26}$$

The stiffness matrix is then defined as the inverse of the compliance matrix.

$$\mathbf{Q}_m = \mathbf{S}_m^{-1} \tag{A.27}$$

To rotate the 3D constitutive matrix a 3D rotation matrix is used:

$$\mathbf{R} = \begin{bmatrix} \cos^2 & \sin^2 & 0 & 0 & 0 & 2\cos\sin \\ \sin^2 & \cos^2 & 0 & 0 & 0 & -2\cos\sin \\ 0 & 0 & 1 & 0 & 0 & 0 \\ 0 & 0 & 0 & \cos & \sin & 0 \\ 0 & 0 & 0 & -\sin & \cos & 0 \\ -\cos\sin & \cos\sin & 0 & 0 & 0 & \cos^2 - \sin^2 \end{bmatrix} \tag{A.28}$$

The rotations is then performed as

$$\mathbf{Q}_m^g = \mathbf{R}\mathbf{Q}_m^l\mathbf{R}^T \tag{A.29}$$

A reordering to comply with BECAS coordinate system is performed:

$$\mathbf{R}(edof, edof) = \mathbf{R} \tag{A.30}$$

where:

$$edof = [6\ \ 1\ \ 2\ \ 3\ \ 5\ \ 4] \tag{A.31}$$

resulting in:

$$\mathbf{R}(edof, edof) = \begin{bmatrix} \cos^2 & 0 & 0 & -2\cos\sin & 0 & \sin^2 \\ 0 & 1 & 0 & 0 & 0 & 0 \\ 0 & 0 & \cos & 0 & \sin & 0 \\ \cos\sin & 0 & 0 & \cos^2 - \sin^2 & 0 & -\cos\sin \\ 0 & 0 & -\sin & 0 & \cos & 0 \\ \sin^2 & 0 & 0 & 2\cos\sin & 0 & \cos^2 \end{bmatrix} \tag{A.32}$$

A.9 Full stiffness matrix and nomenclature

The stiffness matrix is provided by BECAS, eq. (2.41) and is presented in full form below:

$$\mathbf{K}_s = \begin{bmatrix} K_{11} & K_{12} & K_{13} & K_{14} & K_{15} & K_{16} \\ & K_{22} & K_{23} & K_{24} & K_{25} & K_{26} \\ & & K_{33} & K_{34} & K_{35} & K_{36} \\ & & symm. & K_{44} & K_{45} & K_{46} \\ & & & & K_{55} & K_{56} \\ & & & & & K_{66} \end{bmatrix} \tag{A.33}$$

Diagonal terms nomenclature:

- K_{11}: Edgewise shear stiffness (in the x-direction)

- K_{22}: Flapwise shear stiffness (in the y-direction)
- K_{33}: Axial stiffness in the z-direction
- K_{44}: Flapwise bending stiffness (around x-axis)
- K_{55}: Edgewise bending stiffness (around y-axis)
- K_{66}: Torsional stiffness (around z-axis)

Off-diagonal nomenclature introducing torsion couplings, from [23]:

- K_{16}: Coupling term for edgewise shear stiffness and torsion
- K_{26}: Coupling term for flapwise shear stiffness and torsion
- K_{36}: Coupling term for axial force and torsion
- K_{46}: Coupling term for flapwise bending and torsion
- K_{56}: Coupling term for edgewise bending and torsion

The rest of the off-diagonal coupling terms can be illustrated with the figure below, taken from lecture slide in the course AE4ASM109 - Design and Analysis of Composite Structures 1:

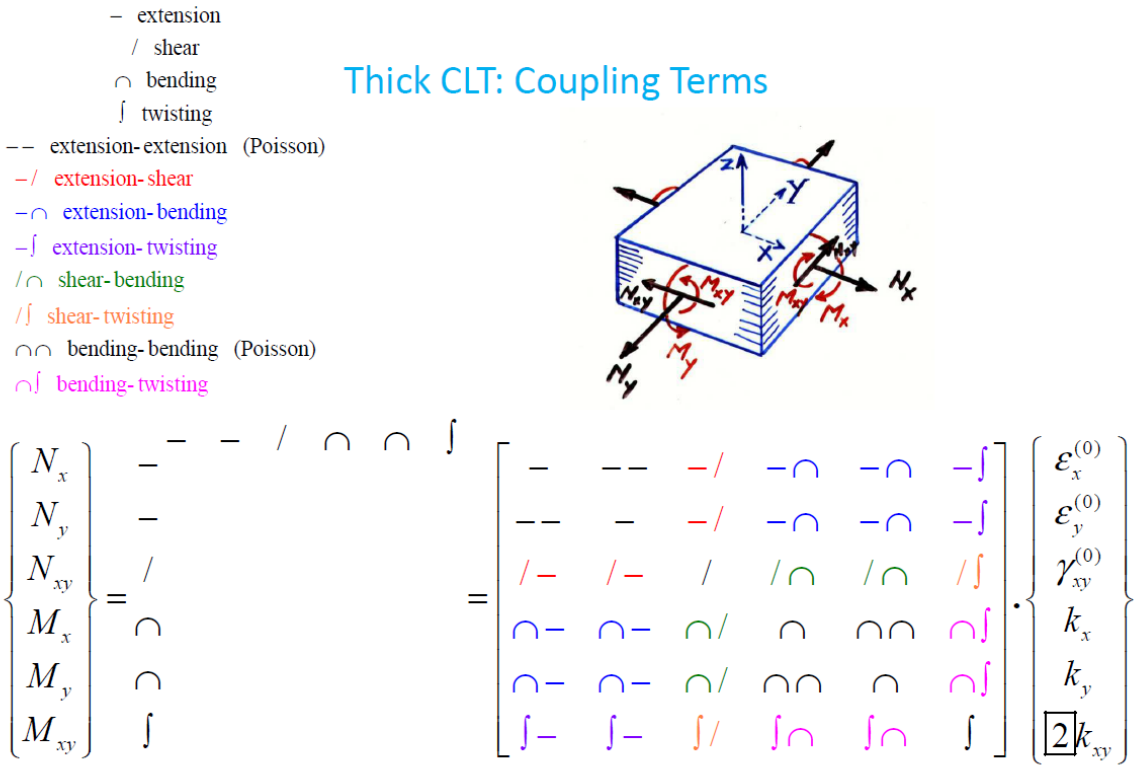

Figure A.5: *Illustration of stiffness terms in laminate constitutive matrix*

A.10 Original blade sub-part layup

Here, the material data for each material used in the DTU10MW reference WTB is presented:

Table A.2: *Material data for each material used in the DTU10MW reference WTB. Note: minthk is the minimum layer thickness of respective material*

name	UNIAX	TRIAX	BIAX	BALSA	PVCFOAM	TE_GLUE
E_{11}[Pa]	4.1630E10	2.1790E10	1.3920E10	5.000E07	7.280E08	2.00E09
E_{22}[Pa]	1.4930E10	1.4670E10	1.3920E10	5.000E07	7.280E08	2.00E09
E_{33}[Pa]	1.3426E10	1.2099E10	1.2099E10	2.730E09	7.280E08	2.00E09
G_{12}[Pa]	5.0470E09	9.4130E09	1.1500E10	1.667E07	2.800E08	7.69E08
G_{13}[Pa]	5.0470E09	4.5386E09	4.5386E09	1.500E08	2.800E08	7.69E08
G_{23}[Pa]	5.0470E09	4.5386E09	4.5386E09	1.500E08	2.800E08	7.69E08
ν_{12}[-]	2.4100E-01	4.7800E-01	5.3300E-01	5.000E-01	3.000E-01	3.00E-01
ν_{13}[-]	2.6750E-01	2.7500E-01	2.7500E-01	1.300E-02	3.000E-01	3.00E-01
ν_{23}[-]	3.3010E-01	3.3290E-01	3.3290E-01	1.300E-02	3.000E-01	3.00E-01
$\bar{\sigma}^t_{11}$[Pa]	3.9644E08	2.1738E08	1.0099E08	4.550E06	6.250E05	5.00E06
$\bar{\sigma}^c_{11}$[Pa]	-2.8317E08	-1.7785E08	-9.4684E07	5.050E06	1.050E06	5.00E06
$\bar{\sigma}^t_{22}$[Pa]	2.5053E07	8.1167E07	9.1537E07	3.500E05	6.250E05	5.00E06
$\bar{\sigma}^c_{22}$[Pa]	-1.0155E08	-1.1974E08	-9.4684E07	2.000E05	1.050E06	5.00E06
$\bar{\tau}_{12}$[Pa]	3.4333E07	5.7631E07	7.0408E07	1.000E06	5.250E05	5.00E06
$\bar{\varepsilon}^t_{11}$[-]	9.5230E-03	9.9760E-03	7.2550E-03	9.100E-02	8.585E-04	2.50E-03
$\bar{\varepsilon}^c_{11}$[-]	-6.8020E-03	-8.1620E-03	-6.8020E-03	-1.010E-01	-1.442E-03	-2.50E-03
$\bar{\varepsilon}^t_{22}$[-]	3.6780E-03	5.5329E-03	6.5760E-03	7.000E-03	8.585E-04	-2.50E-03
$\bar{\varepsilon}^c_{22}$[-]	-6.8020E-03	-8.1620E-03	-6.8020E-03	4.000E-03	1.442E-03	-2.50E-03
$\bar{\gamma}^t_{11}$[-]	6.8027E-03	6.1224E-03	6.1224E-03	5.999E-02	1.875E-03	-2.50E-03
minthk [m]	1.0000E-04	1.0000E-04	1.0000E-04	5.000E-03	5.000E-03	1.00E-04
ρ [kg/m^3]	1.9155E03	1.8450E03	1.8450E03	1.100E02	7.000E01	1.00E00

A.11 Coordinate systems in HAWC2

Below figure A.6 presents the coordinate systems used in HAWC2[38].

A.12 Original layup of the DTU10MW reference blade

Below, the material layups along the span are presented for each cross section sub-part for the DTU10MW reference blade.

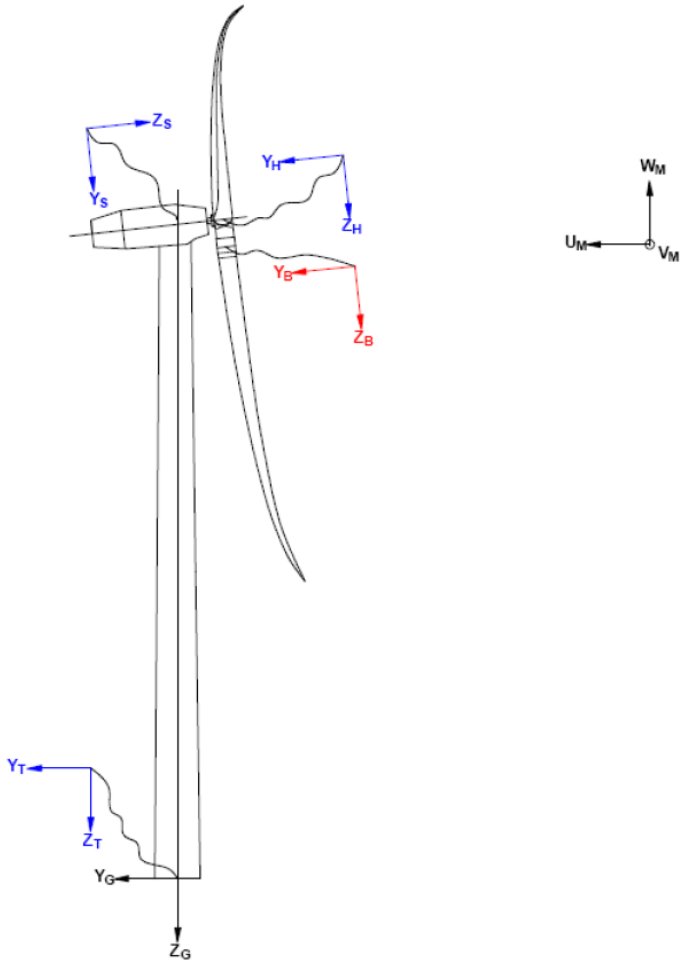

Figure A.6: *Coordinate system definition in HAWC2. Red coordinate system is the blade coordinate system with z along blade span with 0 at root, y towards suction side, and x towards the leading edge.*

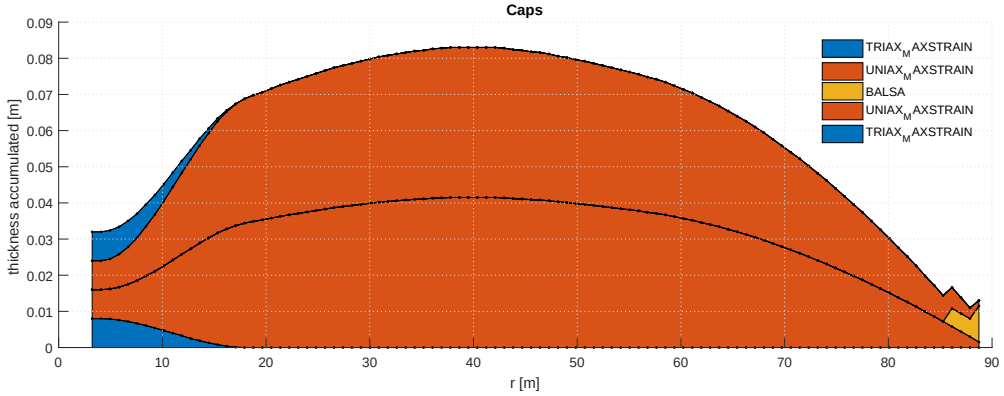

Figure A.7: *Layup of caps*

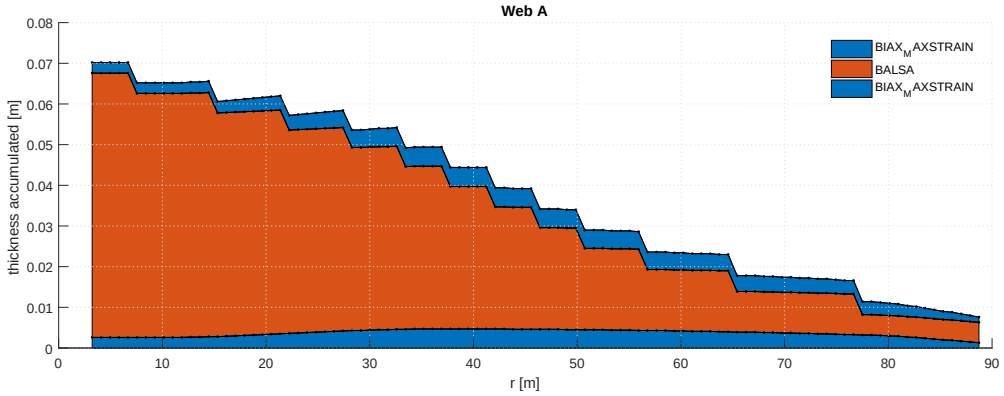

Figure A.8: *Layup of web A*

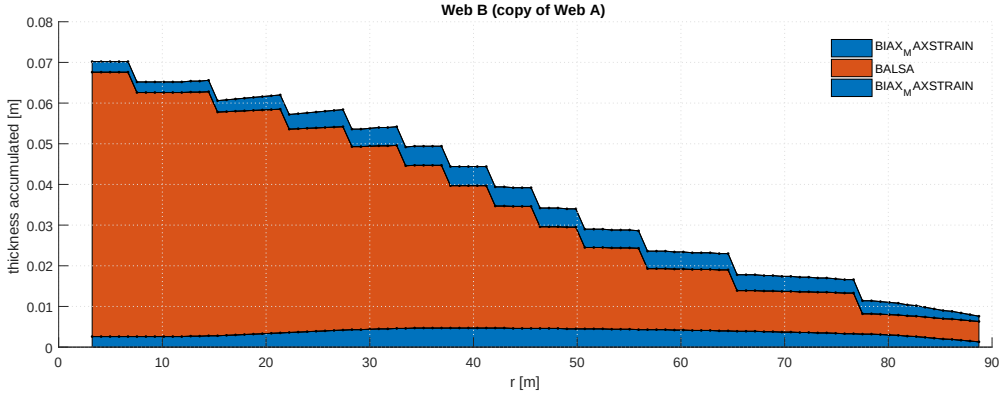

Figure A.9: *Layup of web B*

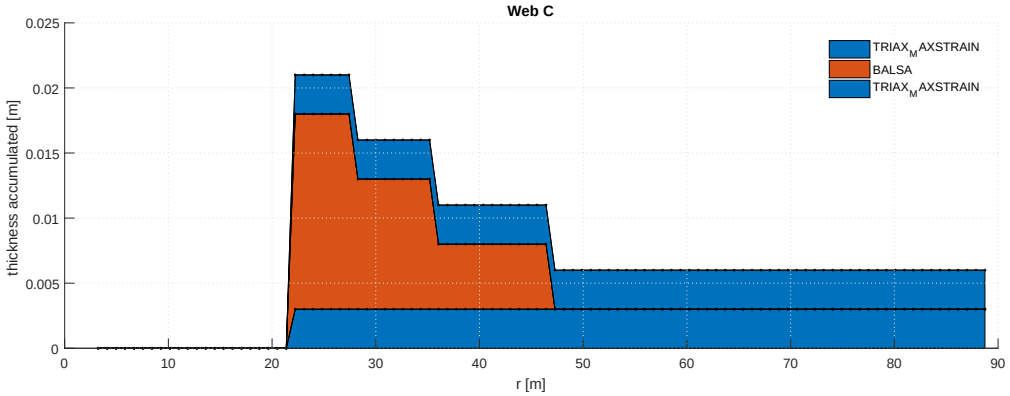

Figure A.10: *Layup of web C*

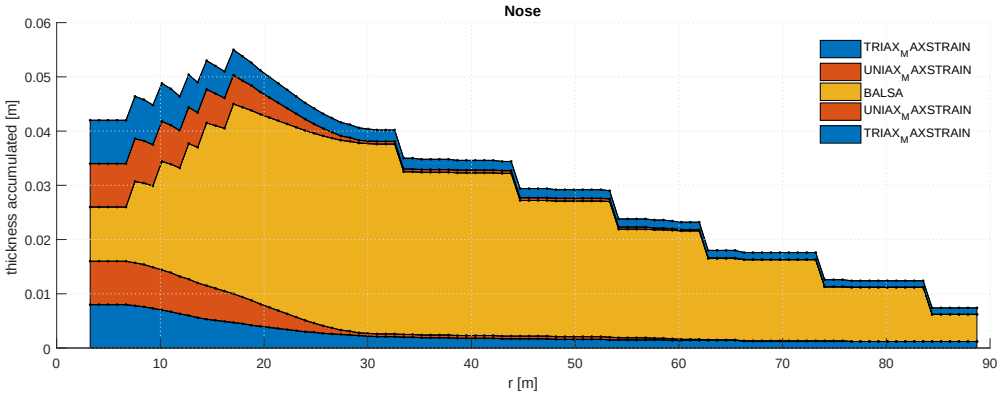

Figure A.11: *Layup of nose (leading edge)*

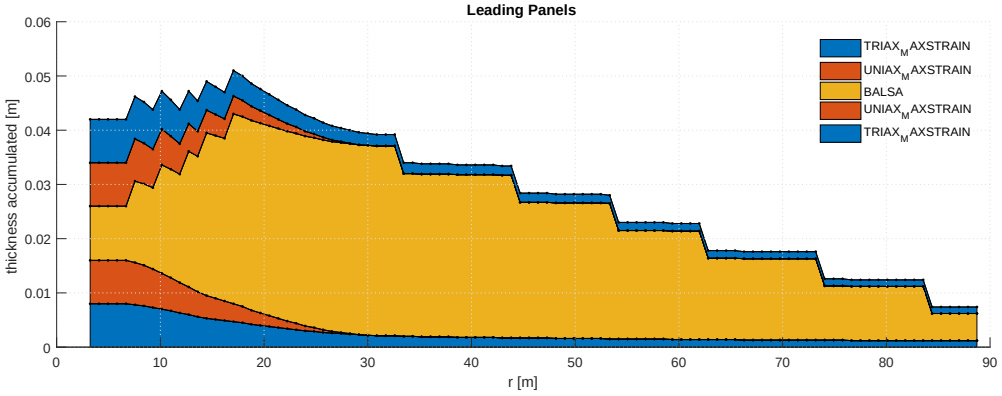

Figure A.12: *Layup of leading panels*

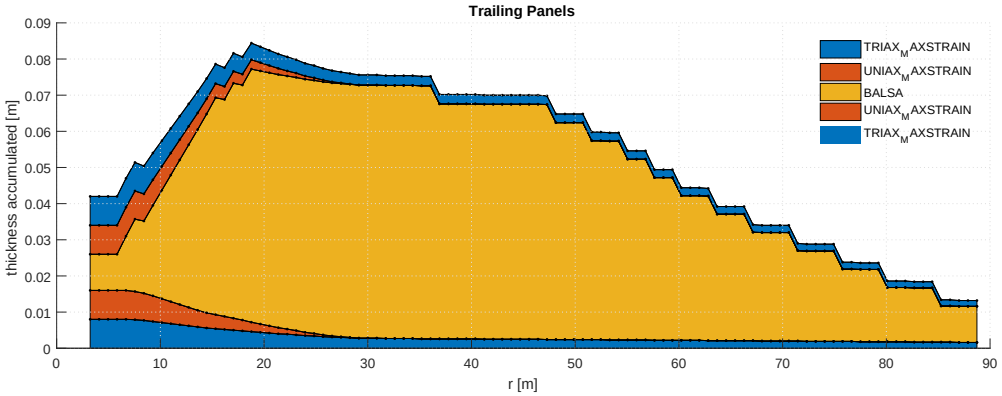

Figure A.13: *Layup of trailing panels*

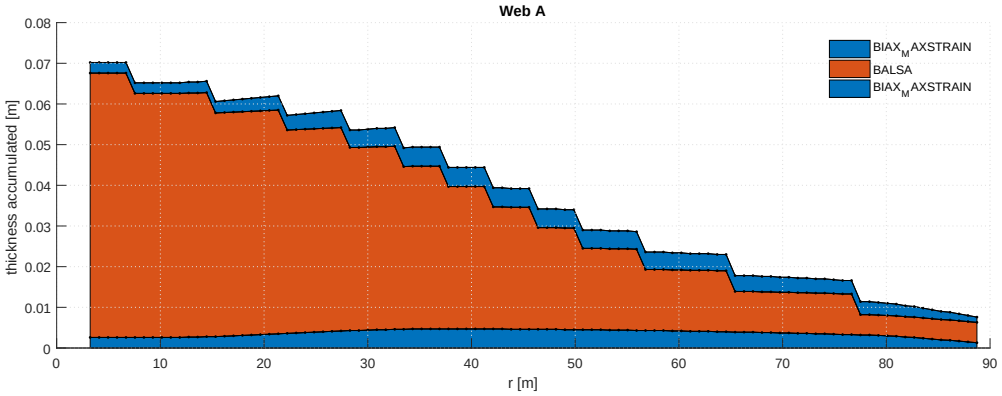

Figure A.14: *Layup of web A*

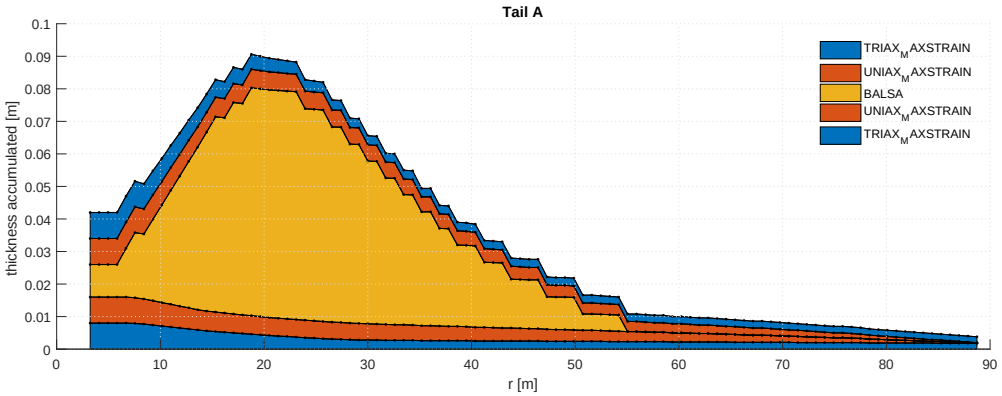

Figure A.15: *Layup of tail A*

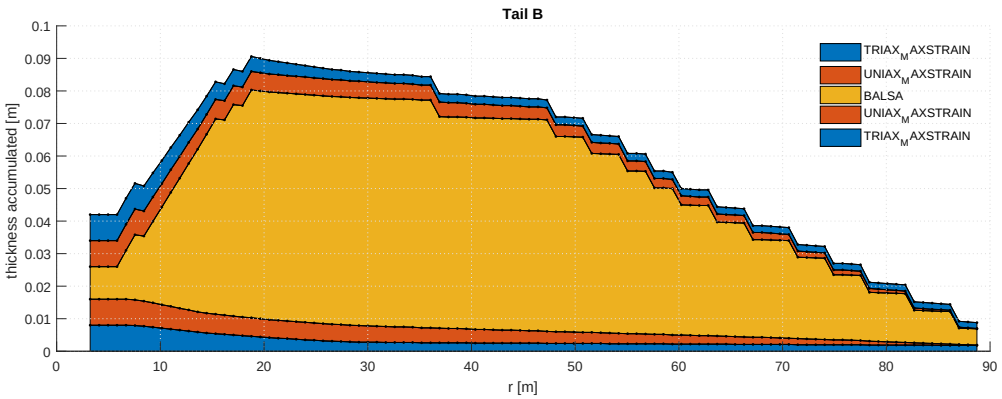

Figure A.16: *Layup of tail B*

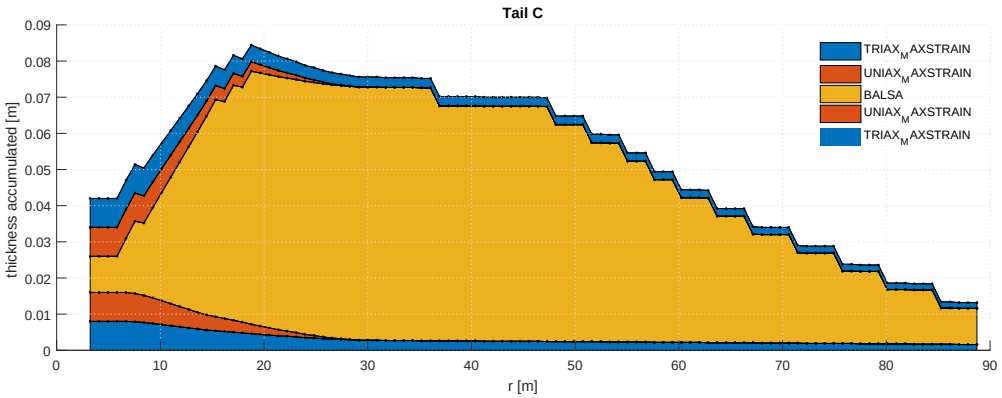

Figure A.17: *Layup of tail C*

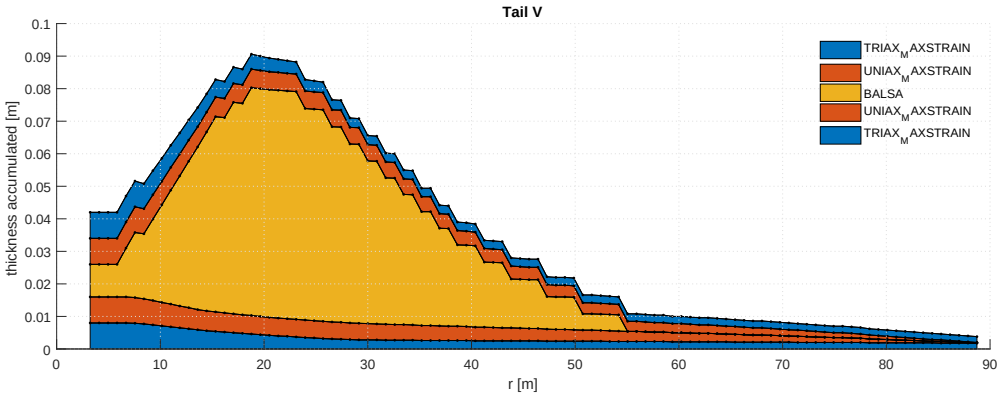

Figure A.18: *Layup of tail V*